Master's thesis

NTNU
Norwegian University of Science and Technology
Faculty of Engineering
Department of Marine Technology

Karoline Bakken

Fatigue of Dynamic Power Cables Applied in Offshore Wind Farms

Master's thesis in Marine Technology
Supervisor: Svein Sævik
June 2019

NTNU
Norwegian University of
Science and Technology

Karoline Bakken

Fatigue of Dynamic Power Cables Applied in Offshore Wind Farms

Master's thesis in Marine Technology
Supervisor: Svein Sævik
June 2019

Norwegian University of Science and Technology
Faculty of Engineering
Department of Marine Technology

NTNU
Norwegian University of
Science and Technology

NTNU Trondheim
Norwegian University of Science and Technology *Faculty of Engineering*
Department of Marine Technology

MASTER THESIS SPRING 2019

for

Stud. Tech. Karoline Bakken

Fatigue of Dynamic Power Cables applied in Offshore Wind Farms

Utmatting av dynamisk kraftkabel til bruk i havvindmølleanlegg

Floating wind farms is expected to become an important solution with respect to developing future renewable energy. This will include dynamic power cables that will be exposed to hydrodynamic loads from wave and floater motion kinematics. A standard dynamic alternating current (AC) cable normally includes three 95 mm2 copper conductors that will be exposed to fatigue. Each of the copper conductors consist of 19 wires which is manufactured in two layers outside the centre wire. During previous PhD works, fatigue data from both single wire and full conductor cross-section testing has been obtained so as to provide input to fatigue analysis. The present thesis deals with investigating which operating life that can be expected in a dynamic power cable exposed to realistic dynamic loads. The work is carried out as a continuation of the project conducted fall 2018 and is to be carried out as follows:

1. A literature review into power cable technology, local and global analysis of dynamic riser cables including local and global failure criteria as reflected in relevant design standards. Also familiarize with the computer programs SIMA (Riflex) and Bflex.
2. Establish a case scenario that includes a realistic wind mill floater and a dynamic cable cross-section. This is to include relevant environmental conditions in terms of current and waves, associated floater motions, cross-section details and cable SN fatigue data.
3. Establish a riser configuration and a global analysis model in SIMA
4. Establish a local analysis model in Bflex.
5. Perform global and local analysis to calculate the fatigue. This is to include sensitivity analysis with respect to drift-off, weather heading, cross-section friction coefficient, bending stiffener design and other parameters to be agreed upon during the course of the work.
6. Conclusions and recommendations for further work

The work scope may prove to be larger than initially anticipated. Subject to approval from the supervisors, topics may be deleted from the list above or reduced in extent.

In the thesis report, the candidate shall present her personal contribution to the resolution of problems within the scope of the thesis work

Theories and conclusions should be based on mathematical derivations and/or logic reasoning identifying the various steps in the deduction.

The candidate should utilise the existing possibilities for obtaining relevant literature.

Thesis report format
The thesis report should be organised in a rational manner to give a clear exposition of results, assessments, and conclusions. The text should be brief and to the point, with a clear language. Telegraphic language should be avoided.

The report shall contain the following elements: A text defining the scope, preface, list of contents, summary, main body of thesis, conclusions with recommendations for further work, list of symbols and acronyms, references and (optional) appendices. All figures, tables and equations shall be numerated.

The supervisors may require that the candidate, in an early stage of the work, presents a written plan for the completion of the work.

The original contribution of the candidate and material taken from other sources shall be clearly defined. Work from other sources shall be properly referenced using an acknowledged referencing system.

The report shall be submitted in electronic format (.pdf):
- Signed by the candidate
- The text defining the scope shall be included (this document)
- Drawings and/or computer models that are not suited to be part of the report in terms of appendices shall be provided on separate (.zip) files.

Ownership
NTNU has according to the present rules the ownership of the thesis reports. Any use of the report has to be approved by NTNU (or external partner when this applies). The department has the right to use the report as if the work was carried out by a NTNU employee, if nothing else has been agreed in advance.

Thesis supervisors:

Prof. Svein Sævik, NTNU

Deadline: June 11th, 2019

Trondheim, January 15, 2019

Svein Sævik

Candidate – date and signature: 18/01/19 Kaspar Ballhaus

Preface

This project is meant as an answer to the subject TMR4930 Marine Technology, Master Thesis, and thus serves as a master thesis in Marine Structural Engineering at the Department of Marine Technology at NTNU. The work was carried out in the spring of 2019.

The topic for the thesis is fatigue of dynamic power cables applied in offshore wind farms. This topic was chosen due to the author's interest in fatigue, a well as the opportunity to use well-known methods and software from the oil and gas industry with new and upcoming renewable technology. The goal of the project is to estimate the lifetime of a dynamic power cable attached to a floating offshore wind turbine at a chosen location, and get an insight in the friction mechanisms in the cross-section and their impact on fatigue life of the power cable.

The report contains a comprehensive literature study and theory about offshore wind, dynamic power cables, and fatigue. It also includes a description of the modeling of two different numeric models, as well as global and local analyses, calculation of fatigue life and study of friction mechanisms. The numeric background for the software used is also included. In the course of the work, choices and simplifications were made in line with the recommendations of the supervisor, Professor Svein Sævik.

This master thesis is a continuation of a project thesis executed in the fall of 2018. All the work has been executed by the author, Karoline Bakken.

Trondheim, June 6th, 2019

Karoline Bakken

Acknowledgment

I would like to thank my supervisor Professor Svein Sævik for extensive guidance, advise, and help in all phases of this master thesis. The work would not have been possible without him.

I would also like to thank Ph.D. Candidate Carlos Eduardo Silva de Souza, who has assisted me considerably in building the global model in SIMA RIFLEX.

I am very grateful to Dr. Techn. Olav Olsen who have been so kind as to provide me with information and transfer functions of the OO-Star, and to Håkon S. Andersen who has also contributed with guidance.

Senior Research Scientist at SINTEF Ocean, Naiquan Ye has provided indispensable technical assistance and guidance in my first encounter with Bflex.

Also, I would like to express my gratefulness my fellow students at office C1.058 for great companionship throughout the last 5 years at NTNU and for giving me motivation and good spirit in times where the workload seemed overwhelming.

Last, but not least I would like to thank Anders and my family for unconditional love and support

K.B.

Abstract

As offshore wind energy installations are moving into deeper waters, and further away from shore, floating wind installations are inevitable. The dynamic power cables that deliver electricity from the installation are essential components for this technology. There has been substantial research on the fatigue life of dynamic slender structures in the oil and gas industry, but very little on dynamic power cables applied in offshore wind. Learning more about fatigue of power cables is a key element to advance in offshore floating wind technology. Generally, a power cable consists of conductors with an assembly of wires helically stranded in layers around a core. The conductors experience contact with each other, as well as between the layers in each conductor, making the cables vulnerable for several fatigue mechanisms.

Fatigue of dynamic power cables applied in wind offshore wind farms was investigated further by performing a global and local analysis. The floating wind turbine OO-Star was chosen as a basis for a case study. OO-Star is a design by Dr. Techn. Olav Olsen, and is participating in the project Lifes50+. West of Barra, Scotland was chosen as the location, and the cable design was developed in close dialogue with Professor Svein Sævik. The global model was built in SIMA RIFLEX, and consisted of the whole dynamic part of the cable. The cable was attached to the sea floor, and a point on the free surface with motions OO-Star due to the transfer functions provided by Dr. Techn. Olav Olsen. No compression and a maximum curvature not to be exceeded laid the basis for the configuration of the cable. The focus of this study was to get an insight into the local contact effects of the cross-section, rather than to perform a full fatigue analysis. Therefore, only three different wind conditions and vessel displacements were included. The local model was created in Bflex. It was assumed that the most severe fatigue damage would occur at the cable hang off, hence only the upper part of the cable was modeled. The local model consisted of a stiff pipe, a bend stiffener, and a cable with several layers and contact elements between them.

The global analyses were performed by running each sea state in the scatter diagram of West of Barra with one hour record length. The angle between the vessel and the cable, and the tension in the upper element were converted into time series and counted by the Rainflow Counting algorithm. The cycle counts and angle range classes were rearranged into 15 cases with dynamic angles and corresponding dynamic tensions. Each dynamic angle and tension pair was applied to the local model for one full cycle. The stress range on wire level was calculated by an analytical model, and fatigue life was calculated by an SN-Curve and the Miner-Palmgren summation concept. Further studies of the friction mechanisms in the cable cross-section were also performed

The fatigue life of the dynamic power cable was estimated to be 267.37 years, but the results were sensitive to the choice of SN-Curve. Further analyses showed that the effect of friction between conductors and between the layers of the conductors played a prominent role in fatigue life.

Sammendrag

De siste årene har utviklingen innenfor offshore vind teknologi vært at installasjonene plasseres lenger unna kysten med dypere vann. De dynamiske kraftkablene som leverer strømmen fra installasjonene er viktige komponenter for denne typen teknologi. Mye forskning har blitt gjort på slanke konstruksjoner i forbindelse med olje og gass industrien, men svært lite er blitt gjort med tanke på utmatting i strømkabler anvendt i flytende offshore vind teknologi. En strømkabel består vanligvis av ledere med tråder som er ordnet i spiraler rundt en kjerne. Dette skaper kontakt både mellom lederne og mellom lagene av tråder i hver enkel leder, og gjør kablene sårbare for ulike utmattingsmekanismer.

Ved å utføre globale og lokale analyser ble utmatting i den dynamiske strømkabelen undersøkt. Den flytende vindturbinen OO-Star ble ansett som en interessant konstruksjon å bruke til dette prosjektet. OO-Star er et design utviklet av Dr. Techn. Olav Olsen som en del av forskningsprosjektet Lifes50+. West of Barra utenfor Skottland ble brukt som lokasjon, og kabeldesignet ble utformet i nøye dialog med Professor Svein Sævik. SIMA RIFLEX ble brukt for å modellere den globale modellen som består av hele kabelen. Den ble festet til havbunnen og til et punkt på overflaten som beveger seg likt som OO-Star gjennom transfer funksjonene fra Dr. Techn. Olav Olsen. Kabelkonfigurasjonen ble basert på kravet om ingen kompresjon i kabelen, samt en maks kurvatur som ikke kunne overskrides. Kun tre vindtilstander med tilhørende flyterposisjoner ble inkludert ettersom målet med oppgaven var å undersøke utmattingsmekanismer, og ikke å utføre en fullstending utmattingsanalyse. Den lokale modellen bestod av den øvre delen av kabelen, da det ble ansett som sannsynlig at utmattingsskadene ville være størst her. Den lokale modellen bestod av kabelen selv med dens mange lag, et stivt rør og en bøyestiver.

Den globale analysen ble utført ved at alle sjøtilstandene beskrevet i scatter tabellen til West of Barra ble analysert i en time hver. Vinkelen mellom turbinkonstruksjonen og den øvre delen av kabelen ble regnet ut for hvert tidssteg, samt spenningen i det øverste elementet av kabelen. Rainflow Counting ble brukt for å telle antall sykluser for hver vinkel. Dette ble reorganisert til 15 lasttilfeller med vinkelintervall og tilhørende strekkintervall. Lasttilfellene var input til den lokale analysen, der hver klasse med vinkel og strekk ble analysert i en syklus. Den resulterende kurvaturen og strekket for hver klasse ble brukt sammen med en analytiske modell til å regne ut spenningsintervallet for hvert lasttilfelle. Deretter ble utmattingslevetiden regnet ut fra en passene SN-kurve og Miner-Palmgen sum. Videre ble kontaktmekanismer i tverrsnittet undersøkt.

Utmattingslevetiden til den dynamiske strømkabelen ble regnet ut til å være 267.37 år, men utregningen er sensitiv for valg av SN-kurve. I tillegg ble det konkludert med at kontakt mellom ledere, og kontakt mellom lagene i hver leder er av høy betydning for utmattingslevetiden, og bør inkluderes i utmattingsanalyser.

Contents

List of Figures

List of Tables

Nomenclature

Latin Letters

a	Acceleration
A	Area, Amplitude
b	Buoyancy
c	Constant
C_P	Power coefficient (Betz Factor)
C_D	Drag coefficient
C_L	Lift coefficient
C_M	Mass coefficient
$\mathbf{C}$	Damping matrix
d	Depth, Damage
D	Drag, Diameter, Total damage
E	Kinetic energy, Young's Modulus
F	Force
F_j	Fill factor
$\bar{F}_x$	Mean axial force
ΔF_x	Dynamic axial force
G	Shear Modulus
$H(\omega)$	Transfer function
Hs	Significant wave height
I	Second moment of inertia
k	Wave number
$\mathbf{K}$	Global stiffness matrix

L Lift, Length
LR Locking radius
m Mass
$\dot{m}$ Mass flow
$\bar{M}_T$ Dynamic bending
ΔM_x Dynamic torque moment about helix tangential x-direction
ΔM_y Dynamic torque moment about helix tangential y-direction
ΔM_z Dynamic torque moment about helix tangential z-direction
$\mathbf{M}$ Mass matrix
n Number of cycles, number of wires
N Number of cycles until failure
P Power
P_0 Power of free-flowing flow
r Radius
$\mathbf{r}$ Nodal displacement vector
R Stress ratio, Radius
$\mathbf{R}$ Global load matrix
S Wave spectrum
t Time
Tp Peak period
$\bar{T}$ Mean tension
ΔT Dynamic tension
v Velocity of airflow
$\dot{V}$ Volume flow
W Weight
z Distance from still water level

Greek Letters

α Lay angle, Damping coefficient
γ Shear strain
$\Delta\beta$ Dynamic curvature
ϵ Phase, Strain
ζ Wave elevation
θ Angle
κ Curvature
μ Friction coefficient
ν Poisson's Number
ρ Density of water, Material density
ρ_{air} Density of air
σ Stress
$\bar{\sigma}$ Mean stress
σ_u Ultimate stress
σ_y Yield stress
$\Delta\sigma_T$ Stress range due to dynamic tension
$\Delta\sigma_{nc}$ Stress range from normal curvature
$\Delta\sigma_{tc}$ Stress range from transvers curvature
$\Delta\sigma_f$ Stress range from friction
σ^2 Variance
τ Friction force per unit length
ψ Polar cordinate angle
ω Circular frequency

Acronyms

AC Alternating Current
DC Direct Current
DFF Design Fatigue Factor
FEM Finite Element Method
$HHT-\alpha$ Hilber-Hughes-Taylor Method
$JONSWAP$ Joint North Sea Wave Project
RAO Response Amplitude Operator
SCF Stress Concentration Factor

Chapter 1

Introduction

1.1 Motivation and Background

Different renewable energy alternatives are being explored as the world strives towards greener energy. Man has utilized wind for thousands of years, and in recent years, wind energy has become one of the more mature renewable energies. As the areas on land that are fit for wind turbines are limited, and the public is dissatisfied with the noise and visibility of the wind turbines, technology is advancing towards offshore wind parks. Moving the wind parks offshore is not only solving the problems with criticisms from the public, but wind speed tends to increase with distance from shore. In the last years, there has been an increase in scale, capacity, and distance from shore each year for offshore wind installations. Moving further from shore often implies moving into deeper waters, making floating wind turbines the most plausible technology.

Floating wind turbines are similar to semi-submersible oil platforms, but have very different motions, as geometry and wind loads are significantly different. Extensive research has been done in terms of evaluating the lifetime for flexible risers and umbilicals in relation to fatigue for the oil and gas industry. For floating wind turbines, there is considerably less research done in terms of the lifetime of dynamic flexible cables. As the power cables that are connected to floating structures are subjected to oscillations due to movements of the vessel in waves, fatigue strength requires to be verified for design.

A cable usually consists of several conductors with layers of copper wires in each conductor. The wires are stranded helically around a core wire, and this causes contact both between the conductors, and between each layer in the conductors. The complex contact situation makes the cable vulnerable for fretting fatigue in addition to fatigue due to the cyclic variation in curvature and tension due to the vessels movements in the waves, Nasution et al. (2014). Karlsen (2010) clarifies that neither the fatigue properties, nor the methods to ascertain SN-data of copper conductors are established by the cable or offshore industry. Knowledge about power cable technology and the lifetime of power cables is one of the most important limiting factors of moving floating wind turbines further away from shore and into deeper waters. To continue the advancement of floating wind turbines in the future, research is necessitated, Thies et al. (2012).

Lifes50+ is a project funded by the Horizon2020 program where the purpose is to develop cost-effective floating solutions for 10MW wind turbines, Horizon 2020 (n.d.). The project consists of 4 different designs and 3 separate locations. One of the designs in the project is the OO-Star

developed by Dr. Techn. Olav Olsen shown in Figure 1.1.1. OO-Star was deemed an appropriate base for a case study to review the lifetime of dynamic power cables further.

Figure 1.1.1: Dr. Techn. Olav Olsen's OO-Star, Lifes50+ (2018)

1.2 Literature Review

A literature search was done prior to the study. Feld et al. (1995) looked at the applied loads and responses of the metallic elements for subsea configurations. Alani & Raoof (1997) studied the effect of mean axial load on axial fatigue life of spiral strands, and concluded that increasing lay angle had a significant negative effect on endurance limit for both the outer and wires in a spiral strand. Chien et al. (2004) discussed different cable designs for 250MW offshore power transmission and concluded that they do not behave like umbilicals dynamically, and that harmonics do occur during transmission. Raoof & Davies (2008) looked at axial fatigue design of sheathed spiral strands in deepwater applications, and concluded that (among other things) the fatigue life of stranded spirals is significantly shorter at the end termination than in free-field. Karlsen (2010) presented a test method for simulating fatigue of a dynamic power cable that included the effects of fretting, creep and friction.

Nasution et al. (2013) investigated fatigue of 95mm^2 copper conductors experimentally and by the use of FEM. Single wires from different layers were tested in tension, and the full cross-section was tested in bending. The full cross-section showed lower fatigue strength that the individual wires and trellis points were particularly vulnerable, as cracks initiated from these points. It was suggested that the difference in results between the testing and the FEM analyses was due to the surface irregularities in the wires from the packaging of the conductor. Nasution et al. (2012) did similar tests and concluded that all first fatigue failures in tension-tension of the full cross-section happened in the outer layers of the conductors, in the thinnest parts of the wires, that is, the trellis points. For tension-bending mode, all the failures occurred in the inner layer of the conductor. It was concluded that this indicated that the effect of friction between layers plays an important role in the lifetime of the cross-section. The report also comments that as the longitudinal stress governs the fatigue performance. Nasution et al. (2014) did experimental and FEM analysis of fatigue strength with 300mm^2 conductors. This study concluded with that in terms of maximum

stress, individual wires from 95mm^2 and 300mm^2 wires fall in a common scatter band, and that lubricated conductors have longer fatigue life than unlubricated conductors. The study also supports the previous conclusions that crack initiation starts from trellis points. In this article, an analytic method to calculate the stress variation in the individual wires of the conductor was developed. Taninoki et al. (2017) looked at dynamic cable systems for 2MW and 100kW floating offshore wind installations and concluded that their proposed cable profile absorbed the floater behavior so that there was no motion in the cable at the bottom hang off.

1.3 State of the Art

1.3.1 Offshore Wind Turbines

According to Gao et al. (2018), "Offshore wind is by far the most developed technology and promising cost reduction has been achieved in the last few years," in terms of offshore renewable technologies. Figure 1.3.1 shows the development of offshore wind capacity until 2017.

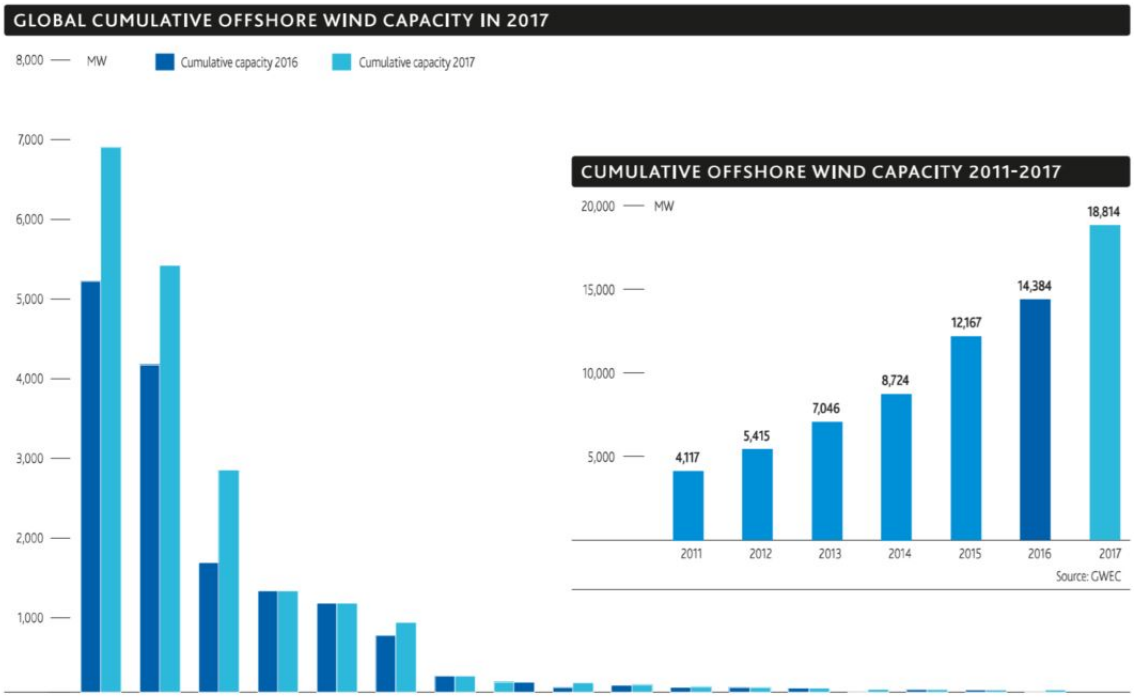

	UK	Germany	PR China	Denmark	Netherlands	Belgium	Sweden	Vietnam	Finland	Japan	South Korea	United States	Ireland	Taiwan	Spain	Norway	France	Total
Total 2016	5,156	4,108	1,627	1,271	1,118	712	202	99	32	60	35	30	25	0	5	2	0	14,483
New 2017	1,680	1,247	1,164	0	0	165	0	0	60	5	3	0	0	8	0	0	2	4,334
Total 2017	6,836	5,355	2,788	1,271	1,118	877	202	99	92	65	38	30	25	8	5	2	2	18,814

Figure 1.3.1: Cumulative offshore wind capacity in 2017, Global Wind Energy Counsil (GWEC) (2018)

The majority of the offshore wind farms are located in Europe. Figure 1.3.2 presents the current market situation of offshore floating wind turbines. As can be seen, it is mainly Europe, the USA, and China that are represented.

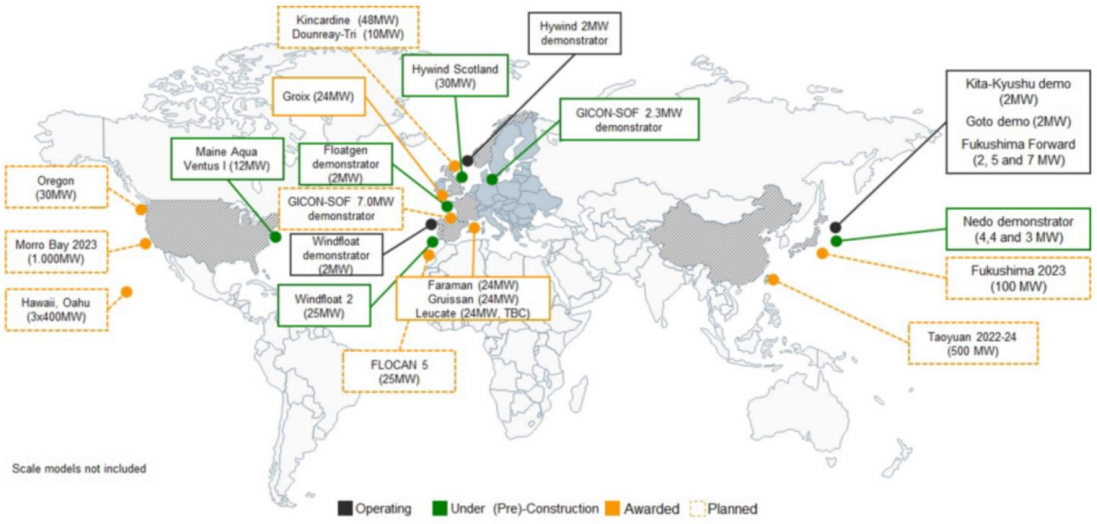

Figure 1.3.2: Current market situation of offshore floating wind turbines, Gao et al. (2018)

In recent years, installations have moved further from shore, into deeper waters and with large farm configurations and larger turbines. Longer blades give advantages in terms of overall cost, but also challenges for installation, Gao et al. (2018). Figure 1.3.3 shows the development of power capacity for the last two centuries. The average size in 2017 was 5.9 MW. That is an increase of 23% from 2016, according to Wind Europe (2018).

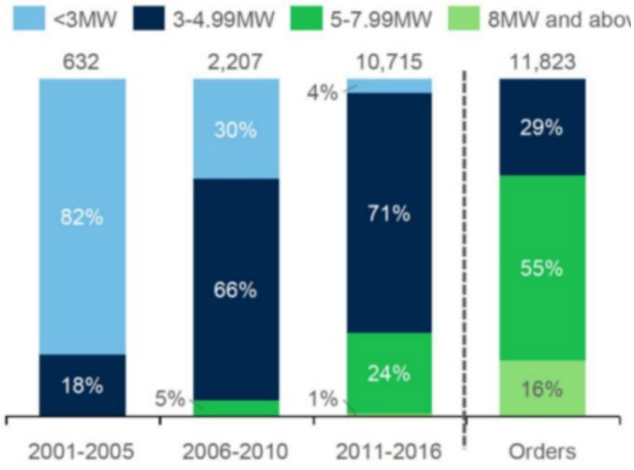

Figure 1.3.3: Development of turbine size, Deigen (2017)

In 2016, the first 8 MW turbine was installed in the Irish Sea in the UK. In Norway, Statoil made a step towards commercialization of floating wind farms by installing the first floating wind farm with 5 6MW spar wind turbines called Hywind, outside of Scotland. Hywind can be employed at depths up to 800m, and enable offshore wind energy installations for areas that have been unavailable until now, Equinor (2018). Short-term plans for the offshore wind industry cover the

installation of two small floating wind farms in the US as well as prototype testing for existing prototypes in Norway, Portugal, and Japan, and planned prototype development in Japan, France, and Germany. Two large wind farms are projected on the east coast of the US, one 120 MW farm outside of Maryland, and one 90 MW on the coast of New York, Gao et al. (2018).

Bailey et al. (2014) states that "Commercialization of floating wind farms is anticipated between 2020 and 2025." In 2014 the European Union set a legally binding target that 27% of the energy consumption is to come from renewable energy sources in 2030. European Wind Energy Association (EWEA) (2015) presents three separate scenarios on the development of offshore wind energy by 2030. The central scenario proposes that 66 GW should come from offshore wind. To achieve this goal, an annual average increase of 15% is required. Gao et al. (2018) states that the goal is probably reasonable as we have seen an increase of 25%-30% annually in recent years. US Department of Energy has a goal of 86 GW of energy provided from offshore wind by 2050, Walt Musial & Draxl (2016).

1.3.2 Power Cables

The trend over the years has been that offshore wind installations move further away from shore. This development is demonstrated in Figure 1.3.4.

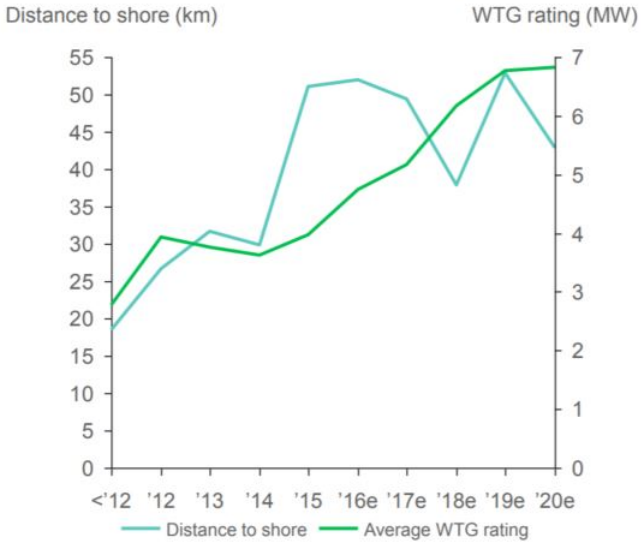

Figure 1.3.4: How distance to shore have increased in recent years, Make Consulting (2016)

Srinil (2016) states that traditionally, the w shape configuration has been used for inter-array cabling, and the lazy wave has been used for export cables, see Figure 1.3.5. However, according to Sommerville (2010), the lazy wave configuration is being considered for inter-array in newer projects such as the Statoil's Hywind project, and the Fukushima Floating Offshore Wind Farm Demonstration Project, Yagihashi et al. (2015). Inter-array cables are usually three-core copper conductors, armored with steel wires with insulation around the conductors, Srinil (2016).

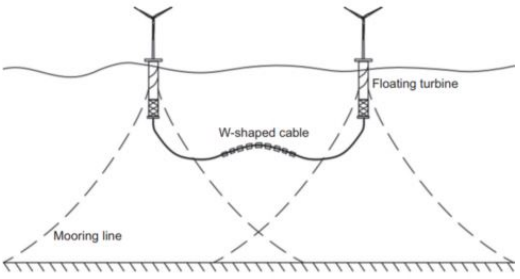

(a) Traditional W-shape for inter array cable

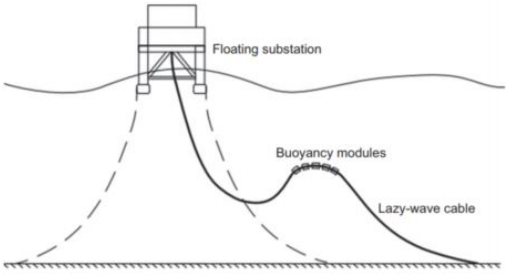

(b) Lazy wave shape, traditionally only used for export cables

Figure 1.3.5: Different cable configurations, Sommerville (2010)

1.4 Objective

The objective of this master thesis is to estimate the lifetime of a dynamic power cable applied in offshore wind farms. Theory and software used and developed for the oil and gas industry, are implemented in the relatively new and upcoming field of ocean renewable energy.

The focus of this study is to estimate the fatigue life of a dynamic power cable at a chosen location through global and local analyses, and with the use of well-known fatigue calculation methods such as Rainflow Counting, SN-Curve, and Miner-Palmgren summation. Besides, the study focuses on getting an insight into the mechanisms affecting the fatigue life of the cable down to fiber level in the power conductors. Investigation of fatigue in steel armouring is not included in the study.

This master thesis is a continuation of a project thesis that was completed in the fall of 2018.

The main objectives of this study are based on the Master Description attached earlier in this report. And all choices or adjustments to the initial plan were made in close dialogue with the supervisor for the project, Professor Svein Sævik. The main objectives are:

1. Perform a literature study and acquire the necessary theoretical background on all topics relevant for the master thesis, including but not limited to global and local analyses, offshore wind turbines, cable technology, and fatigue.
2. Choose and establish a case scenario regarding wind turbine floater design, location, environmental conditions, cable design, and SN-fatigue data
3. Create a global model in SIMA RIFLEX and determine cable configuration.
4. Create a local model in Bflex
5. Perform global and local analyses and process the results to estimate the fatigue life of the dynamic power cable.
6. Conduct a sensitivity study to investigate the friction mechanism in the conductor.

1.5 Contribution

The main contribution from this study is the investigation of fatigue life of a dynamic power cable down to fiber level. By including calculation of friction effects on two levels, insight was gained on what affects the fatigue life of stranded helical copper conductors, whose fatigue properties are not well established. The fatigue life of dynamic power cables was examined by performing global and local analyses on a designated case scenario. The most important conclusion in this study is that contact between conductors, and between layers in each conductor contributes significantly to the fatigue damage, and should be included in analyses in the future. Also, the fatigue life calculation is sensitive to choice of SN-Curve.

1.6 Master Thesis Structure

- **Chapter 1** contains the introduction with a literature review, state of the art and objective for the master thesis.
- **Chapter 2** demonstrates the system theory for wind turbines, offshore wind turbines, and power cables.
- **Chapter 3** goes through how waves can end up causing fatigue damage for an offshore structure.
- **Chapter 4** introduces the case scenario.
- **Chapter 5** describes the theory behind the two numeric models.
- **Chapter 6** explains the modeling methodology.
- **Chapter 7** goes through the analyses methodology.
- **Chapter 8** presents the results and discussion of the results.
- **Chapter 9** is the conclusion and suggestions for further work.

Chapter 2

System Theory

To understand the problem and the procedure to examine the fatigue of dynamic power cables in wind farms, a fundamental understanding of the system is required. This chapter covers theory for wind turbines in general and offshore wind turbines as well as subsea power cables. The chapter also includes historical background, some principal mathematical background, and other relevant theory.

2.1 Wind Turbines

A wind turbine can convert kinetic energy into mechanical energy, and then to electric energy. This conversion is done by extracting the kinetic energy of an air stream by the use of a rotating, disk-shaped wind energy converter, Hau (2013).

2.1.1 Historical Background of Wind Turbines

According to Wagner (2013), man has utilized energy from the wind for thousands of years. In the earliest years, wind energy was mainly used as propulsion for sailing vessels. There are accounts of windmills in Persia as early as 914 AD, and in Europe from around 1200 BC. The first windmills were used for pumping of water and grinding of cereal. Between 1700-1800 there was a major spurge in windmill technology, and new designs with higher efficiency emerged. Lynn (2011) states that before the industrial revolution, windmills were an important source of mechanical energy in Europe. Denmark, England, Germany, and the Netherlands were among the countries with the most development. Windmill technology experienced even more growth in the twentieth century, and in early 1900 multi-blade wind farms were developed in the US. At this time, the wind energy was used to convert kinetic energy into mechanical energy, Hau (2013). According to Lynn (2011), as the industrial revolution emerged, the advancement of windmills declined. Steam engines and combustion motors could provide power at any time, efficiently and independent of weather conditions. Electrical motors could be used to grind grains and pump water more effectively than ever. By the mid-1900s it was rare to see a traditional windmill still in service.

As the electricity technology evolved, the notion of utilizing windmills to generate electrical power arose. One of the most remarkable people behind this approach was Charles Brush. As early as 1888 he developed "A multi-blade rotor 17 m in diameter, [...]a 12 kW dynamo charged a battery bank that fed various motors and hundreds of incandescent lights in his home over the next 15 years", Lynn (2011). This was the first *wind turbine*. In the following years, there was enormous

progress in the design and performance of wind turbines. Hau (2013) describes the emergence of the modern wind turbine with the unit created by Ulrich Hütter. He published papers on the theory of wind energy in 1942 and is said to be one of the pioneers of modern wind energy technology. Hütter built wind turbines with fewer blades, that were profoundly aerodynamically refined, and designed for a greater rotation speed than was seen previously. According to Wagner (2013), this was particularly beneficial, as only a small generator was required to generate electricity. Figure 2.1.1 shows a wind turbine by Hütter, and as can be seen, it is quite similar to the wind turbines one usually encounters today.

Lynn (2011) describes the 200kW wind turbine designed and built by the Dane Johannes Juul in 1957 as one of the most prominent concepts leading up to the modern wind turbine. It had stall control, and emergency aerodynamic tip breaks to avert damage in extreme weather. In 1975 it was refurbished by NASA to be used in their wind energy program. This turbine put Denmark on the map as one of the principal wind energy nations.

Figure 2.1.1: "Wind turbine by U. Hütter in Stötten in the Swabian Alb, Germany (rotor diameter 34 m, rated power 100 kW), 1958-1968", Hau (2013)

In spite of the dramatic increase in efficiency attained by the new technology, energy from wind turbines did not prove to be competitive compared to other sources of electricity in the 1960s to 1970s. It was not until the oil crisis in the seventies that several countries recognized that the world would eventually be dependent on other energy sources than fossil fuels sometime in the future, Wagner (2013). President Jimmy Carter ensured the financing for several extensive wind projects, and by the early 1980s, the state of California had thousands of wind turbines with a combined power production of 1 GW. Nevertheless, this development stalled as President Reagan withdrew the financing of many projects, making Europe, and especially Denmark and Germany the leading nations in wind turbine technology, Lynn (2011).

2.1.2 Mathematical Background of Wind Turbines

The concept of a wind turbine, independently of type, is to convert kinetic energy in the wind into mechanical energy, using a disk shape rotating wind energy converter. The mechanical energy is used to generate electrical energy. According to Hau (2013), Albert Betz was the first to implement this principle to windmills, and developed theory where he applied elementary physics to wind converts. The theory contains simplifications such as assumed frictionless flow; however, it has demonstrated to be quite useful in the early stages of calculation for practical engineering. The following part of the section was originally developed by Albert Betz and later reproduced by Hau (2013).

Basics of Albert Betz Momentum Theory:

Kinetic energy:

$$E = \frac{1}{2}mv^2 \qquad (Nm) \tag{2.1}$$

where for a wind converter, v is the velocity of an air flow of mass m. The volume flow, $\dot{V}$ is:

$$\dot{V} = vA \qquad (m^3/s) \tag{2.2}$$

where A is the area. The mass flow $\dot{m}$ is expressed as:

$$\dot{m} = \rho_{air} vA \qquad (kg/s) \tag{2.3}$$

where ρ_{air} is the density of air. The amount of energy passing through the cross-section per unit time:

$$P = \frac{1}{2}\rho_{air} v^3 A \qquad (W) \tag{2.4}$$

The kinetic energy in the airflow decreases with the extraction of mechanical energy. Reducing the velocity means widening the area of the cross-section. This is depicted in Figure 2.1.2. Here, V_1 and A_1 refer to the flow velocity and area before the extraction of energy, and V_2 and A_2 refer to the flow velocity and area after the extraction.

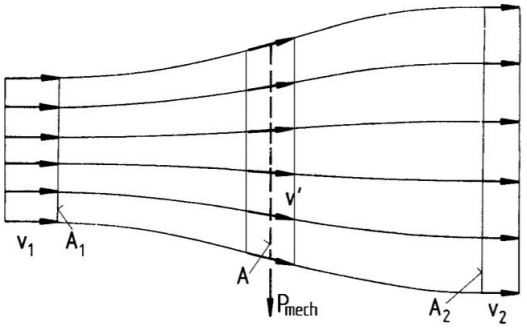

Figure 2.1.2: Changing flow conditions due to extracting of mechanical energy based on elementary momentum theory, Hau (2013)

The extraction of energy is due to the *difference* in power before and after the extraction:

$$P = \frac{1}{2}\rho_{air} v_1^3 A_1 - \frac{1}{2}\rho_{air} v_2^3 A_2 = \frac{1}{2}\rho_{air}(v_1^3 A_1 - v_2^3 A_2) \qquad (W) \tag{2.5}$$

From the Equation 2.5 it follows that the maximum energy extracted is obtained if $V_2 = 0$. Physically, however, this does not make sense as this implies that V_1 must become equal to zero, meaning no energy extraction at all. Through the conservation of momentum, Albert Betz developed a theory of the optimal relationship between the flow velocity before and after the extraction, $\frac{V_1}{V_2}$. c_p was introduced to have a reference for the power output, where the power output, P is compared the power of a free-flowing flow without extraction, P_0.

$$C_P = \frac{P}{P_0} \tag{2.6}$$

Figure 2.1.3 shows that the maximum power to be extracted is at C_P close to 0.6, more precisely at:

$$C_P = \frac{16}{27} = 0.593 \tag{2.7}$$

This is frequently called the Betz factor and expresses the maximum theoretical efficiency.

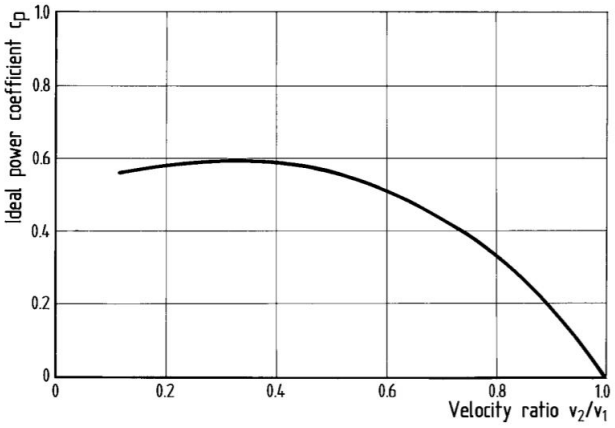

Figure 2.1.3: "Power coefficient versus velocity ratio" Hau (2013)

Basics of Foil Theory

One of the most fundamental components of the wind turbine are the blades. They are shaped as foils and are responsible for the transfer of the kinetic energy in the wind, to the mechanical energy of the rotor. Mathew & Philip (2012) states that in earlier days, the foils in wind turbines were adopted from airplane foils. Today, there is a whole industry dedicated to the optimization and design of wind turbine foils. A basic illustration of the essential features of a standard airfoil is shown in Figure 2.1.4.

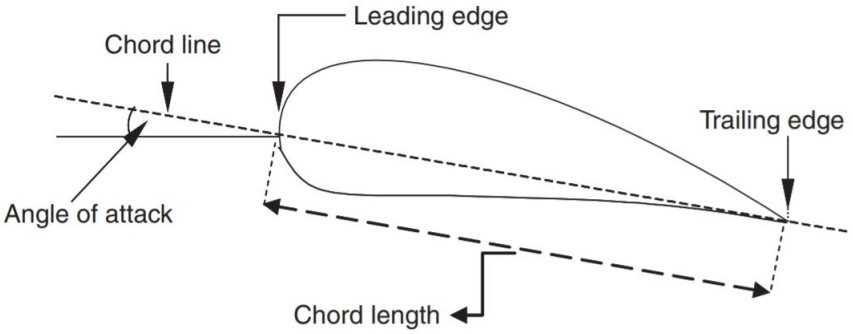

Figure 2.1.4: Basic features of a foil, Mathew & Philip (2012)

If the foil is placed in a flow stream, the foil experiences a separation of streamlines above and below the foil. Due to the configuration of the foil shape, the streamlines above the foil have a longer way to travel than those below the foil. Because of this, the velocity of the flow on the upper side has to increase to meet the particles in the streamlines on the bottom of the foil at the

trailing edge. According to Bernoulli's theorem, increased velocity has to be counterbalanced with a reduction in pressure. Decreased pressure creates a pressure difference between the upper and lower side of the foil resulting in a lift force directed upwards. At the same time, a drag force is also exerted on the foil. Their resultant is the net experienced force on the airfoil, as illustrated in Figure 2.1.5.

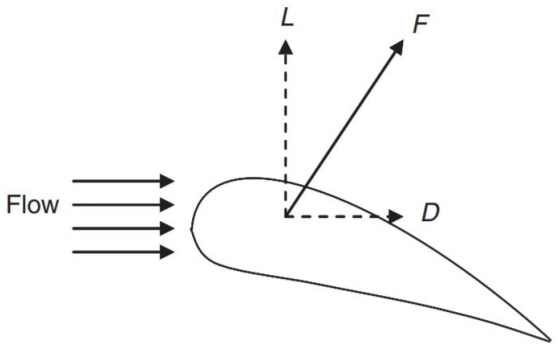

Figure 2.1.5: Lift and drag on an airfoil, Mathew & Philip (2012)

The lift and drag can be expressed as:

$$L = C_L \frac{1}{2} \rho_{air} v^2 A \qquad (N) \tag{2.8}$$

$$D = C_D \frac{1}{2} \rho_{air} v^2 A \qquad (N) \tag{2.9}$$

Where C_L and C_D are lift and drag coefficients respectively.

The angle of attack influences the lift and drag forces (see Figure 2.1.4). In terms of airfoils used in wind turbines, the drag force is just a parasite component following the lift force, so it is a goal to maximize lift and minimize the drag so that the ratio $\frac{C_L}{C_D}$ reaches its maximum. For a wind turbine, the rotation of the foils creates a tangential velocity. The velocity experienced by a point is thus the resultant of the velocity and the tangential velocity. The drag force is parallel with the resulting velocity, and the lift is always perpendicular to the drag.

2.2 Offshore Wind Turbines

The theory in the following paragraph is taken from Kapsali & Kaldellis (2012).

In later years, there has been a significant increase in wind power installations. Renewable energy is on high demand, and wind energy is considered a cost-effective way of providing it. As restrictions on wind installations increase in terms of noise and visibility, development is being withheld. This has made a new market emerge: Offshore Wind Energy. Offshore wind energy implies electrical energy generated by a wind installation placed offshore. There are several advantages of this: wind speeds tend to increase with distance from shore, giving offshore wind energy an even greater potential than on-land wind energy. Also, the noise and visibility of the wind

turbines are no longer a problem as if the installation is placed far enough from shore. Also, the environmental impact is minimal. However, there are several challenges as well. The wind industry is a relatively new industry, and the ocean conditions such as weather, waves, currents, corrosion, and more, pose several challenges and demands multidisciplinary cooperation for development of plausible designs. New approaches are needed in terms of turbine, structure, installation, and maintenance, and the cost of offshore wind energy is considered higher than on land. Offshore wind energy generally follows a simple rule: The further from shore an installation is placed, the greater energy potential in terms of wind speed, but this also implies deeper waters and increased development and operation costs. A lot of the experience gained from the oil and gas industry is valuable in the advancement of offshore wind energy.

2.2.1 Historical Background for Offshore Wind Turbines

Ng & Ran (2016) states that the first offshore wind farm was developed in Denmark in the 1990s. According to Lynn (2011), this wind farm consisted of 11 turbines providing 5 MW combined. By using the already existing knowledge and technology both from the onshore windmill industry and the offshore oil and gas industry, offshore wind turbines have experienced rapid growth in the middle of the 2000s, with doubling of capacity every 2-4 years, Ng & Ran (2016). Figure 2.2.1 shows the increase in offshore wind installations. Lynn (2011) States that "It is reasonable that Europe will generate tens of gigawatts of offshore electricity by 2020".

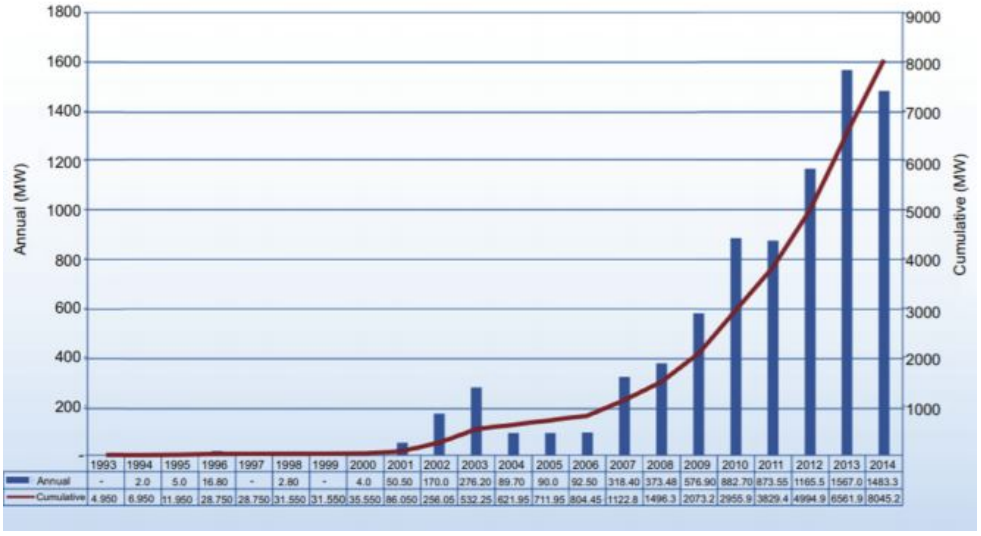

Figure 2.2.1: Annual and cumulative offshore wind installations from 1993-2014, Ng & Ran (2016)

2.2.2 Modifications for Offshore Wind Installations

Offshore wind turbines are quite similar to onshore wind turbines, but with some modifications. Generally, offshore wind installations are larger to make use of the increased energy potential due to the high wind speeds. Concern for the public is also not a problem offshore, allowing larger installations that are more visible and noisier. Other alterations are necessary due to the harsh environment offshore. According to Kapsali & Kaldellis (2012), this includes:

- Strengthening of the tower to be able to handle the loads from the high wind speeds and wave loads form the ocean
- Corrosion systems to avoid corrosion from the salty water
- Warning lights and bright markers to avoid collision.

2.2.3 Offshore Support Structures

Offshore wind turbines may be attached to the seabed or floating. According to International Renewable Energy Association IRENA (2016), the support structures that are attached to the seabed are restricted to water depths of 50m or less. As the offshore wind industry aims to move installations further offshore with increasing water depths, floating solutions are necessary. By introducing floating support structures, water depths constraints are eliminated (at least in terms of support structure). This opens new markets for countries with few shallow water areas suitable for offshore wind energy production. In most cases, moving further away from shore increases the wind speeds, and it also decreases the environmental impact on the surroundings. The main floating options presented in Figure 2.2.2, are all familiar concepts from the oil and gas industry that have proven successful in demanding environments.

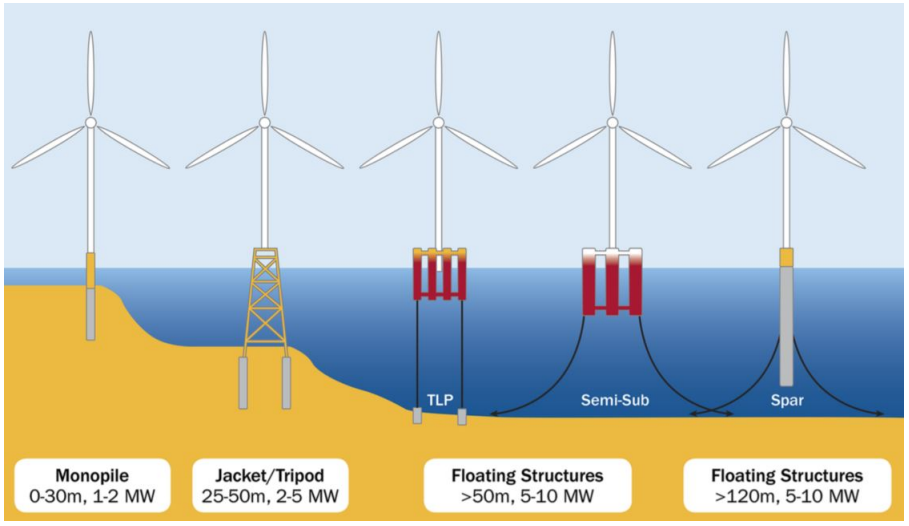

Figure 2.2.2: Different support structures, Bailey et al. (2014)

There are several pros and cons to the different designs, taken from International Renewable Energy Association IRENA (2016):

Tension Leg Platform (TLP): Very buoyant structure connected to tensioned tendons secured to the seabed by piled or suction anchors.

Pros :

- Low mass
- Lower critical wave induced motions
- May be assembled onshore

Cons :

- Stability issues during installation and transportation
- May need special purpose vessel for installation
- Higher mooring cost
- Some uncertainty around high frequency dynamic effects

Semi submersible: Submerged pontoons. Kept in position by mooring lines

Pros :

- May be assembled onshore
- Low drought, may be transported fully equipped using tugs.
- Lower mooring costs

Cons :

- Higher critical wave induced motions
- Large structures, use more material
- Complex fabrication
- Higher mooring cost

Spar Buoy: A cylinder with high drought with ballast below the center of gravity. kept in position with mooring lines

Pros :

- Lower critical wave induced motions
- Simple design.
- Lower mooring costs

Cons :

- Installation requires heavy lift vessel
- Needs high water depths.

2.3 Subsea Power Cables

The cabling system is a crucial component for the offshore wind energy installation. Electrical power cables are used in offshore wind technology to provide energy from the wind turbine to shore or the other way around. It can also be used to provide power to other installations at sea, Nasution et al. (2013). Srinil (2016) describes that the cable industry has experienced a significant increase in the demand for subsea power cables. As technology pushes installations further from shore, and into deeper waters with tough conditions, technical advances are needed for the power cables as well. For safe and efficient transfer of electricity, cable designs must be optimized according to the location of the system, infrastructure, and technical properties. " [...]to significantly increase offshore wind capacity, the inter-array and export cabling systems have been identified by the offshore wind industry as one of the key areas where related cost savings should be considered." Srinil (2016). The design of offshore power cables has several technical and economic challenges, where the distance from shore is an important parameter. According to Lynn (2011), it is most economical to use 3-phase high-voltage AC transmission for distance up to 50 km.

Thies et al. (2012) states that there is substantial experience with marine power cables due to the large oil and gas industry. However, there is little knowledge about the loading regimes for floating marine energy converters because the technology is still relatively new and is lacking ex-

perience.

There are several different cables in use to transport the generated electricity from the wind turbine to shore, or an offshore installation, illustrated in Figure 2.3.1 This project focuses on the dynamic part of an inter-array cable between the floating structure and the seabed.

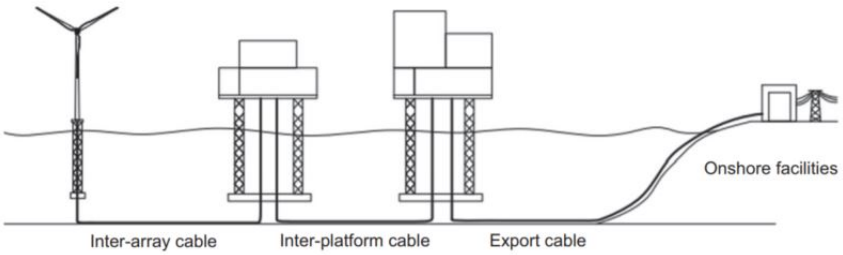

Figure 2.3.1: Different subsea power cables for different use. Adapted from Srinil (2016)

As can be seen in Figure 2.3.1, an inter-array cable link up several wind turbines to an offshore substation where the electricity is collected and transformed before it is sent to shore. Srinil (2016) describes that the inter-array cable is usually quite short, usually less than 1500m, depending on the size of the installation, and the spacing requirements between turbines. Inter-array cables are usually three-core copper conductors, armored with steel wires with insulation around the conductors. 33kV is usually the standard for offshore cables; however, 66kV is under development.

2.3.1 Dynamic Power Cables

According to Thies et al. (2012), power cables can be used in static applications, where it is connected to a fixed structure, or dynamic application where it has to withstand significant cyclic loading. Srinil (2016) stats that "For offshore floating wind turbines, attention must be paid to the development, design, and optimization of a robust dynamic power cable." The combination of the different loads from waves, wind, currents, and more are complex and need to be assessed through a coupled model and experimental tests.

2.3.2 General Design of Subsea Power Cable

There are several different designs of subsea power cables. According to Beckman et al. (2013), each cabling system is specially designed for its purpose, making repairs and maintenance challenging. Thies et al. (2012) describes some of the most common features for a standard subsea power cable presented in Figure 2.3.2:

A Conductor core: Carry the electrical current, and consists of wires made of copper or aluminum.

B Electrical insulation: Insulating the conductors. Possible materials are oil-impregnated paper, cross-linked polyethylene, or ethylene propylene rubber.

C Sheath: Acts as a water barrier, and to protect the cable against fault currents.

D Armature: Metallic armature usually two layers of galvanized steel wires. Gives mechanical strength and protects against impact

E Protective sheath: Outer layer of cable gives abrasion strength, and is made out of polypropylene

Optical cables may be included in the cross-section for some applications. Cables need to be optimized for their use, and standardized cables are rather rare.

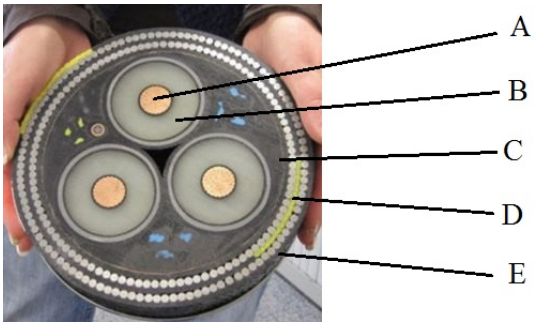

Figure 2.3.2: Main components of a typical subsea power cable. Adapted from Bolotinha (n.d.)

As mentioned in Section 1.3.2, the W-configuration is not the only configuration that has been used for inter-array cables in recent years, and other configurations are being explored. Figure 2.3.3 shows some of the most common riser configurations for floating offshore structures.

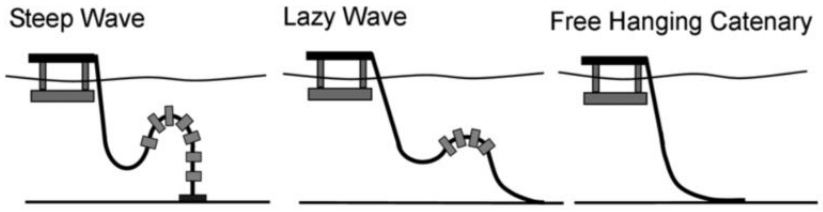

Figure 2.3.3: Different configurations of flexible risers, Thies et al. (2012)

For the 1st and 2nd configuration in Figure 2.3.3, buoyancy modules need to be designed to obtain the desired shape, according to Srinil (2016). These are usually made of synthetic foam. They are positioned on the central part of the flexible riser/power cable and held in place with internal clamps. Using the steep wave or the lazy wave configuration usually minimizes the dynamic response of the cable, decoupling the floating structure motion from the cable touch down point on the seabed. The configuration is highly dependent on the buoyancy elements, so these should not be changed over the lifetime of the flexible cable. Figure 2.3.4 shows how buoyancy elements change the configuration of the flexible riser in terms of hang-off, arch bend, and touch down. "Depending on the hang-off angle, water depth, platform offset, footprint and soil stiffness, areas of local maximum static tensions typically occur at the hang-off point and the two ends [...] of the distributed buoyancy portion[...]", Srinil (2016). The local maximum bending moments happen where the largest curvature occurs.

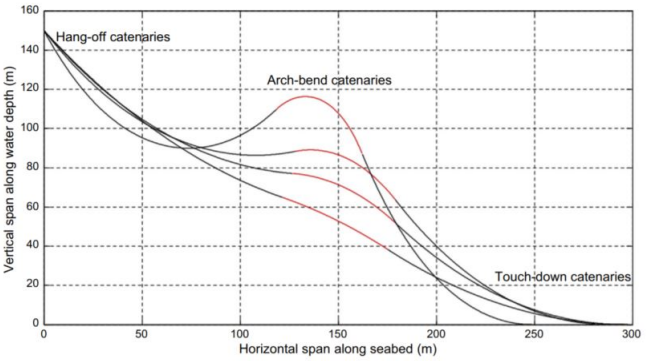

Figure 2.3.4: "Effect of buoyancy distribution (red line) change on the configuration of dynamic cable", Srinil (2016)

2.3.3 Bend Stiffener

The information in the following paragraph is taken from Worzyk (2009).

A dynamic power cable is susceptible to fatigue or over bend when there is an abrupt change in bending stiffness. This can be the case several places including at the cable hang off. An overbend of the cable may lead to severe fatigue damage. To reduce the effect of changing bending stiffness, a bend stiffener may be incorporated in the cable structure. A bend stiffener is a conical structure attached around the cable at the cable hang off. Its conical shape makes the increase of bending stiffness more gradual, and each bend stiffener requires individual design. A poorly designed bend stiffener simply relocates the problem to the end of the bend stiffener.

2.3.4 Copper Power Conductors

According to Worzyk (2009), the majority of subsea power cables include conductors made of copper. Copper is often superior to aluminum for subsea applications, as it allows for smaller cross-section, and thus requires less material for the steel armoring around it. There are several types of conductors as can be seen in Figure 2.3.5. Stranded round cables are most prevalent for subsea application. Nasution et al. (2013) explains that the wires are arranged in layers, and the conductors may be of different sizes with a different number of layers. According to Worzyk (2009) the wires are compressed in stranding machines in layers, or at the end of the stranding. The compression reduces the space between the circular wires, and a compressed copper cable may have a fill factor up to 0.92.

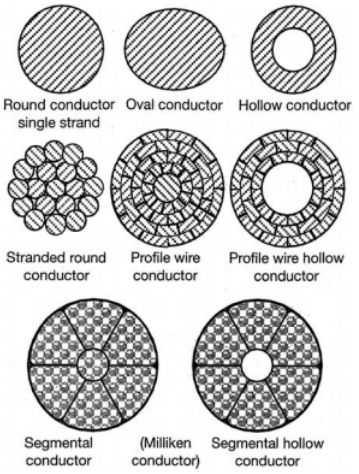

Figure 2.3.5: Different types of conductors, Worzyk (2009)

Nasution et al. (2013) elaborates: The helical nature of the wires in each layer leads to different contact between the wires. Contact between wires of the same layer is called inline contact,

while contact between wires of different layers is called trellis contact. The inline and trellis contact between the wires can be seen in Figure 2.3.6, where the red arrows indicate inline contact, and the black arrows indicate trellis contact.

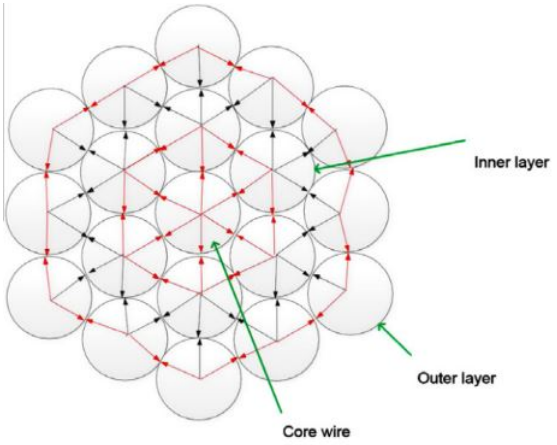

Figure 2.3.6: Inline and trellis contact between wires, Nasution et al. (2013)

The loads on the cables are transferred to the individual wires in the copper conductor. The dynamic and mean tension, are transferred as tension and shear force, and the dynamic bending moment gives local bending and axial friction forces. This can be seen in Figure 2.3.7, where:

- $\overline{T}$ is the mean tension
- ΔT is the dynamic tension
- $\overline{M}_T$ is the mean bending moment
- ΔM_T is the dynamic bending moment
- $\Delta\beta$ is the dynamic curvature
- $\overline{F}_X$ is the mean axial force
- ΔF_X is the dynamic axial force
- ΔM_X is the dynamic torque moment about helix tangential x-direction
- ΔM_y is the dynamic bending moment about helix bi-normal y-direction
- ΔM_z is the dynamic bending moment about surface normal z-direction

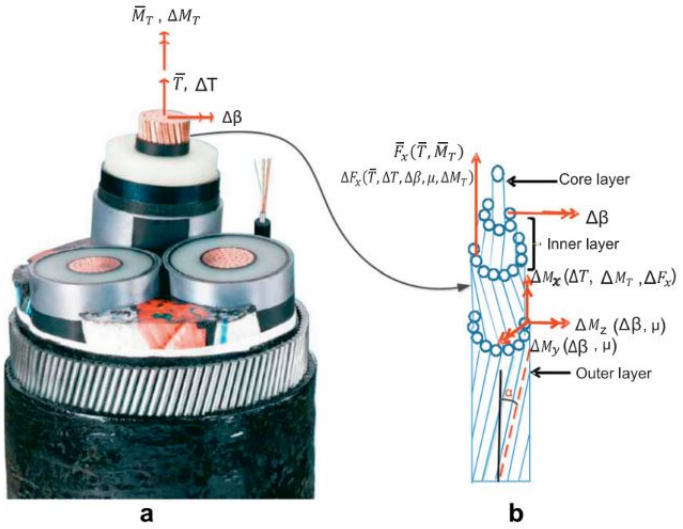

Figure 2.3.7: Forces on a cable, Nasution et al. (2013)

2.3.5 Alternating Current (AC) Voltage

Electrical power can be supplied either by direct current, (DC) or alternating current, (AC). DC only flows in one direction, while for AC, the direction of the current changes several times over a time unit as a sine function, Patrick (2000). Figure 2.3.8 compares the waveform for DC current and AC current.

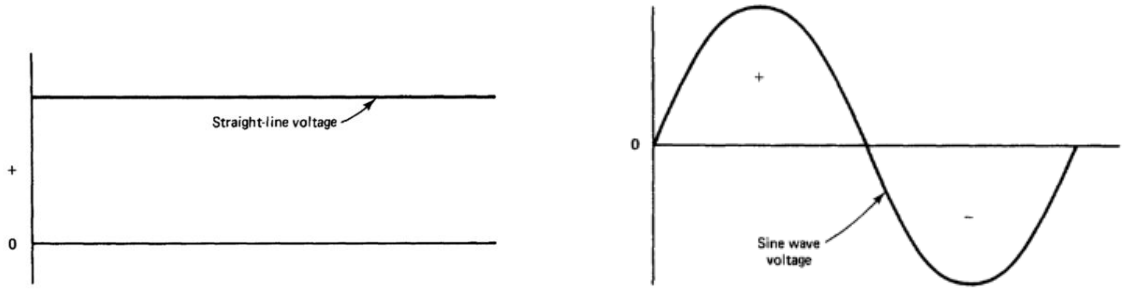

(a) Waveform for DC voltage

(b) Waveform for AC voltage

Figure 2.3.8: Comparison of DC voltage and AC voltage, Patrick (2000)

A three-phase system is made up of three coils rotating in a magnetic field with a phase difference of 120°, Patrick (2000). The three-phase system and its alternating voltage can be seen in Figure 2.3.9. According to Beckman et al. (2013), an AC cable requires one conductor for each phase. The three conductors may be placed in the same cable or within three individual cables. AC demands a thicker cable cross-section than DC, but smaller transformers.

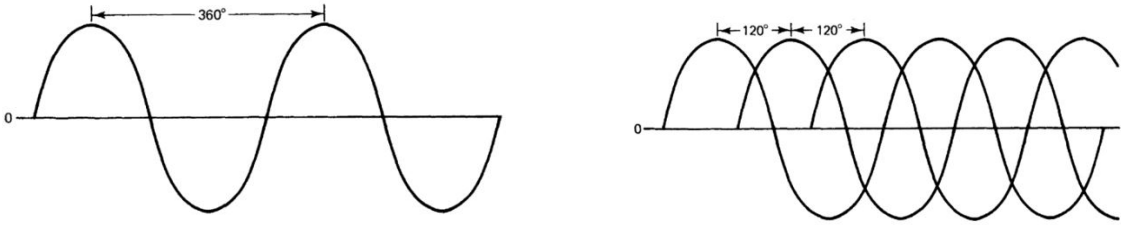

(a) Single phase AC voltage (b) Three phase Ac voltage

Figure 2.3.9: Comparison of single phase and three phase AC voltage, Patrick (2000)

There are several advantages with three-phase AC systems over 1 phase AC systems in terms of price, material use, robustness,"[...] and accounts for the vast majority of the world's industrial machines", Powell (1995).

Chapter 3

Fatigue due to Environmental Loads

In the case of a floating wind turbine, environmental loads that work on the model include waves, wind, current and more. In this thesis, the focus was on wave loads and current. Due to the cyclic nature of waves, failure of dynamic power cables applied in offshore wind farms can either be caused by overloading or fatigue. This study focuses on failure due to fatigue. This section demonstrates the basic principles on how waves can yield fatigue damage for a dynamic power cable attached to a floating wind turbine, as can be seen in the simple flowchart in Figure 3.0.1.

Figure 3.0.1: Flowchart of how waves can give fatigue damage in floating structures

3.1 Statistical Description of Waves

The theory in this section is taken from Faltinsen (1990).

For linear theory, the results from irregular waves can be obtained by adding together results from regular waves. For long-crested irregular sea, the wave elevation can be described as:

$$\zeta = \sum_{j-1}^{N} A_j \sin(\omega_j t - k_j x + \epsilon_j) \tag{3.1}$$

Where ω is the circular frequency, t is time, k is the wave number, ϵ is phase and A is the the amplitude. A can also be expressed in terms of the wave spectrum:

$$\frac{1}{2} A_j = S(\omega_j)\Delta\omega \tag{3.2}$$

Where $\Delta\omega$ is the difference between successive frequencies. The wave elevation is Gaussian distributed with mean at zero and variance at $\sigma^2 = \int_0^\infty S(\omega) d\omega$.

The wave spectrum assumes that the sea can be described as a stationary random process, implying that it is a short-time description of the sea state. The sea state is defined by the significant wave height, Hs, and the peak period, Tp. Hs is the mean height of the $\frac{1}{3}$ highest waves in the sea state, and Tp is the peak frequency of the wave spectrum. There are several different specters but according to Lifes50+ (2015): "[...]the JONSWAP (Joint North Sea Wave Project) is suitable for "wind seas," and thus used in this study. Figure 3.1.1 shows a general wave spectrum and the JONSWAP spectrum. The JONSWAP spectrum can be described as:

$$S(\omega) = 155\frac{H_s^2}{T_1^4\omega^5}\exp\left(\frac{-994}{T_1^4\omega^4}\right)3.3^Y \tag{3.3}$$

Where

$$Y = \exp\left(-\left(\frac{0.191\omega T_1 - 1}{2^{\frac{1}{2}}\sigma}\right)^2\right) \tag{3.4}$$

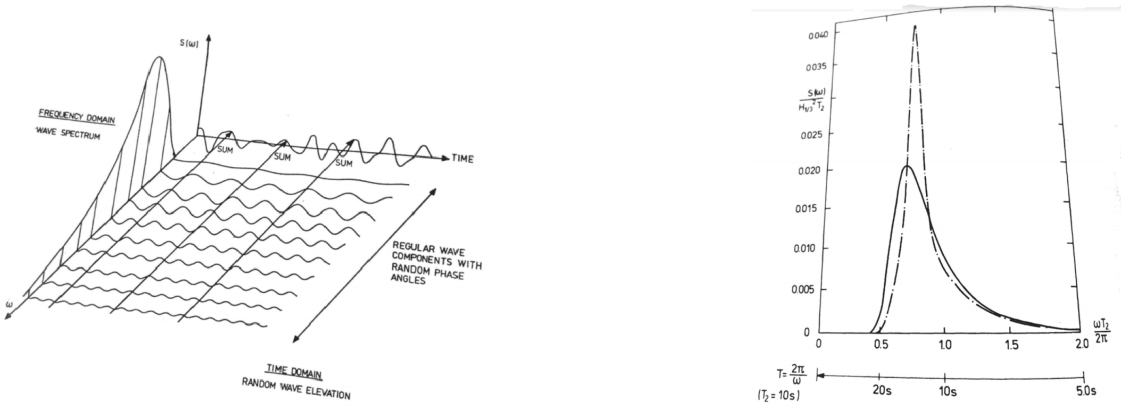

(a) General Wave Spectrum

(b) JONSWAP Wave Spectrum

Figure 3.1.1: General wave spectrum and JONSWAP Spectrum, Faltinsen (1990)

The long-term sea state is usually described in a scatter diagram featuring the number of occurrences for different Hs and Tp.

3.2 Load from Waves

The loads from the waves acting on the floating wind turbine can be calculated using Morison's Equation. The general Morison's Equation expresses the horizontal force, dF, on a strip of the length dz of a fixed vertical cylinder and is formulated in Pettersen (2007) as:

$$dF = \rho\frac{\pi D^2}{4}C_M a_x dz + \frac{1}{2}\rho C_D D u|u|dz \tag{3.5}$$

Where ρ is the density of the water, D is the diameter of the pipe, C_M is the mass coefficient, a_x is the horizontal particle acceleration, is the acceleration in x direction, C_D is the drag coefficient

and u is the horizontal particle velocity.

In the case of a moving cylinder, the Morison's Equation can be modified according to Faltinsen (1990) as follows:

$$dF = \frac{1}{2}\rho C_D D dz(u - \dot{\eta_1})|u - \dot{\eta_1}| + \rho C_M \frac{\pi D^2}{4} dz a_1 - \rho(C_M - 1)\frac{\pi D^2}{4} dz \ddot{\eta_1} \tag{3.6}$$

Where u and a_1 depend on position and dot represents time derivative.

3.3 Response

Langen & Sigbjörnsson (1979) explains that an arbitrary loading can be written as a sum of harmonic components, and these can be Fourier-Transformed so that the contribution from each of the components will be a function of ω. The response can also be transformed into the frequency domain, and this will give a direct measure of how the structure responds to different load frequencies as in Figure 3.3.1. "Solution in the frequency domain is particularity suited for analysis of the response to stochastic loads [...]" Langen & Sigbjörnsson (1979).

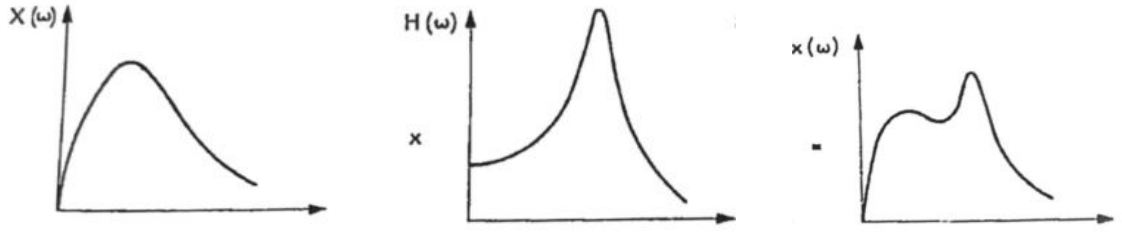

(a) Transformed excitation (b) Transfer function (c) Transformed response

Figure 3.3.1: Solution in the frequency domain, Langen & Sigbjörnsson (1979)

Motion transfer functions provide an efficient description of the motion characteristics of a floating vessel. They are calculated for all 6 degrees of freedom on a specified point on the vessel from either potential theory or experimental tests, SINTEF Ocean (2017). Due to linearity, the response can be analyzed for each wave component in Equation 3.1 separately, Faltinsen (1990). Recalling Equation 3.1, for wave elevation, the steady state response can be written as:

$$A_j|H(\omega)|\sin(\omega_j t - \delta_j(\omega) + \epsilon_j) \tag{3.7}$$

Where $|H(\omega)|$ is called the transfer function. For irregular sea, the response can be linearly superposed for all the different wave components:

$$\sum_{j=1}^{N} A_j|H(\omega)|\sin(\omega_j t - \delta_j(\omega) + \epsilon_j) \tag{3.8}$$

$|H(\omega)|$ and $\delta(\omega_j)$ are functions of frequency, ω.

3.4 Fatigue

Fatigue is damage due to cyclic loading over time where the stress is usually lower than the yield stress for a given material. In this section, some fundamental concepts related to fatigue are presented, as well as the methods used in this master thesis. The following is taken from the compendium by Berge (2016).

3.4.1 Basic Concepts

In Figure 3.4.1, some basic concepts are defined.

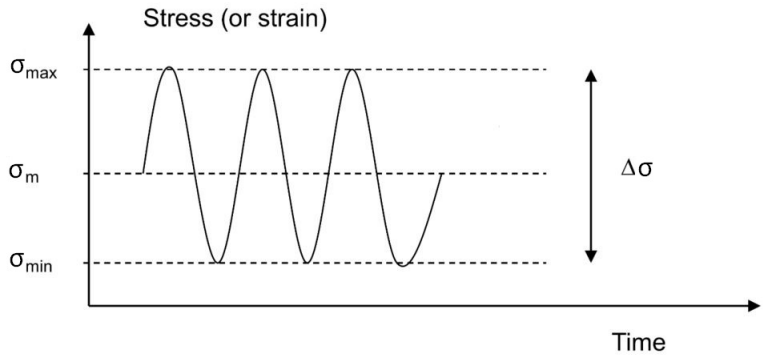

Figure 3.4.1: Example of a fatigue load history, reproduced from Berge (2016)

From Figure 3.4.1, it can be seen that:

- σ_{max} - Maximum stress/strain in a cycle
- σ_{min} - Minimum stress/strain in a cycle
- σ_m - Mean stress/strain in a cycle

moreover, it follows that the stress range, $\Delta\sigma$ is:

$$\Delta\sigma = \sigma_{max} - \sigma_{min} \tag{3.9}$$

And the stress ratio, R is:

$$R = \frac{\sigma_{min}}{\sigma_{max}} \tag{3.10}$$

It is common to differentiate between high cycle fatigue and low cycle fatigue. High cycle fatigue has a fatigue life of more than 10^5 cycles, and the stress is elastic. It tends to follow relationship called the SN-Curve and can be found by Equation 3.11. In the SN-Curve, stress or strain range is plotted against the number of cycles until failure, as can be seen in Figure 3.4.2. For most applications, fatigue life spans over a high number of cycles, so the SN-Curve is presented as a log-log-diagram.

$$N(\Delta\sigma)^m = \mathrm{c} \tag{3.11}$$

Where N is the number of cycles before failure, $\Delta\sigma$ is the stress range, m is an exponent and c is a constant.

DNV GL (2016) elaborates that by subtracting two standards deviations, the SN-Curve represents 97.6% of survival.

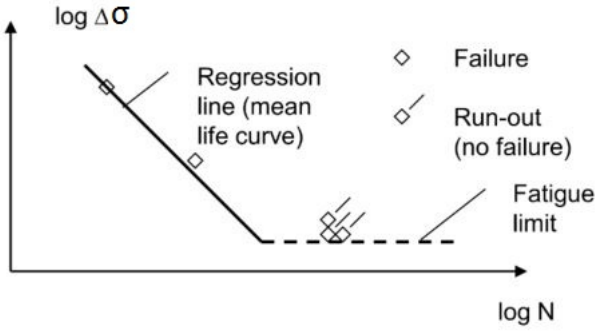

Figure 3.4.2: Example of an SN-Curve, Berge (2016)

For the low cycle fatigue, the material undergoes plastic deformation. For marine structure applications, the stress is usually in the high cycle fatigue range. If the stress range is sufficiently low, fatigue life can approach "infinite". A stress range of this nature is called the fatigue limit and only applies in non-corrosive environments.

The damage done by one cycle is usually close to insignificant, and undetectable by instruments. Failure due to fatigue is a result of the cumulative damage induced by the cyclic loading. For marine structures, load from waves, current, motions, and vortex-induced vibrations may cause severe damage. Fatigue damage can be divided into three stages:

- Crack initiation, N_i
- Crack growth, N_g
- Failure

This means that the fatigue life can be calculated as:

$$N = N_i + N_g \tag{3.12}$$

3.4.2 Irregular Loading

For marine structures, irregularly cyclic loading is common, as in Figure 3.4.3, where the amplitude and frequency vary over time. The lifespan for a typical specimen in the offshore industry is 20 years with an average frequency of 16 1/s. To make the design process manageable, this has to be reduced to a more practical format.

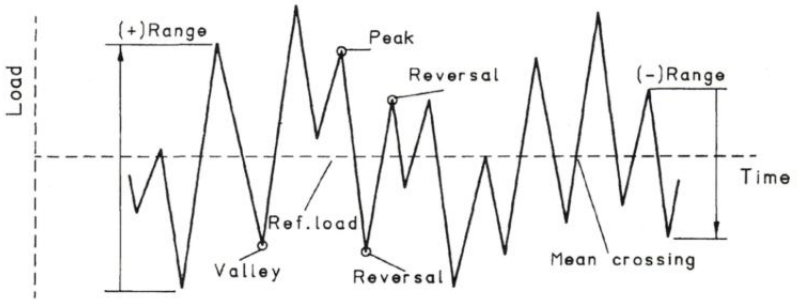

Figure 3.4.3: Example of irregular loading, Berge (2016)

In Figure 3.4.3, a few concepts of irregular loading are defined:

- Reversal - Where the first derivative changes sign
- Peak - Where the first derivative changes from a positive to a negative sign
- Valley - Where the first derivative changes from negative to a positive sign
- Range - Difference between a peak and a valley
- Mean crossing - Number of time the load-time history crosses the mean load level (normally only crossings with positive first derivatives are counted)
- Bandwidth - Ratio of mean crossings with positive slopes to the number of peaks or valleys.

3.4.3 Rainflow Counting

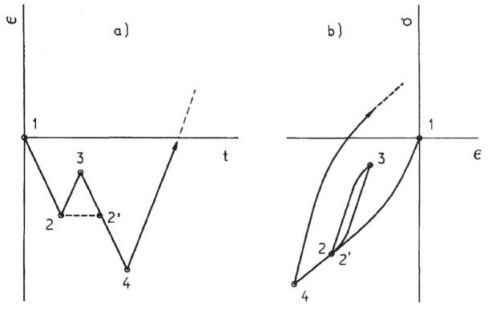

Figure 3.4.4: (a) Cyclic load, (b) Stress-strain response, Berge (2016)

There are several ways of counting cycles, and Rainflow Counting is one of them. The name of this method stems from the thought of rain falling on the roof of a pagoda (Chinese architecture). In this procedure, the reversals are counted in accordance with the stress-strain response. The procedure can be seen in Figure 3.4.4, where the cycle from 2-3-2' does not affect the rest of the stress-strain cycle. Each time a loop is completed, a cycle count is made, so that the counting of the cycles reflects the response of the material. The fatigue damage caused by a closed loop in the irregular amplitude loading is, according to this counting method, the same as one cycle in a constant amplitude test. Half cycles cannot be paired up with other half cycles, so the damage they do on the structure is not counted in this method. However, in a realistic case, there are few half cycles. Due to its versatility, the Rainflow method is considered superior to other counting methods.

The Rainflow Counting algorithm is illustrated in 3.4.5, and goes as follows: Begin at the first valley. If the next valley is deeper or equal to the first one, the rainflow stops here and a cycle is counted, (see point 5 in Figure 3.4.5). If the valley is not deeper than the first one, the flow proceeds to the next valley, (see point 3 in Figure 3.4.5). The rain-flow is also considered to stop if it meets another flow from above, (see point 2' in Figure 3.4.5) When one rainflow has stopped, proceed to the next valley and repeat the procedure. After completion of counting of valleys, the same procedure is performed on the peaks. The results from the Rainflow Counting can be gathered in a histogram that easily shows the number of cycles for different classes.

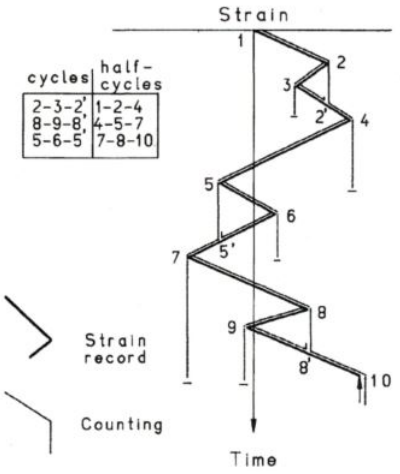

Figure 3.4.5: Rainflow Counting with illustration of the Chinese pagoda origin, Berge (2016)

In this master thesis, Rainflow Counting was utilized by using a module in Pyhton called rainflow.py. According to Janiszewski (n.d.), the module implements ASTM E1049-85 rainflow cycle counting algorithm, and is meant for fatigue analyses. The function rainflow.count_cycles takes in a 1D array of numbers and returns a sorted list of the load ranges and the corresponding number of cycles.

3.4.4 Cumulative Damage

Several methods can be applied to calculate the cumulative damage due to irregular amplitude cyclic loading. The Miner-Palmgren approach has proven to be as good as other methods and is extremely simple. The Miner-Palmgren theory assumes that the damage is constant during a given stress range. The Miner-Palmgren expression:

$$D = \sum_i \frac{n_i}{N} \tag{3.13}$$

where D is the accumulated damage, n_i is the number of cycles with a certain stress range experienced by the structure and N is number of cycles until failure at that stress range.

According to Det Norske Veritas (DNV) (2010), the fatigue criterion which shall be satisfied is expressed as:

$$D \cdot \text{DFF} \leq 1.0 \tag{3.14}$$

Where D is the accumulated damage and DFF is the Design Fatigue Factor.

Table 3.1 show the different Design Fatigue Factors recommended by Det Norske Veritas (DNV) (2010).

Safety Class		
Low	Medium	High
3.0	6.0	10.0

Table 3.1: Design Safety Factors (DFF) for different safety classes recommended by Det Norske Veritas (DNV) (2010)

3.4.5 Mean Stress Correction

According to Sævik & Ye (2016), fatigue tests of steel or copper wires are often done with constant mean stress or with constant R-ratio and always positive to avoid compression. Testing in tension-tension mode normally has a R-ratio of 0.1-0.5, and SN-diagrams deviating from the given R-ratio are often not obtainable. The applied stress range can be calculated for a given R-ratio as:

$$\Delta\sigma = 2\bar{\sigma}\frac{1-R}{1+R} \tag{3.15}$$

To remedy the limitation that SN-Curves are only available for a certain R-ratio, Goodman, Gerber or Söderberg assumptions can be employed to transform between different mean stresses as in 3.4.6. They are described by the following expressions:

Goodman assumption:

$$\Delta\sigma_0 = \frac{\Delta\sigma}{1-(\frac{\bar{\sigma}}{\sigma_u})} \tag{3.16}$$

Gerber assumption:

$$\Delta\sigma_0 = \frac{\Delta\sigma}{1-(\frac{\bar{\sigma}}{\sigma_u})^2} \tag{3.17}$$

Söderberg assumption, Almar-Næss (1985):

$$\Delta\sigma_0 = \frac{\Delta\sigma}{1-(\frac{\bar{\sigma}}{\sigma_y})} \tag{3.18}$$

where $\Delta\sigma_0$ is the stress range at zero mean stress, $\Delta\sigma$ is the calculated stress range, $\bar{\sigma}$ is the mean stress level, σ_u is the ultimate stress level of the material, and σ_y is the yield stress level of the material.

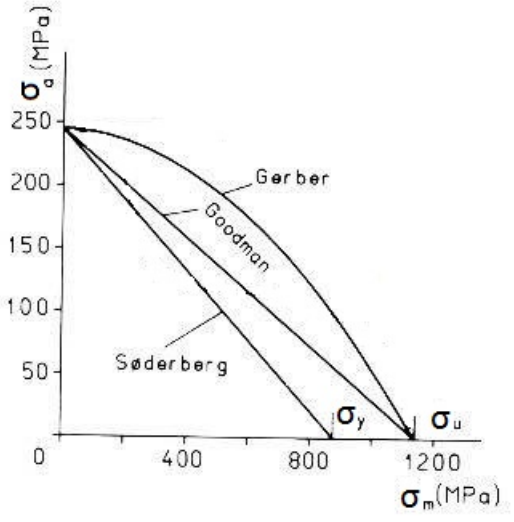

Figure 3.4.6: Goodman, Gerber and Söderberg relations, adapted from Almar-Næss (1985)

3.4.6 Fatigue of Dynamic Power Cables

Nasution et al. (2013) states that when the cable is in operation, it experiences loads from gravity, the motions of the floating vessel, and from the sea. The cable experiences a mean global tension and torque due to gravity. Surge and heave motions induce dynamic tensile and torque, while pitch and roll motions give a dynamic curvature of the cable. This can be seen in Figure 3.4.7.

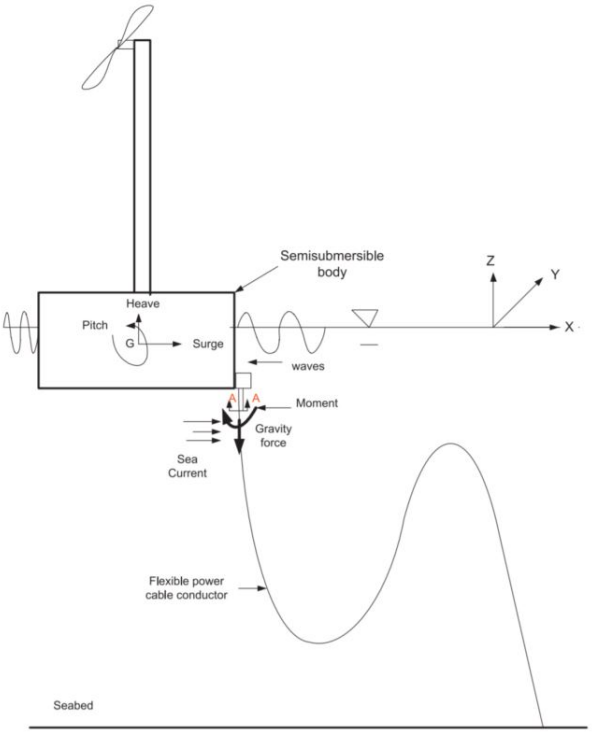

Figure 3.4.7: Dynamic flexible power cable attached to semi-submersible wind turbine, Nasution et al. (2013)

Yang et al. (2017) states that fatigue life is an important parameter in determining service life for a subsea a power cable. Thies et al. (2012) explains that power cables can be used in static applications, where it is connected to a fixed structure, or dynamic application where they have to withstand significant cyclic loading. Due to this, dynamic power cables are subjected to fatigue failure.

There are mainly three causes of mechanical failure in marine power cables applied to marine energy applications, taken from Thies et al. (2012):

- Maximum axial tension
- Over bending
- Fatigue under extreme cyclic loads

According to Karlsen (2010), the individual wires and the intersections between them is what determines the fatigue properties of a copper conductor. R-ratio of loading and wire interaction have been recognized as relevant factors to fatigue life in copper conductors. Fretting fatigue (fatigue due to oscillating load on a junction between two components, Hills (1994)) is identified as one of the dominating mechanisms in multi-layer stranded steel wires. Friction force increases with increasing lay angle and friction coefficient for the material. The copper conductors do not only have contact between conductor surfaces, but also with the protecting sheath around the conductors, giving a complex stress model.

Fatigue of Copper Conductors

According to a study done by Nasution et al. (2013), when testing individual wires as well as a full cross-section of a three-phase 95mm^2, all failures occurred in the inner layer for the cross-section bent over a bell mouth. Also, individual wires from the outer layer of the cross-section were tested in controlled tension-tension loading. Here, all initiation of crack growth happened within or at the edge of the trellis contact area, that has been deformed due to the compacting process of the cable. The study concluded that the difference in fatigue life between layers is due to the variance of surface irregularities. Another study, performed by Nasution et al. (2012) states that the first fatigue failure for a copper conductor subjected to tension-tension fatigue happens in the outer layer. This indicates that the fatigue performance is governed by local effects due to surface irregularities of the different layers.

Analytical Model

Nasution et al. (2014) developed an analytical model for stress variation in individual wires in the conductor cross-section. This model applies for conductors exposed to static and dynamic tension in combination with dynamic curvature. The stress variation can be calculated as:

$$\Delta\sigma = \Delta\sigma_T + \Delta\sigma_{tc} + \Delta\sigma_{nc} + \Delta\sigma_f \tag{3.19}$$

where $\Delta\sigma_T$ is the stress range due to dynamic tension, $\Delta\sigma_{tc}$ is the stress range from transverse curvature of the wire, $\Delta\sigma_{nc}$ is the stress range from normal curvature of the wire and $\Delta\sigma_f$ is the stress range from friction. By looking at a point with the polar coordinate angle $\psi = 0$ and including SCF, Equation 3.19 can be reduced to:

$$\Delta\sigma = (\Delta\sigma_f + \Delta\sigma_T) \cdot \mathrm{SCF} + \Delta\sigma_{nc} \tag{3.20}$$

Where SCF is the stress concentration factor.

The stress variation in the individual wires due to dynamic tension can be found from:

$$\Delta\sigma_T^i = E\cos^2\alpha_i \frac{\Delta T}{EA_{full}} \tag{3.21}$$

where E is the Young's modulus of the material, ΔT is the tension range and EA_{full} is the axial stiffness of the full cross-section of the conductor and can be found from:

$$EA_{full} = EA\left(1 + \sum_{i=1}^{m} n_i \cos^3\alpha_i\right) \tag{3.22}$$

where EA is the axial stiffness of each wire, n_i is the number of wires in layer i, and α_i is the lay angle of layer i.

The bending stress range from normal curvature of the wires for small lay angles can be approximated as:

$$\Delta\sigma_{nc} = R_{nominal}E\cos^2\alpha_i \cos 2\alpha_i \Delta\kappa \cos\Psi \approx R_{nominal}E\Delta\kappa \tag{3.23}$$

where $\Delta\kappa$ is the curvature range and Ψ is the polar coordinate angle defining the helix position (assuming $\psi = 0$).

The friction stress range will be the smallest stress range from either the plane surfaces remain plane solution or maximum allowed due to friction between the interfaces:

$$\Delta\sigma_f^i = \min\left(E\cos^2\alpha_i R_i \Delta\kappa, \frac{\pi R_i \tau_i}{\sin\alpha_i A_i}\right) \tag{3.24}$$

where R_i is the helix radius of the layer i, and τ_i is the friction force per unit length, and can be determined by:

$$\tau_i \cong E\epsilon_c\mu\left(\sum_{j=i+1}^{m}\frac{n_j A_j\cos^2\alpha_j\sin^2\alpha_j}{n_i R_i} + \sum_{j=i}^{m}\frac{n_j A_j\cos^2\alpha_j\sin^2\alpha_j}{n_j R_i}\right) \tag{3.25}$$

where μ is the coefficient of friction and ϵ_c can be found from:

$$\epsilon_c = \frac{T}{EA_{full}} \tag{3.26}$$

where t is tension

Chapter 4

Case Scenario

To studyn the fatigue of dynamic power cable applied in offshore wind, a realistic case study was examined. In this chapter, the chosen concept is described as well as the weather conditions at the proposed location and SN fatigue data.

4.1 Floating Wind Turbine

OO-Star was chosen as the floating wind turbine for the case study. It is a design by Dr. Techn. Olav Olsen, and the project Lifes50+ was used as a groundwork for the design and other relevant information.

4.1.1 Lifes50+

Lifes50+ is a comprehensive research project whose objective is to develop cost-effective floating solutions for 10MW wind turbines. The project is funded by the Horizon 2020 program, "[...]the biggest EU research and innovation program ever, with nearly 80 billion euros of funding available over 7 years (2014-2020)", Horizon 2020 (n.d.). According to Dr. Techn. Olav Olsen (n.d.), the total budget on the project is 7.3 million euros. There are 12 partners associated with the project, including DNV GL and SINTEF. The project consists of 4 different designs and 3 different locations, with water depths deeper than 50m. Figure 4.1.1 presents the different designs in the project, and Figure 4.1.2 shows the different locations in the project.

Figure 4.1.1: The different concepts of the Lifes50+ project, Lifes50+ (n.d.)

Figure 4.1.2: The different sites for Lifes50+ project, Lifes50+ (2017)

4.1.2 OO-Star

OO-Star is one of the two designs to proceed to the second stage of the project. It is a design developed by the Norwegian company Dr. Techn. Olav Olsen.

The support structure is a semi-submersible consisting of one column in the center supporting the tower and turbine, and three outer columns equally spaced, all mounted on a star-shaped pontoon, as can be seen in Figure 4.1.3

Figure 4.1.3: Dr. Techn. Olav Olsen's OO-Star, Lifes50+ (2018)

OO-Star's primary material is post-tensioned concrete, and its main dimensions are displayed in Figure 4.1.4

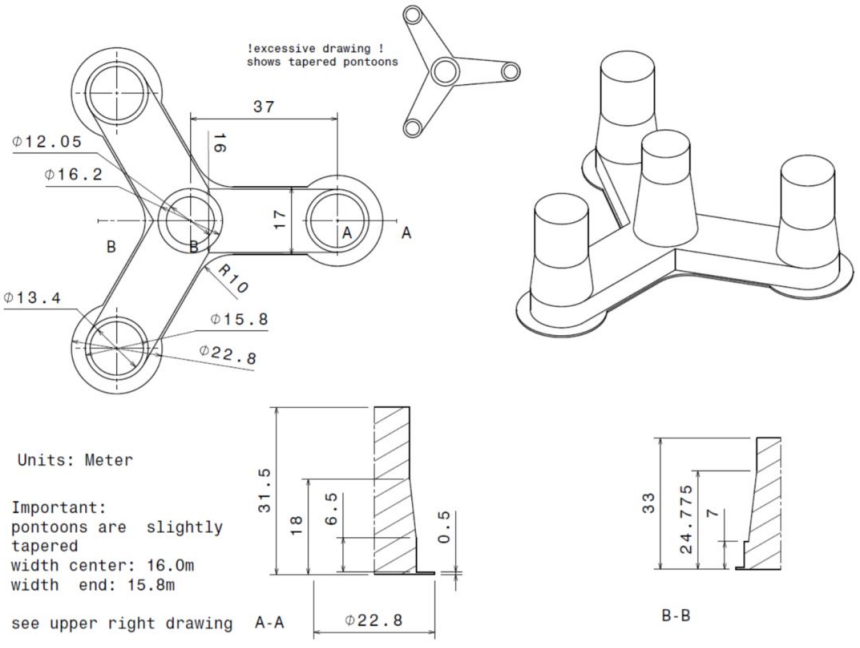

Figure 4.1.4: Main dimensions of OO-Star, Lifes50+ (2018)

4.1.3 Wind Turbine Floater Motions

To reproduce the motion of OO-Star, Dr. Techn. Olav Olsen provided the transfer functions for all 6 degrees of freedom of the vessel. The transfer functions apply for the center of the model, but the cable was attached some distance from the center of gravity as can be seen in Figure 4.1.5. The distance between the center and the cable hang off was 9.24m, and was accounted for in the modeling process. The transfer functions of OO-Star are confidential and could not be reproduced in this report.

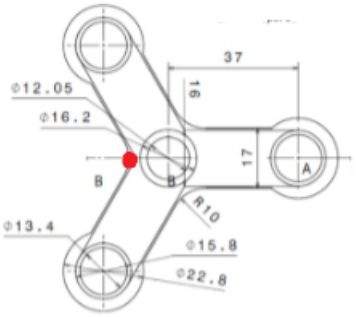

Figure 4.1.5: Cable hang off position, modified from Lifes50+ (2018)

4.2 Power Cable

The power cable used in this master thesis had three-phase AC circuits placed in one cable. The choice of power cable cross-section was based on guidance from Professor Svein Sævik.

4.2.1 Cable Cross-section

An illustration of the cable cross-section is shown in Figure 4.2.1.

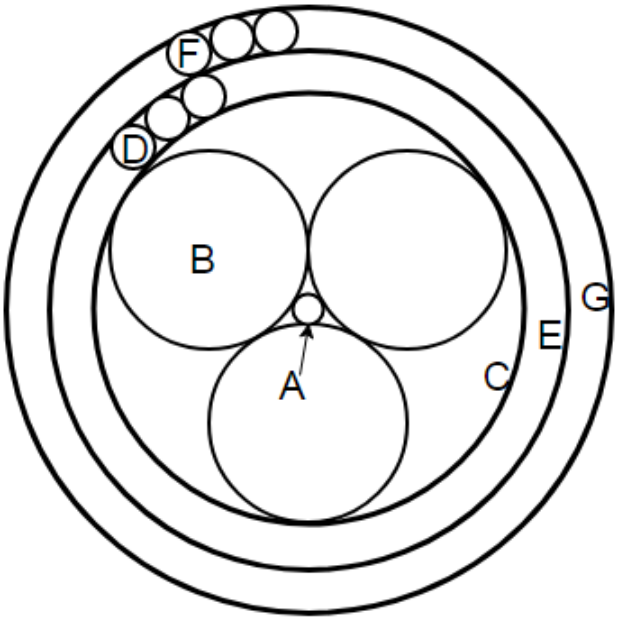

Figure 4.2.1: Illustration of cable cross-section

The different components in the local model were:

A Center tube

B Electrical conductor + insulation

C Sheath around conductors

D 1st layer of armoring

E Tape between the two layers of armoring

F 2nd layer of armoring

G Protective sheath

The dimensions of the components of the cross-section are based on the conductor + insulation cross-section. The conductor itself had an area of $95mm^2$, and combined with a layer of insulation, the radius of the conductor + insulation was 15mm. The calculations of the radius of the center tube and the 1st sheath were based on trigonometry. By imagining a like-sided triangle with its corners in the center of each of the conductors, the following relations was be derived:

$$r_{ct} = r_c(\tan(60) - \tan(30) - 1) \tag{4.1}$$

where r_{ct} is the radius of the center tube and r_c is the radius of the conductor.

$$r_s = r_c(1 + \tan(60) - \tan(30)) \tag{4.2}$$

where r_s is the radius of the sheath around the conductors and r_c is the radius of the conductor.

The dimensions of the cable cross-section are given in Table 4.1.

Component	Radius [mm]	Thickness [mm]
Conductor + Insulation	15	
Center tube	2.32	
Sheath 1	33.07	1.5
Armouring	1.5	
Tape	37.57	0.5
Sheath 3	42.82	3

Table 4.1: Dimensions of the local model

There were 63 steel armoring fibers in the inner layer of the armoring, and 71 in the outer layer, determined by the following expression:

$$n_i = \frac{F_j \cos(\alpha)\pi D_c}{D_s} \tag{4.3}$$

where F_j is the fill factor (0.9 was used), α is the lay angle (20 degrees was used), D_c is the diameter of the cable and D_s is the diameter of one steel fibre.

4.3 Environmental Conditions

This section contains information mainly from the Report Lifes50+ (2015).

The main basis for choosing West of Barra as case location was its deep water and challenging weather conditions. The exact proposed location was in the area with the coordinates 56.609°N, 7.996°W, see Figure 4.3.1. The water depth at the location is between 56-118m, and 118m was used in this study.

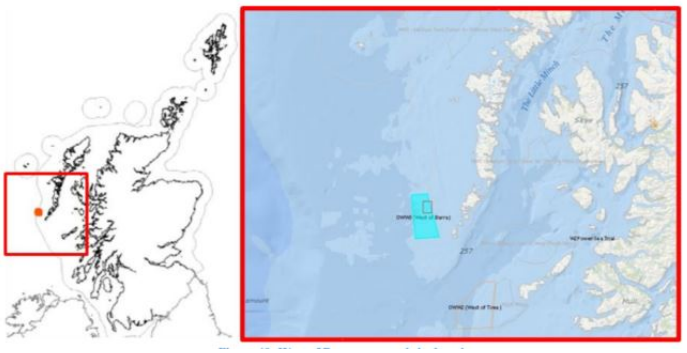

Figure 4.3.1: West of Barra, Scotland,, Lifes50+ (2015)

4.3.1 Wind Climate

The wind speeds at West of Barra are high and reliable throughout the year, with a mean annual power density of 1.3 $\frac{kW}{m^2}$. The following wind and wave data are based on Geos (2001), and extrapolated and modified by Lifes50+ (2015).

Table 4.2 shows the ten minute mean wind speed profile at different heights, and extreme value wind speed is shown in Table 4.3

Height [m]	Wind speed [m/s]
10	9.50
20	10.16
50	10.97
120	11.58
119	11.74

Table 4.2: Ten minute mean wind speed profile, Lifes50+ (2015)

Height [m]	Wind speed [m/s]
10	26.47
20	35.63
50	44.13
120	48.97
119	50.00

Table 4.3: Ten minute mean extreme value speed profile, Lifes50+ (2015)

Figure 4.3.2 shows the scatter diagram for wind conditions at West of Barra, With north being 0 degrees.

Mean Wind Speed at 10 m [m/s]	Mean Wind Direction [°] [19]							
	0	45	90	135	180	225	270	315
0,00-0,30								
0,30-1,60	2	4	6	2	3	4	2	
1,60-3,40	333	413	403	430	535	469	366	326
3,40-5,50	1091	1138	1116	1229	1515	1527	1576	1170
5,50-8,00	1932	1385	1395	1782	2668	3385	3049	2217
8,00-10,80	1421	1294	1105	1841	3496	4850	3750	2016
10,80-13,90	928	641	510	1408	2847	4729	3451	1420
13,90-17,20	397	215	192	605	1576	3035	1782	549
17,20-20,80	52	55	68	162	561	948	731	160
20,80-24,50	5	5	1	30	86	182	132	46
24,50-28,50					3	27	46	10
28,50-32,70							1	1
32,70-51,50								

Figure 4.3.2: Scatter diagram for wind conditions at West of Barra, Lifes50+ (2015)

The maximum annual wind speed at 10 m above sea surface with 1-year return period was calculated by Lifes50+ (2015) to be 29.36 $\frac{m}{s}$

4.3.2 Wave Climate

The wave loads applied to the floating wind turbine were based on the scatter diagram for West of Barra. Due to the nature of the transfer functions, resonance occurred in several of the analyses and modifications to the scatter diagram were inevitable to enable the study. To avoid the area of severe resonance, an thus extreme response for the wind floater, the sea states for the periods 16 -17, 17-18 seconds and 18-19 seconds were moved to the 15-16 seconds column, and thus maintaining the total number of observations. The original and modified scatter diagrams can be seen in Figures 4.3.3 and 4.3.4.

Hs	Tp [s]																				
[m]	0-1	1-2	2-3r	3-4r	4-5	5-6	6-7	7-8	8-9	9-10	10-11	11-12	12-13	13-14	14-15	15-16	16-17	17-18	18-19	19-20	20-21	21-22
0.0-0,5			1																			
0.5-1,0				129	337	681	581	1242	774	341	88	24	11	40	28	11						
1.0-1,5				18	589	1721	1189	2403	3333	1824	754	284	120	23	20	6						
1.5-2,0					21	1260	1855	1644	2765	2720	1444	744	235	131	50	27	3	2				
2.0-2,5				1	4	164	1804	1614	1843	2055	1773	1273	562	222	40	31		4	1			
2.5-3,0					1	8	607	1536	1290	1462	1659	1184	686	338	101	40	1	8	3			
3.0-3,5							85	989	970	1014	1170	1140	749	265	167	61	11	9	1			
3.5-4,0							10	397	846	859	971	873	754	319	221	76	20	5				
4.0-4,5							1	53	646	706	744	893	791	353	206	127	30	4				
4.5-5,0								8	221	529	586	790	659	414	167	76	44	27	4			
5.0-5,5									44	340	558	517	441	250	252	56	9	10	4			
5.5-6,0									7	169	293	433	424	214	182	75	9	16				
6.0-6,5									1	67	101	315	263	186	100	54	21	13	6			
6.5-7,0										3	42	220	301	218	101	35	17	13	2			
7.0-7,5											15	106	160	156	69	54	17	1				
7.5-8,0											8	32	145	117	59	50	1	4				
8.0-8,5												10	121	112	67	37		3				
8,5-9,0												3	115	148	62	25	4	2				
9,0-13,5													78	277	321	197	15	21				

Figure 4.3.3: Original wave scatter diagram,Lifes50+ (2015)

Scatter Diagram

		TP															
		0.0	1.0	2.0	3.0	4.0	5.0	6.0	7.0	8.0	9.0	10.0	11.0	12.0	13.0	14.0	15.00
HS		1.0	2.0	3.0	4.0	5.0	6.0	7.0	8.0	9.0	10.0	11.0	12.0	13.0	14.0	15.0	16.00
0	0.50			1													
0.5	1.00				129	337	681	581	1241	774	341	88	24	11	40	28	11
1	1.50				18	589	1721	1189	2403	3333	1824	754	2284	120	23	20	6
1.5	2.00					21	1260	1855	1644	2765	2720	1444	744	235	131	50	32
2	2.50				1	4	164	1804	1614	1843	2055	1773	1273	562	222	40	36
2.5	3.00					1	8	607	1536	1290	1462	1659	1184	686	338	101	52
3	3.50							85	989	970	1014	1170	1140	749	265	167	82
3.5	4.00							10	397	846	859	971	873	754	319	221	101
4	4.50							1	53	646	706	744	893	791	353	206	161
4.5	5.00								8	221	529	586	790	659	414	167	151
5	5.50									44	340	558	517	441	250	252	79
5.5	6.00									7	169	293	433	424	214	182	100
6	6.50									1	67	101	315	263	186	100	94
6.5	7.00										3	42	220	301	218	101	67
7	7.50											15	106	160	156	69	72
7.5	8.00											8	32	145	117	59	55
8	8.50												10	121	112	67	40
8.5	9.00												3	115	148	62	31
9	13.50													78	277	321	233

Figure 4.3.4: Modified wave scatter diagram

4.3.3 Current

According to Lifes50+ (2015), the coast of Scotland is located on the UK Continental Shelf, so that it is directly affected by the oceanic circulations. However, the amount of water traveling from deep waters of the Atlantic sea to the shallower waters of the continental shelf is reduced due

to the steepness of the slope of the shelf. Tidal currents are stronger and easier to predict than the non-tidal currents in the area. Winds, jets, and density-driven currents affect the non-tidal currents strongly, and this may lead to large changes in the general current patterns for short periods. There are no specific data on the current conditions of West for Barra. However, according to Det Norske Veritas (DNV) (2014), when detailed field measurements are missing, the current speed profile can be described with two components: wind-generated current and tidal current. The current profiles was calculated as follows:

Wind Generated Current

The wind-induced current speed at still water level (z=0) can be calculated, if no statistical data is available, as:

$$V_{c,wind}(0) = kU_{1hour,10m} \tag{4.4}$$

where k is a constant in range 0.015-0.03, and $U_{1hour,10m}$ is the 1 hour wind speed at height 10 m above sea level.

By using $k = 0.03$ and and $29.36\frac{m}{s}$ as current speed at still water level (see Section 4.3.1), the current speed at still water level was calculated to:

$$V_{c,wind}(0) = 0.881$$

Then the current speed profile was calculated as a linear profile from $d_0 < z < 0$:

$$V_{c,wind}(z) = V_{c,wind}(0)\left(\frac{d_0 + z}{d_0}\right) \tag{4.5}$$

where $V_{c,wind}(z)$ is the current speed at still water level, d_0 is the reference depth for wind-generated current d_0=50m, and z is the distance from still water level, positive upwards.

Deep Water Current

The data in this section is taken from Health Safety Executive (HSE) (2001) and reproduced by Lifes50+ (2015).

The 50 year return period speed and directions for tidal current and storm surge current was found to be 0.44 m/s with North-East direction, and 0.6 m/s with North direction respectively. Subsequently, the 1 year return period velocities can be calculated by a correction factor of 0.89. The combined velocity and direction were calculated as the vectorial sum of the two components, as in Table 4.4.

Return Period	Tidal Current		Storm Surge Current		Combined Current	
	Vc[m/s]	Dir[°]	Vc[m/s]	Dir[°]	Vc[m/s]	Dir[°]
1	0.39	50	0.53	0	0.84	21
50	0.44	50	0.60	0	0.94	21

Table 4.4: Deep Water Current at Sea Surface, Lifes50+ (2015)

According to Det Norske Veritas (DNV) (2014), the 1 year return period data from Table 4.4 can be used to calculate the tidal and storm surge current profile for $z \leq 0$:

$$V_{c,tide}(z) = V_{c,tide}(0) \left(\frac{d+z}{d_0} \right)^{\alpha} \tag{4.6}$$

where $V_{c,tide}(z)$ is the current speed at still water level, d is the water depth to still water level (taken positive), and z is the distance from still water level, positive upwards, α is the exponent, typically $\alpha = \frac{1}{7}$.

Current Speed Profile

As a simplification, only three different weather conditions were considered:

- Far: Wind direction and wind induced current direction is the same as wave direction
- Neutral: No wind, only tide and storm surge current
- Near: Wind direction and wind induced current direction is the opposite to wave direction

The current profiles for the three weather conditions were calculated as the vectorial sum of the wind induced current and the tidal- and storm surge current. The profiles are displayed in Tables 4.5 to 4.7, where north is defined as 0°:

Depth [m]	Wind		Tidal and Surge		Total Current Profile	
	Vc[m/s]	Dir[°]	Vc[m/s]	Dir[°]	Vc[m/s]	Dir[°]
0	0.881	270	1.023	21	1.085	331.70
-10	0.705	270	1.008	21	1.010	340.49
-20	0.528	270	0.992	21	0.942	349.47
-30	0.352	270	0.973	21	0.908	364.79
-40	0.176	270	0.952	21	0.904	10.48
-50	0.0	-	0.928	21	0.928	21
-60	0.0	-	0.900	21	0.900	21
-70	0.0	-	0.864	21	0.864	21
-80	0.0	-	0.817	21	0.817	21
-90	0.0	-	0.741	21	0.741	21
-100	0.0	-	0.0	-	0.0	-

Table 4.5: Current Speed and Direction Profile for near wind condition, partly from Lifes50+ (2015)

Depth [m]	Wind		Tidal and Surge		Total Current Profile	
	Vc[m/s]	Dir[°]	Vc[m/s]	Dir[°]	Vc[m/s]	Dir[°]
0	0.0	-	1.023	21	1.023	21
-10	0.0	-	1.008	21	1.008	21
-20	0.0	-	0.992	21	0.992	21
-30	0.0	-	0.973	21	0.973	21
-40	0.0	-	0.952	21	0.952	21
-50	0.0	-	0.928	21	0.928	21
-60	0.0	-	0.900	21	0.900	21
-70	0.0	-	0.864	21	0.864	21
-80	0.0	-	0.817	21	0.817	21
-90	0.0	-	0.741	21	0.741	21
-100	0.0	-	0.0	-	0.0	-

Table 4.6: Current Speed and Direction Profile for neutral wind condition, partly from Lifes50+ (2015)

Depth [m]	Wind		Tidal and Surge		Total Current Profile	
	Vc[m/s]	Dir[°]	Vc[m/s]	Dir[°]	Vc[m/s]	Dir[°]
0	0.881	90	1.023	21	1.571	52.56
-10	0.705	90	1.008	21	1.421	48.57
-20	0.528	90	0.992	21	1.279	43.65
-30	0.352	90	0.973	21	1.147	37.64
-40	0.176	90	0.952	21	1.029	30.19
-50	0.0	-	0.928	21	0.928	21
-60	0.0	-	0.900	21	0.900	21
-70	0.0	-	0.864	21	0.864	21
-80	0.0	-	0.817	21	0.817	21
-90	0.0	-	0.741	21	0.741	21
-100	0.0	-	0.0	-	0.0	-

Table 4.7: Current Speed and Direction Profile for far wind condition, partly from Lifes50+ (2015)

4.4 SN Fatigue Data

The S-N curve in Figure 4.4.1 was used to estimate the lifetime of the power cable.

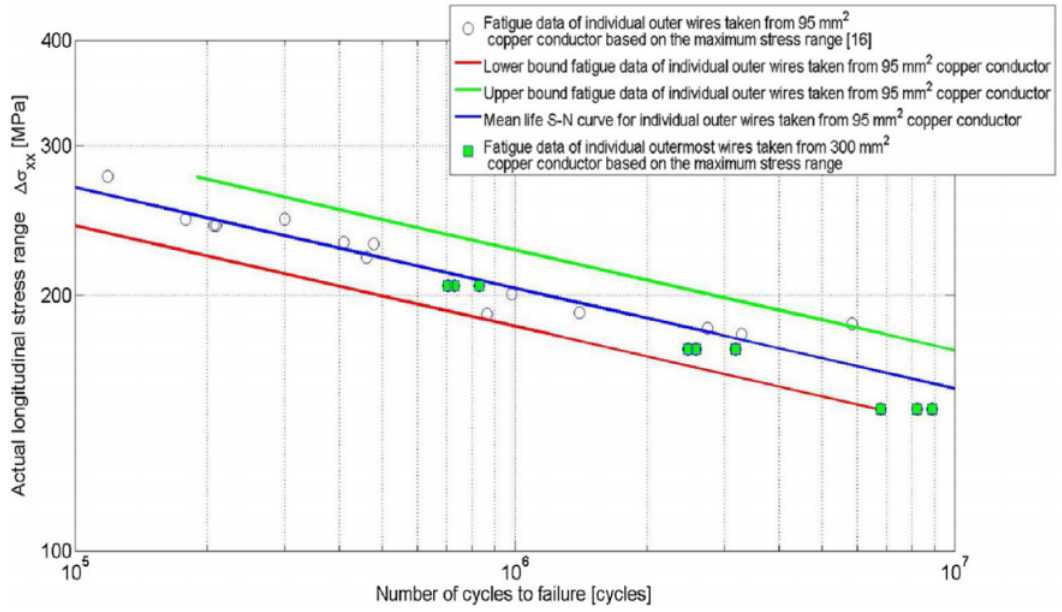

Figure 4.4.1: S-N data for case scenario, Nasution et al. (2014)

The blue SN-cCurve follows the log-linear relationship of Equation 3.11, with m=8.424 and c=2.88e25, according to Nasution et al. (2013). The red plot is the SN-Curve with two standard deviations subtracted, that was used in this study. The constants of the red plot are m=8.424 and c=1.57e25.

Chapter 5

Numeric Models

In this chapter, the numeric theory behind the two models used to analyze the fatigue of the dynamic power cable is presented.

5.1 The Finite Element Method

The finite element method is a numerical procedure for solving differential equations and is often used in analyses of structures. The finite element method gives an approximate solution, with increasing accuracy with decreasing mesh size. According to the Finite Element Theory, for a static linear system, the system relationship is:

$$\boldsymbol{R} = \boldsymbol{K}\boldsymbol{r} \tag{5.1}$$

Where **R** is the global load matrix, **K** is the global stiffness matrix, and **r** is the nodal displacement vector.

This is based on the following principles:

- Equilibrium
- Kinematic compatibility
- Stress-strain relationship

Moan (2003)

5.1.1 Principle of Virtual Work

The element stiffness relationship can be derived based on virtual work (Galerkin's Method). This method assumes a displacement for each element so that the displacement is continuous between elements. The method can be generalized and used for all kinds of structural problems in all dimensions, Moan (2003). The method gives an approximation rather than the exact solution. This is done by, on average, fulfilling the differential equations in the problem. By setting the internal work equal to the external work, it is assumed that the error from assuming the weight function in the external work is equal to the error in the internal work. If the weight functions are selected so that the boundary conditions are fulfilled appropriately, the error in the external work will cancel out. This means that the total error in the volume integration is zero on average, but

at an arbitrary point, the equilibrium equation is not necessarily fulfilled. This is referred to as integrated equilibrium. The principle of virtual work in a body with deformed volume and surfaces in equilibrium:

$$\int_v (\rho \ddot{\boldsymbol{u}} - \boldsymbol{f}) \cdot \delta \boldsymbol{u} dV + \int_V \boldsymbol{\sigma} : \delta \epsilon dV - \int_S \boldsymbol{t} \cdot \delta \boldsymbol{u} dS = 0 \tag{5.2}$$

where V refers to the volume, ρ is the material density, $\ddot{\boldsymbol{u}}$ is the acceleration field, $\boldsymbol{f}$ is the volume force vector, δ is the virtual displacement, $\boldsymbol{\sigma}$ is the stress tensor, ϵ is the natural strain tensor, $\boldsymbol{t}$ is the surface traction, $\boldsymbol{u}$ is the displacement vector and S refers to the surface, Sævik (2013).

5.2 Method for Static calculation

5.2.1 Static Non-linear Theory

According to Moan (2003), a system is non-linear if it contains non-linear material, large displacements or geometry non-linearity. For non-linear problems, the stiffness will depend on the displacement:

$$\boldsymbol{R} = \boldsymbol{K}(\boldsymbol{r})\boldsymbol{r} \tag{5.3}$$

The stiffness matrix is often written on differential form, with the incremental stiffness matrix, K_I:

$$d\boldsymbol{R} = \frac{d}{d\boldsymbol{r}}(\boldsymbol{K}(\boldsymbol{r})\boldsymbol{r})d\boldsymbol{r} \tag{5.4}$$

$$d\boldsymbol{R} = \boldsymbol{K_I}(\boldsymbol{r})d\boldsymbol{r} \tag{5.5}$$

In general it can be challenging to determine $\boldsymbol{r}$ for a given $\boldsymbol{R}$ analytically, and thus iterative methods will have to be used. Only the methods relevant for this project will be presented in the report.

5.2.2 Combined Method

The combined method is a combination of the Euler-Cauchy Method and the Newton-Raphson Method.

Euler-Cauchy Method

This method it an incremental method, meaning that the external load is applied step-wise. For each step the displacement increment $\boldsymbol{\Delta r}$ is determined. The total displacement is then calculated by adding the incremental displacements. The incremental stiffness matrix $\boldsymbol{K_I}$ is constant for each increment, and is calculated for each step based on the current displacement and stress before a new load increment is added. This is illustrated in Figure 5.2.1. For load increment number (m+1):

$$\Delta \boldsymbol{r_{m+1}} = \boldsymbol{K_I}(\boldsymbol{r_m})^{-1} \Delta \boldsymbol{R_{m+1}} \tag{5.6}$$

where:

$$\Delta \boldsymbol{R_{m+1}} = \boldsymbol{R_{m+1}} - \boldsymbol{R_m} \tag{5.7}$$

$$\boldsymbol{r_{m+1}} = \boldsymbol{r_m} + \Delta \boldsymbol{r_{m+1}} \tag{5.8}$$

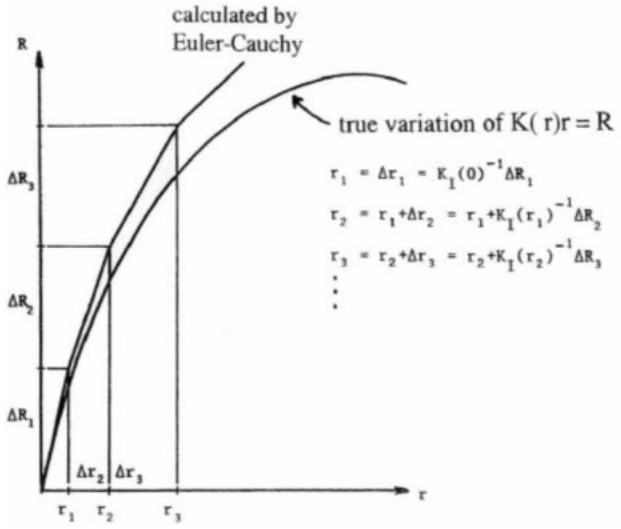

Figure 5.2.1: Euler-Cauchy Method, Moan (2003)

As the incremental stiffness from the previous increment is used, it will only give an approximation, and does not fulfill total equilibrium. This can be seen in Figure 5.2.1 where the approximation is plotted with the true solution. More accurate results will be obtained by using smaller increment size and by equilibrium corrections.

Newton Raphson Method

The Newton-Raphson Method is an iterative method, and is based on the Newton-Raphson Algorithm:

$$x_{n+1} = x_n - \frac{f(x_n)}{f'(x_n)} \tag{5.9}$$

where $f'(x_n)$ is the derivative of $f(x)$ at $x = x_n$. This is illustrated in Figure 5.2.2, and the algorithm can be generalized to solve Equation 5.5:

$$\boldsymbol{r_{n+1} = r_n - K_I^{-1}(r_n)(R_{int} - R)} \tag{5.10}$$

This method requires that Δr_{n+1} is solved for from

$$\boldsymbol{R - R_{int} = K_{I(n)} \Delta r_{n+1}} \tag{5.11}$$

and that K_I is established.

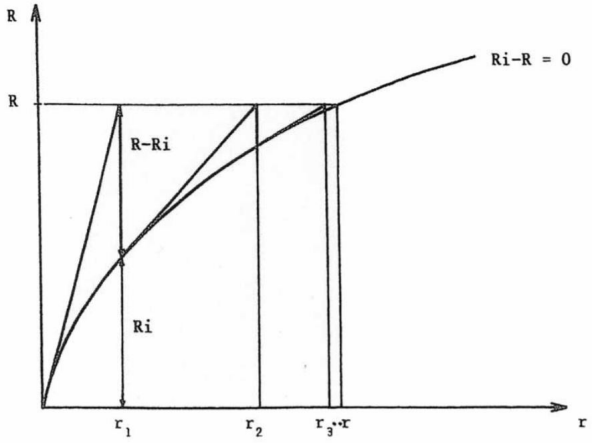

Figure 5.2.2: Newton-Raphson Iteration, Moan (2003)

Newton-Raphson method is time consuming, but calculation time can be improved by updating $\boldsymbol{K_I}$ less frequently. This is called the modified Newton-Raphson method, and usually gives slower convergence. The iteration ends when the displacement from one iteration to the next is smaller than the convergence criteria:

$$||\boldsymbol{r_{n+1}} - \boldsymbol{r_n}|| < \epsilon \tag{5.12}$$

Combined Method

When combining the two methods, load is applied according to the Euler-Cauchy method, and iteration until equilibrium is done according to the modified Newton-Raphson method for each increment as illustrated in Figure 5.2.3. The method is considered to be effective as long as the load curve is increasing with displacement. For extremal points in the load-displacement curve, additional procedures need to be implemented.

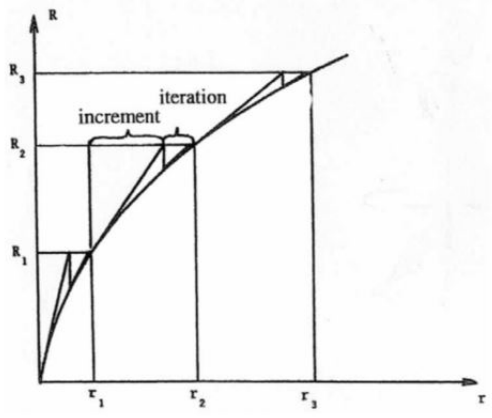

Figure 5.2.3: Combined Method, Moan (2003)

5.3 Method for Dynamic Calculation

Dynamic analysis has to be considered when external loads are not applied in a very slow manner. Dynamic loads are different from static loads by implying a time dependent solution and by introducing inertia loads throughout the structure, and often also damping. The equilibrium Equation for a dynamic system is stated by Langen & Sigbjörnsson (1979) as:

$$\boldsymbol{M}\ddot{\boldsymbol{r}} + \boldsymbol{C}\dot{\boldsymbol{r}} + \boldsymbol{K}\boldsymbol{r} = \boldsymbol{Q}(t) \tag{5.13}$$

A variation of Equation 5.13 is the semi-discrete global equation describing the instantaneous equation of motion of a non-linear system at time t. This relation is presented by Mathisen (1990) as:

$$\boldsymbol{R^I} + \boldsymbol{R^D} + \boldsymbol{R^S} = \boldsymbol{R^E} \tag{5.14}$$

Where $\boldsymbol{R^I}$ is the inertia force vector, $\boldsymbol{R^D}$ is the damping force vector, $\boldsymbol{R^S}$ is the internal force vector and $\boldsymbol{R^E}$ is the external force vector.

The inertia forces relate to the mass matrix as:

$$\boldsymbol{R^I} = \boldsymbol{R^I}(\ddot{\boldsymbol{r}}, \dot{\boldsymbol{r}}, \boldsymbol{r}, t) = \boldsymbol{M}(\ddot{\boldsymbol{r}}, \dot{\boldsymbol{r}}, \boldsymbol{r}, t)\boldsymbol{r} \tag{5.15}$$

The internal forces $\boldsymbol{R^S}$ can be established by:

$$\frac{\partial \boldsymbol{R^S}}{\partial \boldsymbol{r}} = \boldsymbol{K^M} + \boldsymbol{K^G} \tag{5.16}$$

The total tangential stiffness is now:

$$\boldsymbol{K_T} = \boldsymbol{K_T}(\ddot{\boldsymbol{r}}, \dot{\boldsymbol{r}}, \boldsymbol{r}, t) = \boldsymbol{K^M} + \boldsymbol{K^G} + \boldsymbol{K^{NC}} \tag{5.17}$$

$$\boldsymbol{K^{NC}} = \boldsymbol{K^{NC}}(\ddot{\boldsymbol{r}}, \dot{\boldsymbol{r}}, \boldsymbol{r}, t) = \frac{\partial \boldsymbol{R^{NC}}}{\partial \boldsymbol{r}} \tag{5.18}$$

Where $\boldsymbol{K^M}$ and $\boldsymbol{K^G}$ are the material and geometric stiffness matrices respectively, and $\boldsymbol{K^{NC}}$ is the total external non-conservative external forces.

The equivalent damping force can be expressed as:

$$\boldsymbol{R_D} = \boldsymbol{R_D}(\ddot{\boldsymbol{r}}, \dot{\boldsymbol{r}}, \boldsymbol{r}, t) = \boldsymbol{C_T}\dot{\boldsymbol{r}} \tag{5.19}$$

And the tangential damping matrix is:

$$\boldsymbol{C_T} = \boldsymbol{C_T}(\ddot{\boldsymbol{r}}, \dot{\boldsymbol{r}}, \boldsymbol{r}, t) = \alpha_1 \boldsymbol{M} + \alpha_2 \boldsymbol{K_T} + C_d \tag{5.20}$$

Where α_1 and α_2 are the damping coefficients for the Rayleigh damping and C_d is the damping coefficient matrix for additional discrete nodal points.

The dynamic equilibrium equation is an initial value problem, meaning that start values determine the solution. Practical numerical integration methods use a step-by-step approach, where the time interval is divided into sub-intervals with step length h. Displacement, velocity, and acceleration are known for the beginning of the sub-interval, and the solution for the end of the sub-interval is calculated by assuming the variation of the acceleration over the time step. The computed value is used to determine the velocity and displacement across the time step, and they

are the start values for the next sub-interval. This way, an approximated solution is calculated at instants along the time axis, and accuracy increases as h decreases, Langen & Sigbjörnsson (1979).

How the acceleration changes during a time step is suggested by several methods and can be explicit or implicit. A non-linear implicit method requires iteration at each time step to establish for each time step, while this is not necessary for an explicit method. Only the methods relevant to this master thesis are presented

5.3.1 Newmark's $\boldsymbol{\beta}$ Family

Newmark-$\boldsymbol{\beta}$ is a family of numerical integration of the dynamic equilibrium equations. It can easily be derived from assuming a constant average acceleration over the time step. The following equations are taken from SINTEF Ocean (2017) and Mathisen (1990):

$$\boldsymbol{M_t\ddot{r}_{t+\Delta t} + C_{T,t}\dot{r}_{t+\Delta t} + R^S_{t+\Delta t} = R^E_{t+\Delta t}} \tag{5.21}$$

$$\boldsymbol{\dot{r}_{t+\Delta t} = \dot{r}_t + (1-\gamma)\ddot{r}_t\Delta\tau + \gamma\ddot{r}_{t+\Delta t}\Delta\tau} \tag{5.22}$$

$$\boldsymbol{r_{t+\Delta t} = r_t\Delta\tau + (\frac{1}{2} - \beta)\ddot{r}_t(\Delta\tau)^2 + \beta\ddot{r}_{t+\Delta t}(\Delta\tau)^2} \tag{5.23}$$

where $\Delta\tau = \theta\Delta t, \leq 1.0$

γ and β are parameters defining the change in acceleration, velocity and displacement vectors in time step, Δt. Langen & Sigbjörnsson (1979) explains that the equations are obtained from Taylor-series expansion. Different values of these parameters give different methods in the Newmark-$\boldsymbol{\beta}$ family. γ represents the numerical damping, taken from SINTEF Ocean (2017):

- $\gamma > \frac{1}{2}$: Positive numerical damping
- $\gamma < \frac{1}{2}$: Negative numerical damping
- $\gamma = \frac{1}{2}$: No numerical damping

$\gamma = \frac{1}{2}$ is customarily used to assure second order accuracy and stability. According to Mathisen (1990), the Newmark-$\boldsymbol{\beta}$ method may have difficulties with solving non-linear problems if they are not discretized in the right way.

In dynamic analysis, the higher modes are of little interest, and these can be removed by introducing an increased damping ratio. The Newmark's $\boldsymbol{\beta}$ Family removes the medium modes, and not affecting the lowest and highest modes. The higher modes can be removed by introducing numerical damping, but it is at the cost of accuracy. The method can be applied both for linear and non-linear analysis, SINTEF Ocean (2017).

5.3.2 Modified Hilber-Hughes-Taylor Method

The problem with accuracy when removing the higher modes can be fixed by using Hilber-Hughes-Taylor Method, often referred to as HHT-α. The method maintains accuracy while introducing

artificial damping of the higher modes. This is done through the modification of Equation 5.21.

$$\begin{aligned} \boldsymbol{M_t}\ddot{\boldsymbol{r}}_{\boldsymbol{t+\Delta t}} + (1+\alpha_H)\boldsymbol{C_{T,t}}\dot{\boldsymbol{r}}_{\boldsymbol{t+\Delta t}} - \alpha_H \boldsymbol{C_{T,t}}\dot{\boldsymbol{r}}_n + (1+\alpha_H)\boldsymbol{R^S_{t+\Delta t}} - \alpha_H \boldsymbol{R^S_t} \\ = (1+\alpha_H)\boldsymbol{R^E_{t+\Delta t}} - \alpha_H \boldsymbol{R^E_t} \end{aligned} \tag{5.24}$$

The method is unconditionally stable when:

- $-\frac{1}{3} \leq \alpha_H \leq 0$
- $\gamma = \frac{1}{2}(1-2\alpha_H)$
- $\beta = \frac{1}{4}(1-\alpha_H)^2$

The method is effectively suppressing high frequency and also retains second-order accuracy, Mathisen (1990).

5.4 Global Model in SIMA RIFLEX

SIMA RIFLEX is a computer program made for analyzing slender structures, such as flexible risers and mooring lines, developed by SINTEF Ocean. The Combined Method is used for the static calculation, and Newmark-$\boldsymbol{\beta}$ is used for dynamic analysis. These methods are described in Section 5.2.2 and 5.3.1 respectively.

5.4.1 Element Formulation

SIMA RIFLEX uses co-rotated ghost reference as element formulation for beam elements. Co-rotated beam elements use Green strain and 2nd Piola-Kirchhoff stresses as the Total Lagrangian formulation, but adapts the procedure of Updated Lagrange formulation where the configuration is updated. This yields the following stiffness matrix:

$$\boldsymbol{K_I} = \boldsymbol{K_0} + \boldsymbol{K_\sigma} \tag{5.25}$$

This is convenient when it is assumed that the initial configuration deforms as a rigid body, and will move and rotate with the motion of the body. At any time the initial configuration is close to the deformed configuration, SINTEF Ocean (2017). Mathisen (1990) explains that each beam element has a local coordinate system, i_i^0 as illustrated in Figure 5.4.1 where the initial configuration C_0 moves as a rigid body with the element and becomes C_{0n}. The deformed beam element will have its local coordinate system rotated, now denoted i_i^a and i_i^b. This forms the reference for the calculation of stresses and strains.

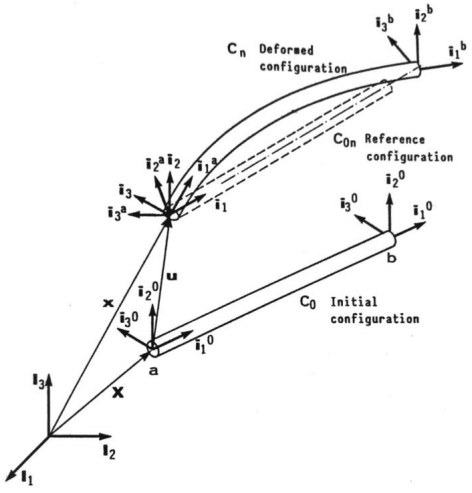

Figure 5.4.1: Co-rotated Ghost Reference, Mathisen (1990)

5.4.2 Element Description

In this section, the relevant element type and its kinematics are presented. Only the element used in the master thesis is included.

Beam Element

SINTEF Ocean (2017) states that the beam element in SIMA RIFLEX has 2 nodes with 6 degrees of freedom for each node, 3 translational and 3 rotational as can be seen in Figure 5.4.2. This is defined in relation to the local Cartesian coordinate system in the initial C0n configuration. It is assumed that straight lines normal to the midplane will remain straight and normal to the midplane, and that strains are small in the element, in accordance with the Kirchhoff Hypothesis.

The displacement of an arbitrary point, P with coordinates x,y, and z can be expressed as the following:

$$u(x, y, z) = u_0(x) - y\frac{dv_0}{dx} - z\frac{dw_0}{dx} \tag{5.26}$$

$$v(x, y, z) = v_0(x) - z\theta \tag{5.27}$$

$$w(x, y, z) = w_0(x) + y\theta \tag{5.28}$$

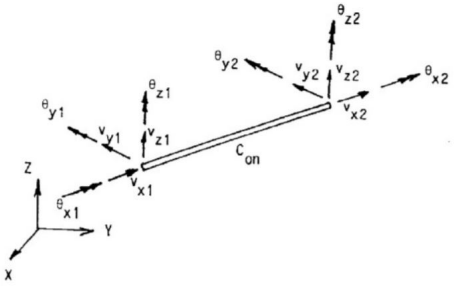

Figure 5.4.2: Degrees of freedom for the beam element, SINTEF Ocean (2017)

5.4.3 Load Model

The loads on the global model are mainly tension due to inertia and weight, as well as external loads due to irregular waves. The theory in this section is mostly taken from SINTEF Ocean (2017).

The inertia forces consist of:

$$\boldsymbol{R^I}(\boldsymbol{r}, \dot{\boldsymbol{r}}) = [\boldsymbol{M^S} + \boldsymbol{M^F}(\dot{\boldsymbol{r}}) + \boldsymbol{M^H}(\dot{\boldsymbol{r}})]\ddot{\boldsymbol{r}} \tag{5.29}$$

Where $\boldsymbol{M^S}$ is the structural mass matrix, $\boldsymbol{M^F}$ is internal flow mass matrix, $\boldsymbol{M^H}$ is hydrodynamic mass matrix.

The damping forces consists of:

$$\boldsymbol{R^D}(\boldsymbol{r}, \dot{\boldsymbol{r}}) = [\boldsymbol{C^S}(\boldsymbol{r}) + \boldsymbol{C^H}(\boldsymbol{r}) + \boldsymbol{C^D}(\boldsymbol{r}, \dot{\boldsymbol{r}})]\dot{\boldsymbol{r}} \tag{5.30}$$

Where $\boldsymbol{C^S}$ is the internal structural damping matrix, $\boldsymbol{C^H}$ is hydrodynamic damping matrix, $\boldsymbol{C^D}$ is matrix of specified discrete dashpot dampers.

The external load vector consists of:

- Weight and buoyancy.
- Forced displacements due to support vessel movements.
- Wave and particle accelerations in accordance to Morison's Equation, (see Equation 3.5).

In SIMA RIFLEX the water velocity and motion are decomposed into x,y and z, where x is in the longitudinal direction and y and z as the symmetry axes for the cross-section.

5.5 Local Model in Bflex

Bflex is a computer program developed by Professor Svein Sævik. Sævik (2013) and Sævik (2017) are used as a basis for this section. The Newton-Raphson Method, described in Section 5.2.2, is used for calculations in the static analysis. While for the dynamic analysis, the Modified HHT-α Method described in Section 5.3.2 is used.

5.5.1 Element Formulation

Bflex also uses co-rotated ghost reference described in Section 5.4.1, where small strains are assumed, but at the same time allowing large rigid body motions due to a 4 base vector system.

By looking at Equation 5.2 for an infinite small increment, Δ, and only including static terms the following is obtained:

$$\int_V \boldsymbol{C} : (\epsilon + \Delta \boldsymbol{E}) : \delta(\epsilon + \Delta \boldsymbol{E}) dV_0 - \int_S (\boldsymbol{t} + \Delta \boldsymbol{t}) \cdot \delta \boldsymbol{u} dS_0 = 0 \tag{5.31}$$

This is used as a basis for the stiffness matrix in Bflex.

5.5.2 Element Descriptions

In this section, the relevant elements and their kinematics are described.

PIPE31

PIPE31 is an elastic element with two nodes and six degrees of freedom in each node. The following stresses are according to Hooke's law:

$$\begin{bmatrix} \sigma_{11} \\ \sigma_{22} \\ \tau \end{bmatrix} = \frac{E}{1-\nu^2} \begin{bmatrix} 1 & \nu & 0 \\ \nu & 1 & 0 \\ 0 & 0 & \frac{1-\nu^2}{2(1+\nu)} \end{bmatrix} \begin{bmatrix} \epsilon_{11} \\ \epsilon_{22} \\ \gamma \end{bmatrix} \tag{5.32}$$

The displacement of an arbitrary point p defined by the local coordinates in the cross-section can be expressed as:

$$u_1(x, y, z) = u_{1,0} - y u_{2,0} - z u_{3,0} \tag{5.33}$$

$$u_2(x, y, z) = u_{2,0} - z\theta_x \tag{5.34}$$

$$u_3(x, y, z) = u_{3,0} - y\theta_x \tag{5.35}$$

Where σ_{ij} is the stress in i,j direction, E is Young's modulus for the material, ν is the Poisson's number, $\epsilon_i j$ is the strain in i,j direction, γ is the shear strain, u_i is the displacement in i direction, and θ is the torsion.

HSHEAR353

Helix beam element with 4 nodes; 2 centroid nodes, and 2 helix nodes. The nodal points have to be defined in polar coordinates. There are 24 active degrees of freedom in the element where 12 are connected to the standard beam degrees of freedom to describe the global strain quantities, and 12 degrees of freedom are used to describe the local displacement of the wire relative to the core as shown in Figure 5.5.1. Due to this, cubic interpolation is possible in all directions, and membrane locking due to curvature coupling is avoided. The torsion DOF at the helix nodes are not yet activated because of kinematic constraints, and have to be suppressed when using the element.

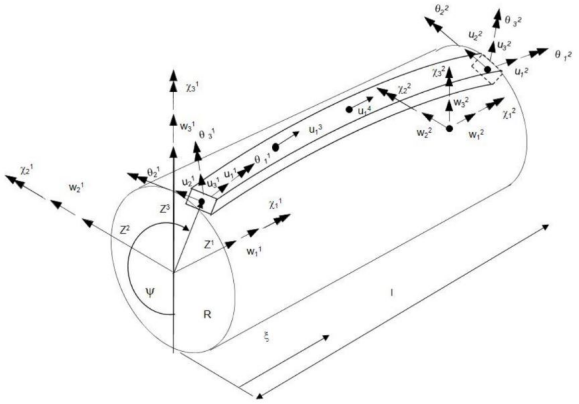

Figure 5.5.1: Degrees of freedom for HSHEAR353 element, Sævik (2013)

The strains can be described as:

$$\epsilon_1 = u_{1,1} - \kappa_3 u_2 + \kappa_2 u_3 \tag{5.36}$$

$$\epsilon_2 = u_{2,1} - \kappa_3 u_1 + \kappa_1 u_3 \tag{5.37}$$

$$\epsilon_3 = u_{3,1} - \kappa_2 u_1 + \kappa_1 u_2 \tag{5.38}$$

The rotations can be expressed as:

$$\omega_1 = \kappa_1 u_{1,1} - \kappa_t u_2, 1 + \kappa_3(u_{3,1} + \kappa_1 u_2) + \kappa_2(u_{2,1} - \kappa_1 u_3 + \omega_{1p}) \tag{5.39}$$

$$\omega_2 = u_{3,11} - \kappa_2 u_1, 1 - 2\kappa_1 u_{2,1} - \kappa_3 \kappa_t u_2 + \kappa_1 \kappa_1 u_3 + \omega_2 \tag{5.40}$$

$$\omega_3 = u_{2,11} - \kappa_3 u_1, 1 - 2\kappa_1 u_{3,1} - \kappa_2 \kappa_t u_2 + \kappa_1 \kappa_1 u_2 + \omega_3 \tag{5.41}$$

Where $u_{i,j}$ is the differentiation of the displacement u_i along the axis X^i with respect to the curve linear coordinate X^j. ϵ_1, ϵ_2 and ϵ_3 are the axial strain, the center line rotation about the X^3 axis and the center line rotation about the X^2 axis respectively. ω_1, ω_2 and ω_3 are the center line torsion, the curvature about the X^3 axis and the curvature about the X^2 axis respectively. The ω_{ip} are the prescribed torsion and curvatures, and the κ_i represents the initial torsion and curvatures. χ_i is prescribed rotation quantities at the pipe centerline and κ_t is given as:

$$\kappa_t = \frac{\cos^2 \alpha}{R} + \sin^2 \alpha \left(\frac{-w_{2,11} \sin \psi}{1 - R w_{2,11} \sin \psi} + \frac{w_{3,11} \cos \psi}{1 + R w_{3,11} \cos \psi}\right. \tag{5.42}$$

HSHEAR363

Helix beam element with 3 nodes; 2 centroid nodes and 1 radial node to describe the radial motion. The centroid nodes have 6 degrees of freedom each and take care of the axial and torsional stiffness, while the radial node has 1 degree of freedom to be able to describe the radial motion and take care of circumferential strain. The nodal points can be described with Cartesian coordinates. It can be interpreted as a simplified shell, and the aim for this element is to describe plastic layers, tape layers, and pressure armor. The degrees of freedom for the HSHEAR363 element are displayed in Figure 5.5.2.

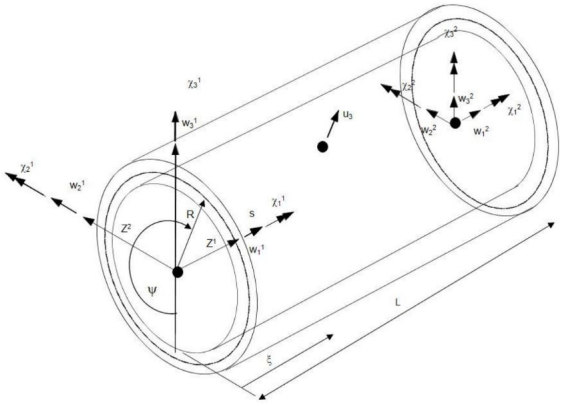

Figure 5.5.2: Degrees of freedom for HSHEAR363 element, Sævik (2013)

The radial displacement can be described as:

$$u_3 = (\gamma_1 + \gamma_2 \cos 2\psi + \gamma_3 \sin 2\psi) \tag{5.43}$$

For pressure armour and tape layers the longitudinal strain can be described as:

$$\epsilon_{11} = cos^2 \alpha w_{1,1} + \frac{\sin^2 \alpha}{R} u_3 + R \sin \alpha \cos \alpha \chi_{1,1} - u_{3,22} \sin^2 \alpha X^3 \tag{5.44}$$

While for the plastic layer the strains can be described as:

$$\epsilon_{11} = w_{1,1} + w_{3,11} R \cos \psi - w_{2,11} R \sin \psi \tag{5.45}$$

$$\epsilon_{22} = \frac{u_3}{R} - u_{3,22} X^3 \tag{5.46}$$

$$\epsilon_{12} = R \chi_{1,1} \tag{5.47}$$

HCONT463

HCONT463 was used to model contact between different layers in a cross-section. Considering two different bodies, A and B where a is inside B. The HCONT463 is made to match the quantities of the HSHEAR353 and the HSHEAR363 elements. For the HSHEAR363 element, the radial displacement is considered only, while for HSHEAR353, the longitudinal and transverse direction are included. Figure 5.5.3 shows the element connecting a HSHEAR353 element and a HSHEAR363

element. The HSHEAR353 side includes 10 DOFs while the HSHEAR363 side includes 3 DOFs resulting in 13 nodes in total. The element is in reality equipped with 15 DOFs where the torsion DOFs are dummies.

When the element is used, it is important to begin in the inner layer of the cross-section. This element begins as the master element and connects its radial node nodes to the two radial nodes of the slave element. Then the slave element becomes the master element and connects its two radial nodes to the radial node of the element on the outside again, until the outer layer is reached.

The energy functional $\Delta\pi$ is can be described as:

$$\Delta\pi = \sum_{l=A}^{B} \Delta\bar{\pi}^l - \int_{S_c} (\lambda_n + \Delta\lambda_n) \cdot g ds - \frac{1}{2\alpha} \int_{S_c} \Delta\lambda_n^2 ds - \int_{S_c} \lambda_t \cdot \Delta\gamma ds - \frac{1}{2} \int_{Sc} \Delta\lambda_t \Delta\gamma ds \quad (5.48)$$

where $\Delta\bar{\pi}^l$ is the incremental potential of the bodies of A and B, λ_t is the shear stress, λ_n is can be found from Equation 5.50, α is a scaling parameter related ot the surface stiffness.

To fulfill equilibrium for the two bodies on the time interva $[t, t + \Delta t]$ it is necessary that:

$$\delta\Delta\pi = 0 \quad (5.49)$$

In addition to the traditional Euler Equations and boundary conditions the following constraint condition is recovered:

$$(\Delta \boldsymbol{u_B} - \Delta \boldsymbol{u_A}) \cdot \boldsymbol{n} + g_0 = \frac{\Delta\lambda_n}{\alpha} \quad (5.50)$$

If $\alpha \to \infty$ the contact condition is recovered exactly.

The contact kinematic of the HCONT463 element is:

$$\Delta u_n = (\Delta \boldsymbol{u_B} - \Delta \boldsymbol{u_A}) \cdot \boldsymbol{n} = (\Delta u_3^{0B} - \Delta u_3^{0A}) \quad (5.51)$$

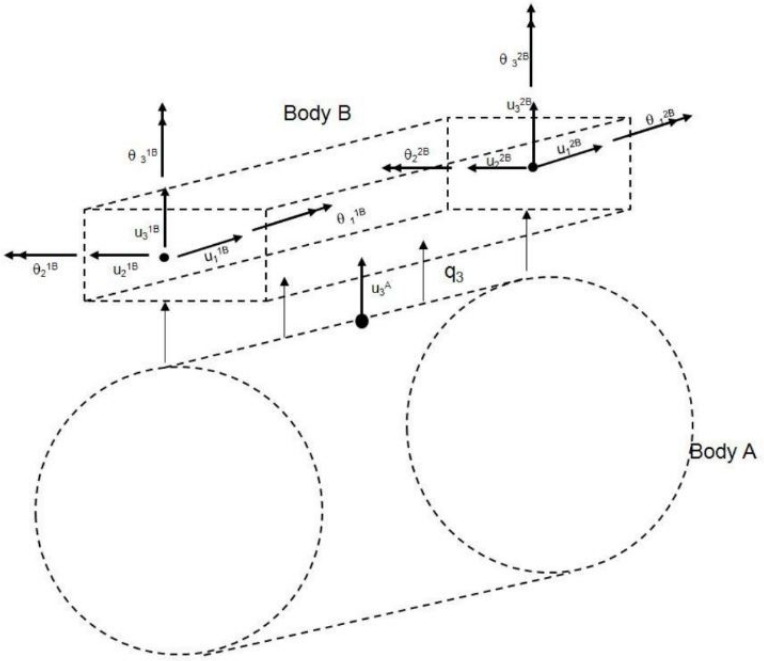

Figure 5.5.3: Degrees of freedom for HCONT463, Sævik (2013)

HCONT454

The purpose of the HCONT454 element is to connect two HSHEAR454 element groups (A and B) in the same layer by considering hoop contact between them and the reduction and expansion of gap due to curvature. Figure 5.5.4 illustrates how the element was used in this study to describe the contact between the conductors in the cross-section.

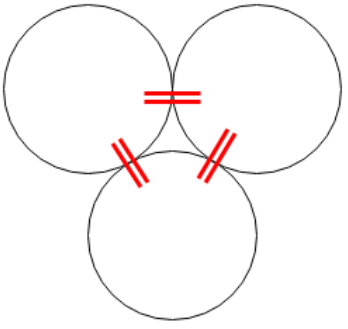

Figure 5.5.4: Illustration of HCONT454 connecting 3 conductors in a cable cross-section

The element has 36 degrees of freedom as can be seen in Figure 5.5.5, where the extra 12 dofs are used to describe the beam strains of the center as this affect the gap in compression and tension. All three directions, X^1, X^2 and X^3 are included where the X^2 direction represents contact, and the others friction. The energy functional described for the HSHEAR463 element in Equations 5.48 to 5.50 are also valid for the HCONT454 element. The contact kinematics in the normal direction can be expressed as:

$$\Delta u_n = (\Delta \boldsymbol{u}_B - \Delta \boldsymbol{u}_A) \cdot \mathbf{n} = (\Delta \boldsymbol{u}_2^{0B} - \Delta \boldsymbol{u}_2^{0A} + \frac{b}{Ff}(\Delta \epsilon_\psi + \Delta \epsilon_{Z^1})) \tag{5.52}$$

where $\Delta\epsilon_\psi$ is the hoop strain:

$$\Delta\epsilon_\psi = \frac{\Delta u_3^{0A} + \Delta u_3^{0B}}{2R} \tag{5.53}$$

and:

$$\Delta\epsilon_{Z^1} = -R\sin\psi\Delta v_{,11} + R\cos\psi\Delta w_{,11} \tag{5.54}$$

Where R is the mean helix radius of the two bodies and $v_{,11}$ and $w_{,11}$ are the center beam transverse curvatures differentiated two times with respect to longitudinal direction.

The only contribution to the incremental relative tangential displacement is from the helix side:

$$\Delta u_s = (\Delta \boldsymbol{u}_B - \Delta \boldsymbol{u}_A)\cdot \mathbf{s} = (\Delta \boldsymbol{u}_1^{0B} - \Delta \boldsymbol{u}_1^{0B}) \tag{5.55}$$

$$\Delta u_t = (\Delta \boldsymbol{u}_B - \Delta \boldsymbol{u}_A)\cdot \mathbf{t} = (\Delta \boldsymbol{u}_3^{0B} - \Delta \boldsymbol{u}_3^{0B}) \tag{5.56}$$

.

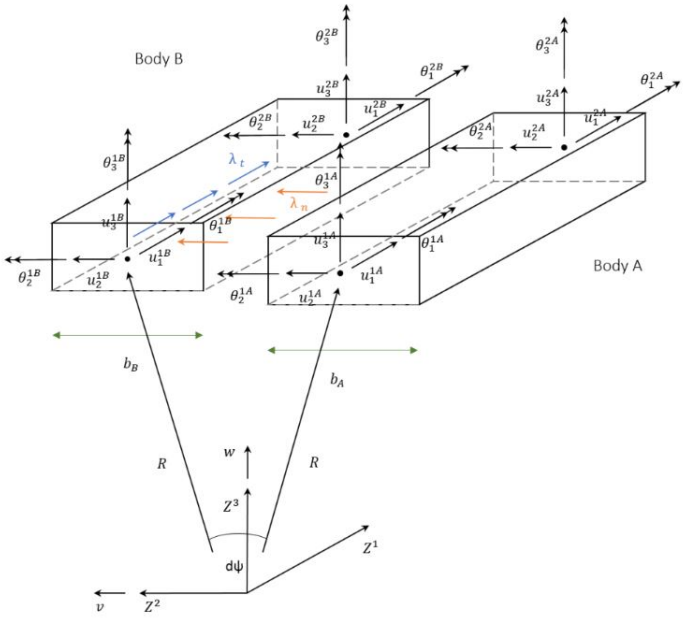

Figure 5.5.5: Degrees of freedom for HCONT454, Sævik (2017)

PIPE52

PIPE52 element is often used to model conic bend stiffeners. It supports a general description of flexible risers and is used to describe "pipe-in-pipe" with a non-linear elastic material curve. It has the same kinematics as PIPE31.

CONT130

A three-node contact element often used to describe contact between a pipe inside a pipe.

Chapter 6

Modeling Methodology

In this chapter, the methodology of the modeling process of the two models is described. The detailed properties of the two models were established in line with Professor Svein Sævik's recommendations

6.1 Procedure for Modelling of Global Model

The global model was created in SIMA RIFLEX, and represented the entire dynamic part of the power cable. The cable hang off was modeled as a point with the motions of the vessel, induced by the transfer functions of OO-Star. With the assumption of most severe fatigue damage at the top of the cable, very little attention was given to the bottom touchdown. The following section describes the modeling procedure of the global model.

6.1.1 Cable Configuration

The global model consisted of 3 sections with 2 different cross-sections, as illustrated in Figure 6.1.1. Section 1 was the lowest part of the cable and was attached to a supernode located on the seabed, with the cable cross-section. The second section was located in the middle of the model with a buoyancy cross-section. The third section was also modeled with the cable cross-section and included the vessel hang off supernode.

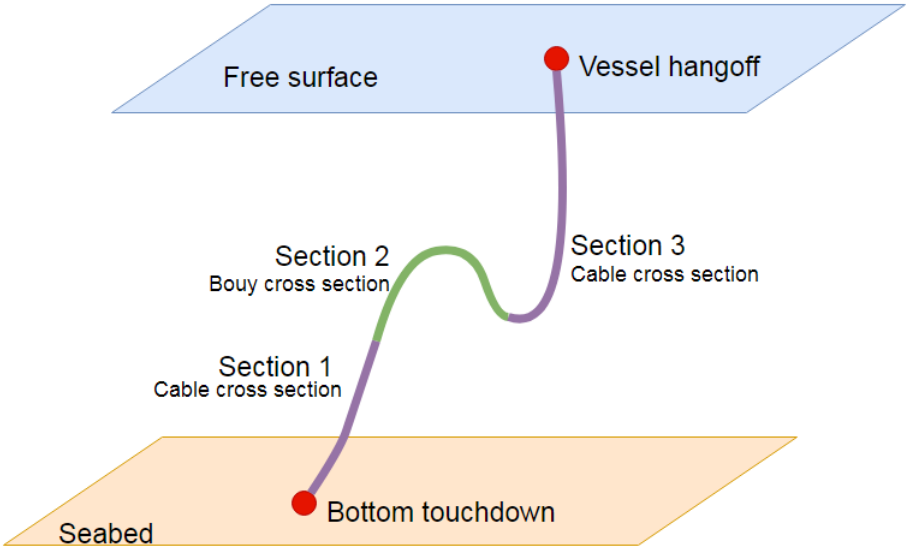

Figure 6.1.1: Illustration of the global model and its different sections

The main purpose of the study was to examine the contact mechanisms in the cable cross-section, rather than perform a full fatigue analysis. Consequently, weather conditions were simplified to include 3 vessel displacements:

- Near: Maximum wind from the east direction
- Neutral: There is no wind
- Far: Maximum wind from the west direction

See Section 4.3.3 for more detailed information on the weather conditions.

Table 6.1 show the vessel positions relative to the anchoring point. The near position was set to be 60 m away from the anchoring. The maximum offset in far position was determined to be 20% of the water depth in the east direction, relative to the neutral position, in line with recommendations from Dr. Techn. Olav Olsen. With the assumption of a linear system, the offset in near position, relative to the neutral position was calculated from the scatter diagram for wind in Figure 4.3.2 as:

$$\text{Offset Near} = \left(\frac{\text{maximum wind speed from east}}{\text{maximum wind speed form west}}\right)^2 \cdot \text{Offset far} \tag{6.1}$$

Position	Distance from anchoring in x-direction [m]
Near	60
Neutral	73.25
Far	96.85

Table 6.1: Floater positions at different wind conditions

The design criteria for the cable configuration were no compression, and a maximum curvature of 1.3675 $\frac{1}{m}$ (American Petroleum Institute (2014)) for the three vessel positions. An iterative approach was used to determine the configuration of the cable, and final measurements are displayed in Table 6.2.

Section number	External area [m^2]	Length [m]
1	0.006171	30
2	0.03	40
3	0.006171	130

Table 6.2: Dimensions of different sections of cable

6.1.2 Cross-sectional Properties

Table 6.3 presents the properties of the two cable cross-sections, and Figure 6.1.1 illustrates their use.

Property	Cable cross-section	Buoy cross-section
Dry mass+ Buoyancy [$\frac{kg}{m}$]	15.75	15.75
External Area [m]	0.006171	0.03
Axial Stiffness [N]	2.0e+08	2.0e+08
Bending Stiffness [Nm^2]	1481	1481
Torsional Stiffness [Nm^2]	5403	5403

Table 6.3: Parameters used for the two different cross-sections

The buoyancy elements used for section 2 of the cable was modelled with an increased external area. The values in Table 6.3 were calculated as follows:

The Dry mass + Buoyancy:

$$\text{Dry mass + Buoyancy} = L_c A_c n_c(\rho_c - \rho_w) + L_{s,1} A_s n_{s,1}(\rho_s - \rho_w) + L_{s,2} A_s n_{s,2}(\rho_s - \rho_w) \quad (6.2)$$

where L_c is the length of a helical copper conductor pr meter, A_c is the area of a copper conductors, n_c is the number of copper conductors, ρ_c is the density of copper, ρ_w is the density of water, $L_{s,i}$ is the length of steel armoring pr meter for layer i, A_s is the area of one wire for the steel armoring, assumed to be the same for layer 1 and 2, $n_{s,i}$ is the number of wires in armoring layer i and ρ_s is the density of steel.

The plastic sheaths and tape were assumed to have the same density as the water, and thus have neutral buoyancy.

The axial stiffness and torsional stiffness were calculated according to Sævik & Ye (2016) as:

$$EA = nEA_t \cos\alpha(\cos^2\alpha - \nu_a \sin^2\alpha) \quad (6.3)$$

$$GI = nA_t ER^2 \sin^2\alpha \cos^2\alpha \quad (6.4)$$

where n is the number of wires in the steel armoring, E is Young's modulus of steel, A_t is the area of one steel wire, G is the Shear moudulus, I is the second moment of inertia, α is the lay angle of

the armoring, and R is the radius in polar coordinates between the armoring layers.

The bending stiffness was calculated from the outer sheath as:

$$EI = E \cdot \frac{\pi}{4}(r_o - r_i) \tag{6.5}$$

where E is Young's modulus of the plastic of the outer sheath, r_o is the outer radius of the outer sheath, and r_i is the inner radius of the outer sheath.

Lead was added to the model to increase its weight and inertia. According to Professor Svein Sævik, the following criteria would be beneficial for the cable:

$$\frac{\sum_{i=1}^{n} m_i - b}{b} \approx 2 \tag{6.6}$$

where m_i is the mass of the different components in the cross-section, and b is the buoyancy.

6 kg/m of lead was added to the model to accommodate the recommendation. It was verified that the incorporation of lead would be feasible if the center tube was made of lead, and by also adding 3 tubes identical to the center tube to the space between the conductors. As the lead did not serve any structural purpose, it was included in the model by an increase of the Dry mass + buoyancy, reaching 15.75 $\frac{kg}{m}$ as shown in Table 6.3.

An additional dummy supernode was added to the vessel with a dummy line between the two supernodes attached to the vessel. The dummy supernode enabled calculation of the angle between the vessel and cable by dot product.

6.1.3 Boundary Conditions

The cable touchdown was fixed in all translational and rotational degrees of freedoms. The cable hang-off on the vessel was fixed in all translational degrees of freedom and free in all rotational degrees of freedom.

6.1.4 Testing of Global Model

Prior to the analyses, the global model was verified by exposing the model to the most severe sea state and evaluating its fundamental properties. The following results for each of the three weather conditions were seen as vital to assess the quality of the model:

- The static configuration without current, to make sure the cable possessed the desired lazy wave shape, and that the buoyancy section was not too high in the water.
- Curvature envelope, to make sure the curvature did not exceed the maximum curvature of 1.3675 $\frac{1}{m}$.
- Maximum force envelope, to make sure the maximum tension in the cable was tolerable.
- Minimum force envelope, ensure no compression in the cable.

Table 6.4 display the verification test setup for the global model.

Variable	Value
Hs [m]	13.5
Tp[s]	16
Time step [s]	0.1

Table 6.4: Key variables used in testing of global model

The results from the verification test showed no compression in the cable and acceptable curvature. The maximum capacity of the cable was calculated by Equation 6.7 to be 223kN, while the maximum tension in the cable during static analysis was 40.69kN, well within the tension capacity. The results of the verification indicated that the global model performed satisfactorily. All the results were plotted and can be reviewed further in Appendix A.

$$T_{cap} = n\cos(\alpha)\sigma_y A_s \tag{6.7}$$

where n is the total number of armouring layers in both layers, α is the lay angle, σ_y is the yield stress of steel and A_s is the area of one steel fibre.

Figure 6.1.2 and Figure 6.1.3 show the global model in its three possible configurations, with and without current.

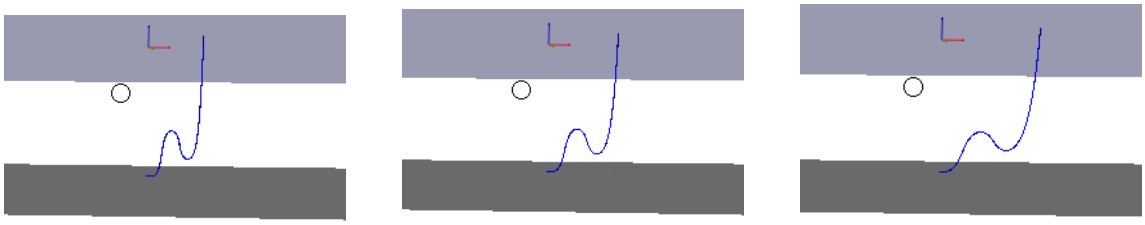

(a) Near position (b) Neutral position (c) Far position

Figure 6.1.2: Static configuration of the global model for different vessel displacements, without current

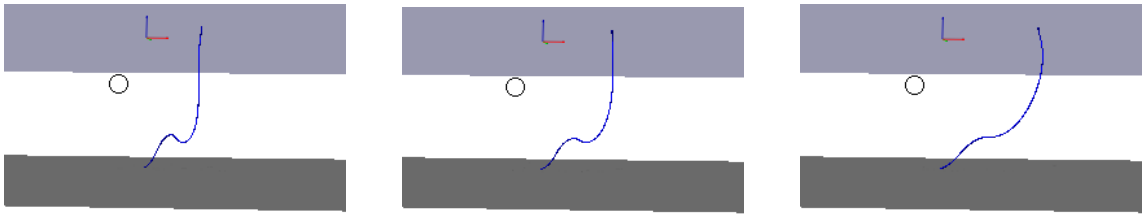

(a) Near position (b) Neutral position (c) Far position

Figure 6.1.3: Static configuration of the global model for different vessel displacements, with current

6.2 Procedure for Modelling of Local Model

The local model was created in Bflex and only consisted of the upper part of the cable, in line with the assumption of the location of most severe fatigue damage. The model was developed from the inner layer and outwards, with three main components, as illustrated in Figure 6.2.1. The extra lead added to the cross-section was not included due to the lack of structural importance.

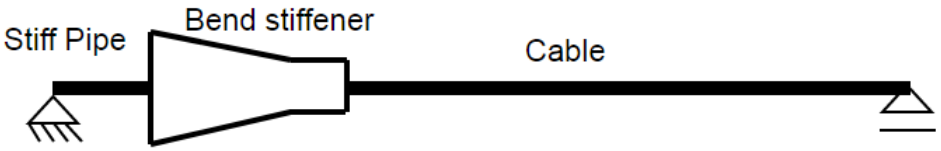

Figure 6.2.1: Illustration of local model

6.2.1 Cable

Figure 6.2.2 illustrated the cable cross-section.

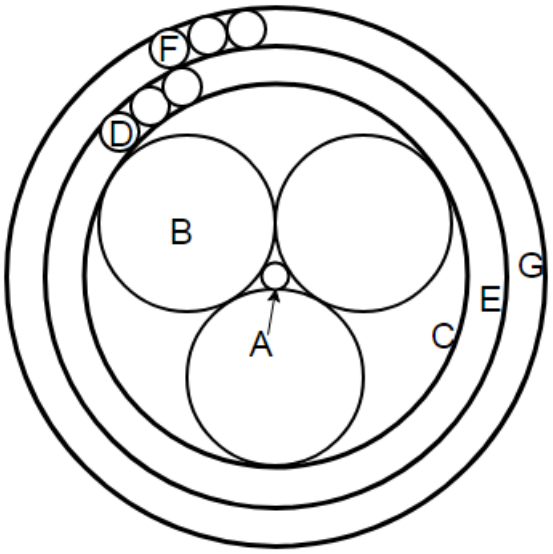

Figure 6.2.2: Illustration of cable cross-section in local model

Initially, the cable model had a length of 5 pitch lengths, but this was later changed to 4.25 as it became apparent that the model was too short. The cable included several layers and components, as displayed in Figure 6.2.2. The straight components were modeled with HSHEAR363 elements. That includes the center tube (A), the sheath around the conductors (C), the tape between the armoring layers (E), and the outer sheath(G). The helical components were modeled with HS-HEAR353 elements and included the conductors (B) and the armoring layers (D) and (F). The cable was formed out of one central node system, and all the components were connected to this node system in addition to possessing their respective radial node system.

Contact elements were used to model the interaction between the element groups. HCONT463 was used to describe the contact between different layers. The interaction between the layers was described by making one layer the master and the other the slave, and connecting their center nodes and radial nodes. Figure 6.2.3 illustrates how HCONT463 connected the different layers.

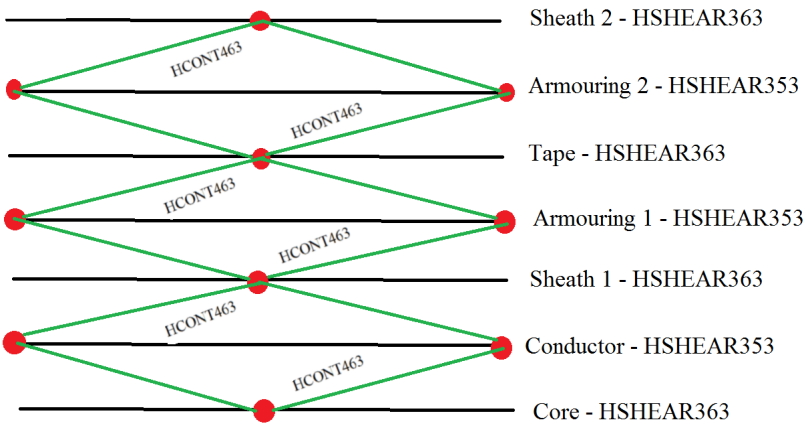

Figure 6.2.3: Logic of HCONT463

HCONT454 was used to describe the contact between the conductors. This element connects the two radial nodes of the HSHEAR353 elements together.

The conductors were modeled with a lay angle of 8 degrees, and the armouring with a lay angle of 20 degrees.

The cable included three different materials. The conductors were of copper, the armouring were of steel and the sheaths and tape were made of plastic. The most important material properties are reproduced in Table 6.5

Property	Steel	Copper	Plastic
Type	Linear	Linear	Elastic
Young's Modulus [GPA]	210	115	0.7
Shear Modulus [GPA]	80	40	
Poisson's Number [-]	0.30	0.36	0.35
Axial stiffness [N]	1.48e+06	1.07e+07	
Bending stiffness [Nm^2]	0.835	4.19	
Torsional stiffness [Nm^2]	0.64	0.32	

Table 6.5: Properties of the materials used in the local model

The friction between layers was determined by the use of FRICONTACT materials. Table 6.6 presents the properties of the contact materials and Table 6.7 displays their usage.

Property	contact01	contact1	contact10
Type	Coulomb friction	Coulomb friction	Coulomb friction
Static friction coeff. [-]	0.15	0.15	0.15
Dynamic friction coeff. [-]	0.15	0.15	0.15
Elastic stiffness in axial direction $[N/m^2]$	100e6	100e6	100e6
Elastic stiffness in transv. direction $[N/m^2]$	100e6	100e6	100e6
Surface stiffness [N/m^2]	100e5	100e6	100e8

Table 6.6: Properties of the friction elements used in the local model

Contact	Friction Model
center tube - Conductor	contact01
Conductor - Conductor	contact1
Conductor - Sheath	contact1
Sheath 1 - Armouring 1	contact1
Armouring 1 - Tape	contact10
Tape - Armouring 2	contact10
Armouring 2 - Sheath 2	contact1

Table 6.7: Friction models for different contacts in cable

6.2.2 Bend Stiffener

A bend stiffener was added to the model to ease the transition between the cable and the cable hang off.

The dimensions of the bend stiffener were roughly calculated early in the process with the following procedure:

Locking radius of the flexible cable:

$$LR = \frac{r}{1 - F_j} = \frac{r}{1 - 0.9} = 10r \tag{6.8}$$

where LR is the locking radius, r is the radius of the conductor, F_j is the fillfactor = 0.9 was used.

Minimum bend radius from American Petroleum Institute (2014):

$$r_{min} = 1.5 * 1.1 * LR \tag{6.9}$$

where r_{min} is the minimum locking radius, and LR is the locking radius.

Maximum curvature:

$$\kappa_{max} = \frac{1}{r_{min}} \tag{6.10}$$

where κ_{max} is the maximum curvature, and r_{min} is the minimum locking radius.

Angle between cable and vessel:

$$\theta_{tot} = \theta_s + \theta_p + \theta_{offset} \tag{6.11}$$

where θ_{tot} is the total angle at the end of the flexible cable, θ_s is angle due to surge, θ_p is angle due to pitch and θ_{offset} is the angle due to the offset of the floater. These variables are calculated as follows:

Angle due to surge:

$$\theta_s = \arctan\left(\frac{\mu_{surge}}{L_1}\right) \tag{6.12}$$

$$\mu_{surge} = \frac{H_{max}}{2} RAO \tag{6.13}$$

where L1 is the assumed length from the vessel to the curve on the lazy wave configuration due to the buoyancy elements. H_{max} is the significant wave height for the most extreme sea state in the scatter diagram in Figure 4.3.4 and RAO is the response amplitude operator for surge provided by Dr. Techn. Olav Olsen.

Angle due to pitch:

$$\theta_{pitch} = \frac{H_{max}}{2} RAO \tag{6.14}$$

where H_{max} is the significant wave height for the most extreme sea state in the scatter diagram in Figure 4.3.4 and RAO is the response amplitude operator for pitch provided by Dr. Techn. Olav Olsen.

Angle due offset:

$$\theta_{offset} = \arctan\left(\frac{offset * depth}{L_1}\right) \tag{6.15}$$

This can be used to calculate the length of the bend stiffener:

$$L_{BS} = \frac{\theta_{max}}{\kappa_{max}} \tag{6.16}$$

where L_{BS} is the length of the bend stiffener, θ_{max} is the maximum angle and κ_{max} is the maximum curvature.

Further, the outer diameter for the widest part of the bend stiffener can be calculated as follows:

maximum tension is estimated to

$$T = 1.3 T_{static} \tag{6.17}$$

where T is the maximum tension, and T_{static} is the static tension due to the configuration of the riser.

$$T_{static} = 10 + W_s + L_1 \tag{6.18}$$

where W_s is the submerged weight of the cable and L_1 is the depth from the floater to the curve on the lazy wave configuration due to the buoyancy elements.

W_s was calculated for all the components pr meter cable the following way:

$$W_s = \sum V(\rho_{comp} - \rho_{water}) \tag{6.19}$$

Where V is the volume for each component, ρ_{comp} is the density of the material of the component and ρ_{water} is the density of the water.

Number of armouring fibres that fit around the cross-section, the following method was used:

$$F_j = \frac{nD}{\cos(\alpha)2\pi R} \tag{6.20}$$

where F_j is the fill factor, n is the number of armoring fibers with diameter D that can fit around a larger circle with radius R, and α is the lay angle of the armoring fibers.

The bending stiffness EI was calculated by the following expression:

$$\kappa_{max} = \sqrt{\frac{T_{max}}{EI}}\theta_{max} \tag{6.21}$$

where κ_{max} is the maximum curvature, T_{max} is the maximum tension, EI is the bending stiffness, and θ_{max} is the maximum angle.

Finally, the outer radius of the bend stiffener was calculated by:

$$EI = \frac{\pi}{4}(r_o^4 - r_i^4) \tag{6.22}$$

where EI is the bending stiffness, r_o is the outer radius of the bend stiffener and r_i is the inner radius.

The bend stiffener from the rough calculations proved inadequate, and the final diemensions, showed in Table 6.8, were determined through an iterative process. The bend stiffener was positioned one pitchlengt from the cable termination.

Parameter	Value [m]
Length	1.400
Outer diameter, widest part	0.260
Outer diameter, narrowest part	0.100
Inner diameter	0.097

Table 6.8: Dimensions of bend stiffener

Material Data for Bend Stiffener

The material of the bend stiffener was polyurethane with non-linear material properties. The initial Young's modulus was chosen to be 150 GPa, with decay in stiffness according to Figure 6.2.4.

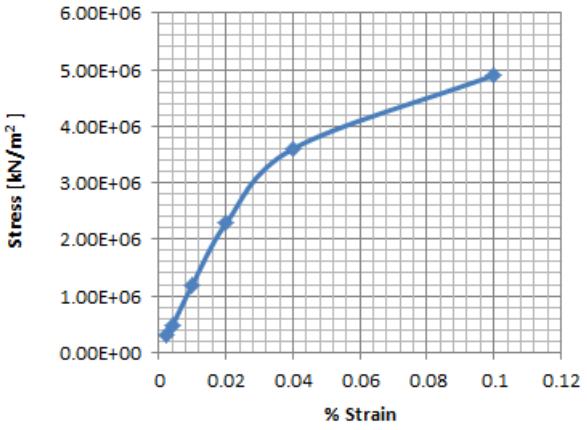

Figure 6.2.4: Stress-strain relationship for bend stiffener material

6.2.3 Stiff Pipe

A stiff pipe was modeled at the end of the cable to avoid curvature and transient effects at the cable termination. The pipe had the length of one pitch length and was modeled with PIPE31 elements. The first node of the stiff pipe was connected to the first node of the central node system through the CONSTR card in Bflex. The card assigns one node to be the slave and the other to be master, and defines the relationship between them according to Equation 6.23. With $C_1 = 1$, the nodes followed each other exactly.

$$r_{Si} = C_1 \cdot r_{Mj} \tag{6.23}$$

Where r_{Si} is the displacement of the slave node, C_1 is a constant describing the relationship between the master and the slave and r_{Mj} is the displacement of a master node.

6.2.4 Method for Application of Tension

For an easy application of dynamic tension to the model, an extra pipe element was added at the end of the model as can be seen in red in Figure 6.2.5. The element had a very low EA, but the same EI as the steel armoring, enabling tension to be applied as strain so that:

$$\epsilon_0 = T_0 \tag{6.24}$$

where ϵ_0 is the reference value for strain and T_0 is the reference value for tension. This was scaled so that the reference value was T_0 =1kN, and desired tension could easily be applied in Bflex by multiplying the strain with a factor.

Figure 6.2.5: Illustration of the extra element added for easy application of tension

6.2.5 Boundary Conditions

The boundary conditions of the local model allowed the cable to slide inside the bend stiffener. The following constraints were implemented:

- Centroid system was fixed in 2 and 6 for all nodes, and 2 and 3 for the last nodes
- Radial nodes of the center tube, sheaths, and tape were fixed in 2 and 3 for all nodes.
- The conductors were fixed in 1 and 2 for the first and last node. Degree of freedom 4 was fixed in all nodes.
- The armoring layers were fixed in 1 at the first node, and in 2,4,5 and 6 for all nodes

6.2.6 Testing of Local Model

Like the global model, the local model was verified prior to the analyses. The following sequence of loads was added to the local model:

1. Gravity Load: Gravity was excluded in the local model, but the effect of the mass of the model was applied at the first time step.
2. Tension: The mean tension was applied to the local model at t=1s to t=5s, in the axial direction on the last node in the outer sheath, with a magnitude 13.7kN found from the global analysis.
3. Initial strain: Initial strain of magnitude 0.03 was added to the outer sheath of the model in 1 direction at t=1s to t=5s.
4. Bending: Smooth bending of the cable was applied with a dynamic angle. The cable was bent from 0 degrees to 5 degrees between t=5s and t=15s, and from 5 degrees to -5 degrees between t=15s and t=35s.

The following results were seen as relevant for the evaluation of the local model:

- Force in the conductors over the length of the cable
- Moments about X, Y and Z axis over the length of the cable
- Curvature of the outer sheath over the length of the cable
- Curvature in bend stiffener

The testing revealed that the local model seemed acceptable. All the results of the testing of the local model are in Appendix B. Figure B.1.1 shows that the tension variation on the conductors between maximum angle and minimum angle died out towards the end of the model, indicating that the model was of sufficient length, and the same can be seen for the moments in Figure B.1.2 to Figure B.1.5. The curvature was about zero at the beginning and end of the outer sheath (Figure B.1.6), and the curvature in the bend stiffener (Figure B.2.1) had the desired shape. The results indicated that the bend stiffener had appropriate dimensions and was serving its purpose.

Figure 6.2.6 and Figure 6.2.7 show the local model and some of its components as they appeared in XPOST.

(a) Local model from the side with bend stiffener

(b) Cable cross-section in local model

Figure 6.2.6: Local model

(a) Conductors

(b) Armouring

Figure 6.2.7: Helical components of the local model

Chapter 7

Analyses Methodology

In this section, an overview of the procedure to calculate the fatigue life is presented. Figure 7.0.1 illustrates the analysis algorithm.

Figure 7.0.1: Algorithm for calculation of fatigue life

7.1 Global Analysis

The global analyses were performed by exposing the global model in far configuration to all 160 sea states in Figure 4.3.4 with one-hour record length. The following three resulting quantities from the analyses were stored in separate files for each time step and each sea state:

- The tension in the upper element of the cable.
- The displacement of the dummy node on the vessel in x-, y-, and z-direction.
- The displacement of the supernode at the cable hang off, and subsequent node in the top the cable in x-, y- and z-direction.

7.1.1 Post Processing of Global Analyses Results

The angle (θ) between the vessel and cable in Figure 7.1.1 was calculated and turned into time series by dot product as in Equation 7.1. Figure 7.1.2 presents examples of the time series of the angle between the vessel and cable, and the tension in the upper element obtained from the global analyses.

$$cos(\theta) = \frac{\boldsymbol{a} \cdot \boldsymbol{b}}{|\boldsymbol{a}||\boldsymbol{b}|} \tag{7.1}$$

Where $\boldsymbol{a}$ and $\boldsymbol{b}$ are the vectors of the dummy element and the first element of the cable.

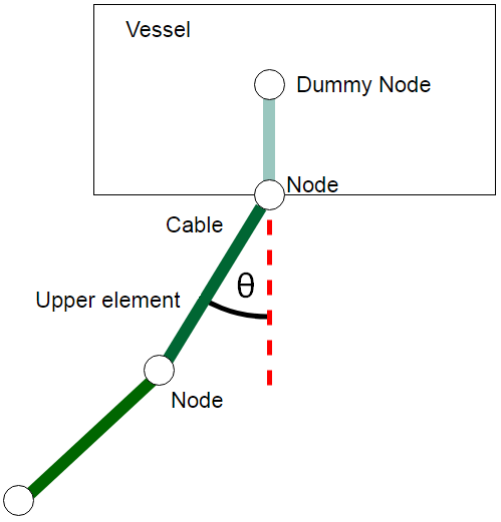

Figure 7.1.1: Angle between vessel and cable

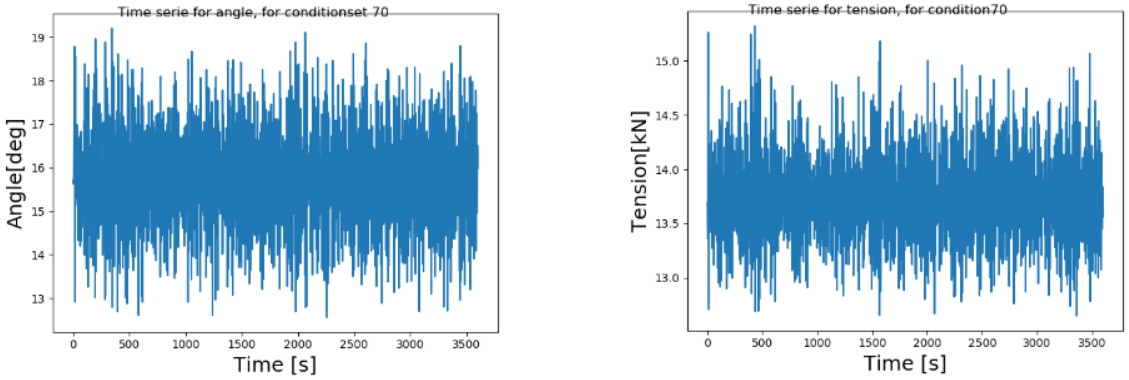

(a) Time series for angle between vessel and cable

(b) Time series for tension in the upper element

Figure 7.1.2: Example of time series for angle and tension

7.2 Rainflow Counting

Rainflow Counting was performed in Python on the time series of the angle to determine the number of cycles for each angle range. The Rainflow Counting algorithm used by Python is explained in Section 3.4.3. The counts from each sea state were scaled for their occurrence in the scatter diagram in Figure 4.3.4 to apply for one year according to:

$$n_{cycle,year} = n_{cycle,hour} \frac{n_{seastate}}{N_{seastate}} \cdot 365 \cdot 24 \tag{7.2}$$

Where $n_{cycle,year}$ is the number of cycles of in an angle class in a whole year, $n_{cycle,hour}$ is the number of cycles in an angle class for an hour, calculated by the global analyses, $n_{seastate}$ is the

number of observations of an individual sea state according to the scatter diagram, and $N_{seastate}$ is the total number of sea states in the scatter diagram in Figure 4.3.4.

The results from the Rainflow Counting can be seen in Figure 7.2.1. The angle range classes were of equal length of 0.3, but it is not possible to see the classes on the x-axis due to a large number of classes.

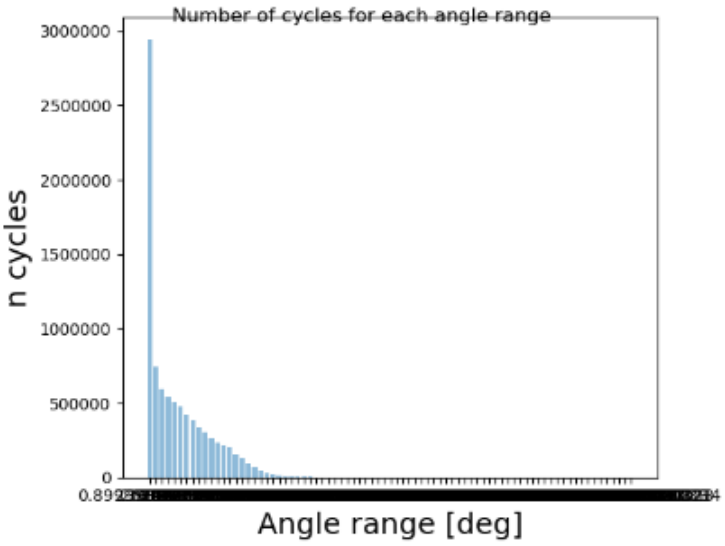

Figure 7.2.1: Distribution of cycles for each angle class

It is apparent from Figure 7.2.1 that the majority of the cycles occurred in the first angle range classes, and decreasing as the angle range increases.

The damage from each range was calculated according to Miner-Palmgren summation concept in Equation 3.13, with N_i calculated from the SN-Curve from Equation 3.11. The damage inflicted by each angle range class was calculated as:

$$d_i = \frac{n_i}{N_i} \tag{7.3}$$

$$d_i = \frac{n_i}{\frac{c}{\Delta\sigma^m}} \tag{7.4}$$

Where d_i is the damage from the cycles in angel class i, n_i is the number of cycles in angle class i, N_i is the number of cycles until failure for angle class i, c and m are from Equation 3.11, c=4 and m=2.88e25 for this case, $\Delta\sigma$ is the stress range that relates to the angle range as: $\Delta\sigma_i = a\Delta\theta_i$ where a is an arbitrary constant.

Figure 7.2.2 demonstrates the damage from each angle range class. The middle classes evidently cause the most substantial damage, combining a high number of cycles with high damage per cycle.

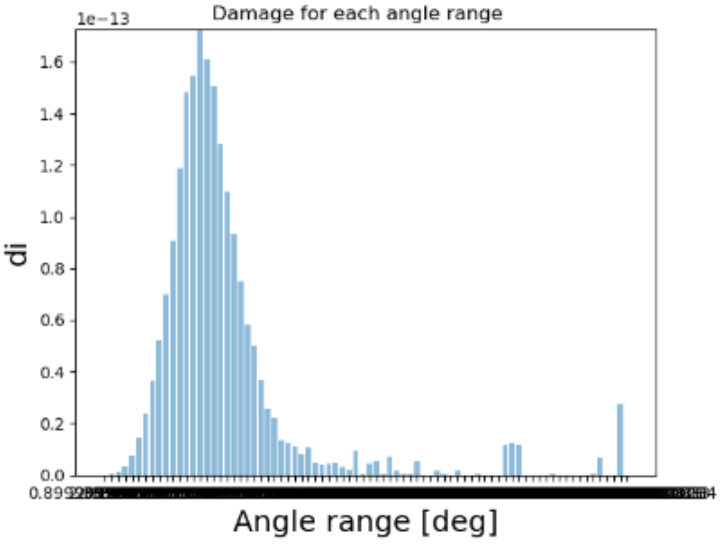

Figure 7.2.2: Damage for each angle class

To obtain a high resolution of the final results, the angle range classes were rearranged and merged into 15 classes with approximately the same damage impact. Figure 7.2.3 shows the damage caused by the 15 rearranged angle range classes, and Figure 7.2.4 and Table 7.1 present the rearranged cycle distribution.

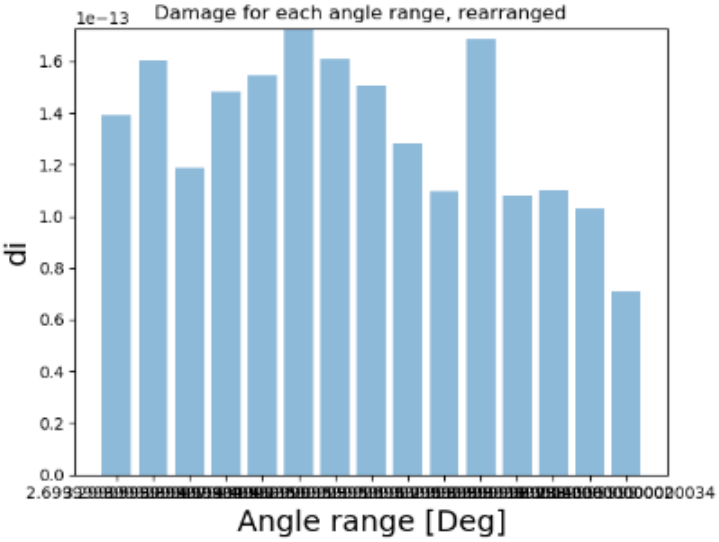

Figure 7.2.3: Damage for each angle class, rearranged

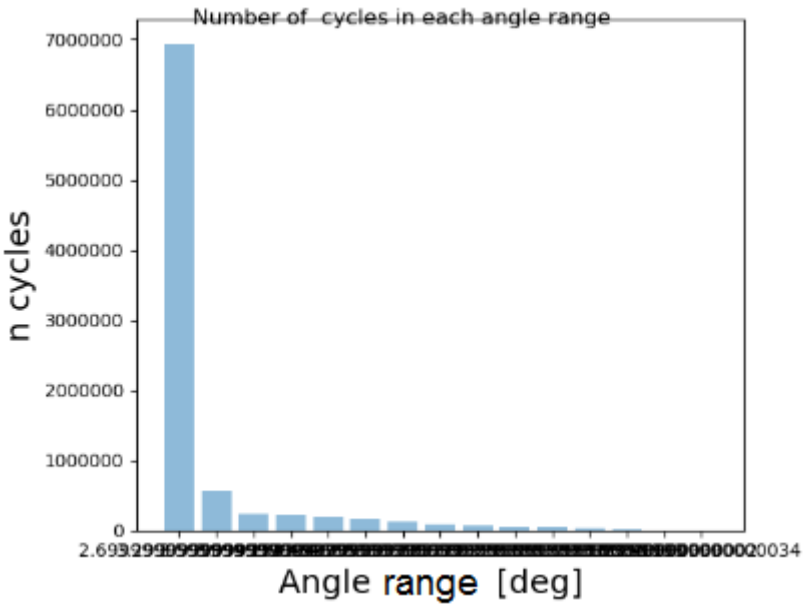

Figure 7.2.4: Distribution of cycles for each angle class, rearranged for equal damage

Angle range class [deg]	Number of cycles
0.0 - 2.7	6930399.8
2.8 - 3.3	571967.9
3.4 - 3.6	237278.5
3.7 - 3.9	219492.0
4.0 - 4.2	198970.4
4.3 - 4.5	154052.1
4.6 - 4.8	130555.0
4.9 - 5.1	93955.7
5.2 - 5.4	68946.3
5.5 - 5.7	46839.2
5.8 - 6.3	54651.8
6.4 - 6.9	24288.7
7.0 - 8.4	16385.8
8.5 - 18.0	3355.4
18.1 - 23.4	139.3

Table 7.1: Number of cycles in each angle range class

It is important to note that the cycle counts in Table 7.1 are not just half and whole cycles, as they were already scaled for occurrence in one year.

7.3 Local Analysis

The results from the global analyses served as input for the local analyses. Due to the nature of the boundary conditions of the local model, both ends of the model experienced rotation when a dynamic angle was applied. This is shown in Figures 7.3.1 and 7.3.2, where θ_1 was equal to the applied angle, but the total angle experienced by the model was:

$$\theta_{tot} = \theta_1 + \theta_2 \tag{7.5}$$

Where θ_{tot} is the total angle experienced by the local model and θ_1 and θ_2 are illustrated in Figure 7.3.1.

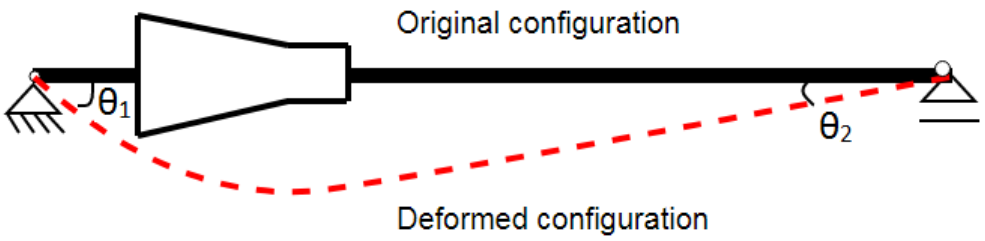

Figure 7.3.1: Illustration of initial and deformed configuration of local model

Figure 7.3.2: Deformed local model in XPOST

Several analyses were done to establish the relation between the applied angle and the total angle. Figure 7.3.3 show the linear regression with a coefficient of determination (R^2) of 0.9978, and the relationship:

$$\theta_{tot} = 1.2694\theta_{appl.} \tag{7.6}$$

Where θ_{tot} is the total angle experienced by the local model and $\theta_{appl.}$ is the angle applied by Bflex.

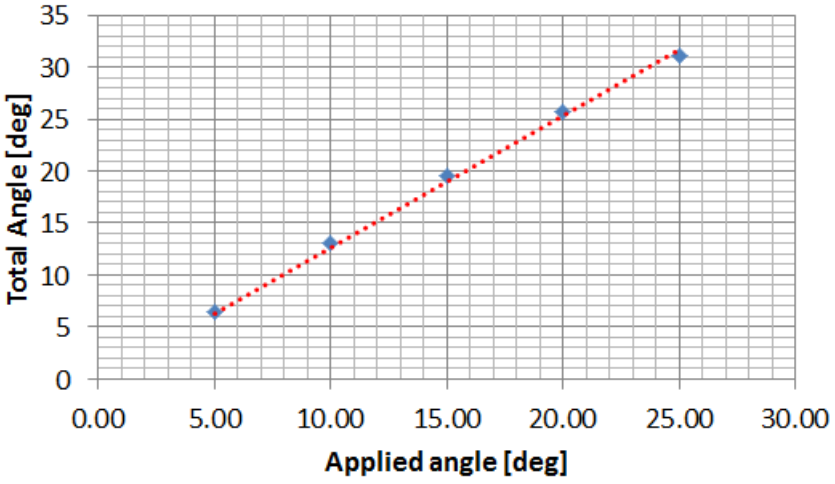

Figure 7.3.3: Relationship between applied angle and total angle

To determine the input for the local analysis, it was decided in line with Professor Svein Sævik's recommendations that the angle would be the master over the tension. Although the trends in the angle time series and the tension time series agreed, the high angles and tensions did not occur at the exact same time steps, resulting in no linear correlation. A simple but conservative approach, with the assumption that maximum tension occurred with maximum angle, and minimum tension occurred with minimum angle, was adopted. The maximum and minimum tension recorded at the top of the cable was 40.69 kN and 9.32 kN, respectively, and linear interpolation was used to calculate the dynamic tension levels corresponding to the dynamic angle ranges in Table 7.1.

Bend stiffeners are usually mounted in a stress-free configuration, equivalent to the neutral vessel position in this study. The stress-free configuration angle was -2.32° found from the SIMA RIFLEX, with zero degrees being as if the cable was hanging straight down and positive angle is counterclockwise. The dynamic analyses were performed in the far position with current, where the static position of the bend stiffener was 15.78° due to the strong current as can be seen in Figure 6.1.3. The total mean angle was, consequently, 18.16°, and the maximum and minimum angle for each angle range were added and subtracted to the mean angle, so that the cable oscillated about this angle.

Table 7.2 display the 15 load cases for the local analysis. The angles displayed in the table are the corrected angles, calculated by Equation 7.6. The dynamic tensions were found through interpolation, and the mean tension represents the static tension at the top of the cable after the current was applied in far position. The analyses were administered by a Cygwin script, making it easy to change the variables in each case.

Load case Nr.	Max. Angle [deg]	Min. angle [deg]	Mean tens.[kN]	Max. tens.[kN]	Min. tens.[kN]
1	16.43	12.18	13.7	25.07	11.50
2	16.91	11.71	13.7	25.52	11.44
3	17.14	11.47	13.7	25.75	11.41
4	17.38	11.23	13.7	25.97	11.37
5	17.61	11.00	13.7	26.20	11.34
6	17.85	10.76	13.7	26.42	11.31
7	18.09	10.52	13.7	26.65	11.28
8	18.32	10.29	13.7	26.88	11.25
9	18.56	10.05	13.7	27.10	11.22
10	18.80	9.82	13.7	27.33	11.18
11	19.27	9.34	13.7	27.78	11.12
12	19.74	8.87	13.7	28.24	11.06
13	20.92	7.69	13.7	29.37	10.90
14	28.49	0.13	13.7	36.62	9.89
15	32.74	-4.13	13.7	40.69	9.32

Table 7.2: Parameters for load cases in the local analyses

7.4 Calculation of Fatigue Life

The fatigue life was calculated for each layer at two points of the conductors:

- At maximum curvature range (x=0.900m)
- At maximum tension range (x=0.625m)

The two points did not coincide due to a phase shift caused by friction. The calculation methodology was the same for both points.

Tension and curvature plots served as outputs from the local analyses, and can be viewed in whole in Appendix C. The output was used to calculate the stress range on for each layer in each case according to the analytical model described in Section 3.4.6. Lay angles were $\alpha_2 = -4.1°$ and $\alpha_3 = +7.3°$ for the innermost layer and outer layer respectively, Nasution et al. (2013). The friction coefficient was $\mu = 0.2$, and the stress concentration factor (SCF) for the innermost layer and the outer layer were 1.058 and 1.238 respectively, Nasution et al. (2012).

The number of cycles until failure (N_i) was calculated from Equation 3.11. Damage from each case in one year was calculated according to the Miner-Palmgren summation concept from Equation 3.13, using the cycle counts (n_i) found by Rainflow Counting in Table 7.1. By inverting the damage generated in one year, the fatigue life in years was calculated with a DFF=10.0. The results were mean stress corrected according to the Söderberg assumption described in Section 3.4.5.

7.5 Sensitivity Studies and Study of Friction Mechanisms

Several additional studies were performed to obtain insights into the contact mechanisms in the cable cross-section. By further examination of the results collected from the global and local analyses, the following aspects were investigated:

- Study of sensitivity by using mean and minimum tension in Equation 3.26
- Study of sensitivity to the choice of SN-Curve
- Study of the effect of contact between conductors on fatigue life
- Study of the effect of contact between layers in conductors on fatigue life

All studies above were performed at the point on the conductor with maximum tension range.

7.5.1 Study of Sensitivity of using Mean and Minimum Tension in Equation 3.26

Equation 3.26 in the analytical model does not contain specifications on which tension (T) to be used, but maximum tension yields the most conservative approach. As a sensitivity study, the fatigue life was also calculated using the mean and minimum tension in Equation 3.26 to see what effect this would have on the fatigue life.

7.5.2 Study of Sensitivity to Choice of SN-Curve

The results were compared to the findings by Karlsen (2010), to investigate their sensitivity to the choice of SN-Curves. The fatigue life was calculated from the two proposed SN-Curves in the paper and applying a safety factor of 10.0. The SN-Curves were derived found from experimental tests of Nexans conductors, but did not account for the SCF. Consequently, the SCFs were excluded from Equation 3.20 in the analytical model for the calculation. Figure 7.5.1 shows the SN-Curves from Karlsen (2010). The parameters in the SN-Curve expressions, with two standard deviations subtracted, are presented in Table 7.3.

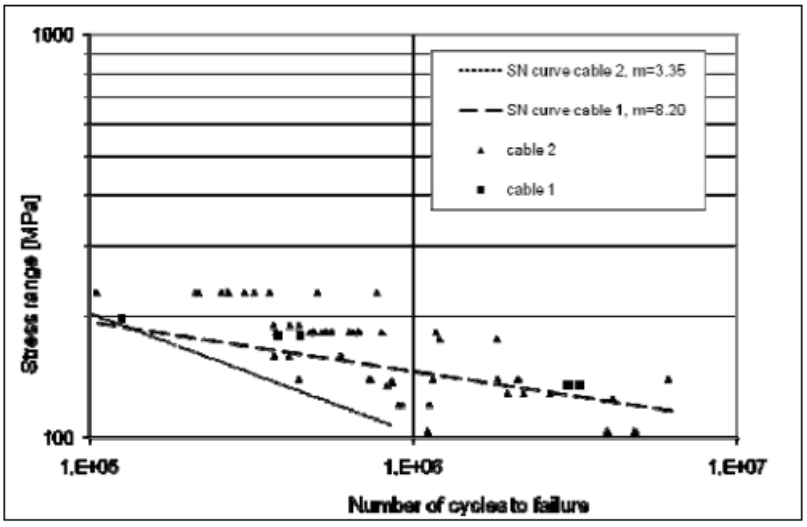

Figure 7.5.1: SN-Curves from Karlsen (2010)

	c	m
SN-Curve cable 1	1.855E25	8.20
SN-Curve cable 2	1.282E14	3.35

Table 7.3: Parameters for SN-Curves with two standards deviations subtracted, Karlsen (2010)

7.5.3 Study of Effect of Contact Between Conductors

The HCONT454 element described the contact between the three helical conductors in the cable cross-section. Including the effect of contact mechanism between the conductors was investigated by looking at the plot of tension at the maximum and minimum angle in each case. Figure 7.5.2 show the contribution to the tension range from the contact between the conductors. It was represented as the difference between the maximum tension range(ΔT_{max}) illustrated by the green arrow, and the tension range from applied tension (ΔT_T) at the end of the model, illustrated by the yellow arrow.

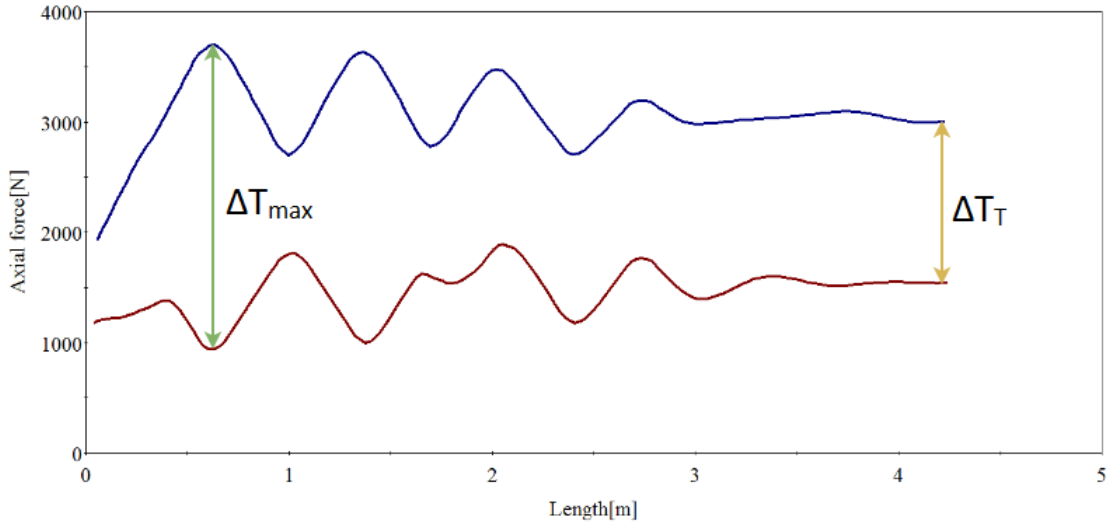

Figure 7.5.2: Effect of contact between conductors

The contribution to the tension range from the contact friction could be calculated as:

$$\Delta T_f = \Delta T_{max} - \Delta T_T \tag{7.7}$$

Where T_f is the contribution to the tension range form contact between the conductors, ΔT_{max} is the maximum tension range and ΔT_T is the tension range from applied tension to the local model.

The fatigue life was calculated again with the analytical model in Section 3.4.6 with ΔT_T for the tension range in Equation 3.21.

7.5.4 Study of Effect of Contact Between Layers in Conductors

The friction between the layers in the conductor was included in the analytical model by the friction term, $\Delta\sigma_f^i$ in Equation 3.20. By eliminating this term, contact between the layers in the conductor was excluded, and Equation 3.20 for the stress range was reduced to:

$$\Delta\sigma = \Delta\sigma_T \cdot SCF + \Delta\sigma_{nc} \tag{7.8}$$

Calculation of fatigue life was furthermore completed according to the analytical model in Section 3.4.6.

Chapter 8

Results and Discussion

In this chapter, several aspects of the master thesis are discussed, including the chosen case study and the methodologies for the global and local models and analyses. Furthermore, the results are presented and discussed.

8.1 Discussion of Case Study

8.1.1 Floating Wind Turbine

The OO-Star from Dr. Techn. Olav Olsen, and Lifes50+was chosen as the basis for the case study, due to the author's prior familiarity with the project from a summer internship. The Lifes50+ report is comprehensive, and OO-Star proved to be an appropriate support structure for the study. Another option could have been to use the Hywind concept that is already installed at the Hywind Scotland Project, or one of the other concepts in the Lifes50+ project.

8.1.2 Location and Environmental Conditions

West of Barra was chosen as the location for the study, due to its deep water and challenging weather conditions. However, as the work was carried out, the wave conditions proved to be slightly too challenging, as some wave periods coincided with severe resonance in the transfer functions of OO-Star. The most extreme sea state observations were moved to lower Tps in the scatter diagram while maintaining the total number of observations. The relevant extreme sea states had low occurrence, and consequently, a small impact on the total fatigue life. In retrospect, other less extreme locations could have been considered.

8.1.3 Cable

The cable cross-section was based on guidance from Professor Svein Sævik, who has extensive experience in the field. Another approach could have been to contact a subsea cable manufacturer and adopt one of their designs. However, the majority of dynamic power cables are designed specifically for their use, and standardized models are rare. The cable proved to be slightly too lightweight and exhibited a large response to the vessel motions. 6 $\frac{kg}{m}$ of lead was added to the cross-section to increase the cable inertia, but double armoring could have been included in the cross-section. The price of steel would have had to be taken into consideration for such a discussion.

8.2 Discussion of Modeling Methodology

8.2.1 Global Model

The global model was modeled in SIMA RIFLEX, and consisted of the whole dynamic part of the cable. The transfer functions provided by Dr. Techn. Olav Olsen induced the appropriate vessel motions at the cable hang off. The main design criteria were no compression and maximum curvature not to be exceeded in the cable. The cable was modeled with the lazy wave configuration, which usually implies a thether to ensure a stable touchdown. Nonetheless, the area of interest was the upper segment of the cable, and a thether was not included in the model. Moreover, the cable configuration could probably be optimized further. As the focus of the thesis was to investigate the contact mechanisms in the cable cross-section, the weather conditions were simplified only to contain 3 possible wind conditions and corresponding vessel positions.

8.2.2 Local Model

Due to the assumption of critical fatigue location, the local model only included the upper segment of the cable, including a bend stiffener. The bend stiffener served its purpose for most of the load cases, but the sudden increase in curvature in Figure B.2.1 indicates a slight optimization potential. Also, Figures C.1.14b and C.1.15b show that the curvature at the termination of the cable is not equal to zero, suggesting that the bend stiffener performs inadequately for these load cases. The helical layers of the conductors were not modeled, but included by the analytical model.

8.3 Discussion of Analyses Methodology

The local analysis was performed with 15 different load cases generated from the global analysis. Expanding the number of load cases would have increased the accuracy of the results, though at the cost of computation time. Due to the nature of the boundary conditions of the local model, the angle ranges from the global analyses had to be corrected as described in Section 6.2. The relationship between the applied angle and the total angle proved to linear with a close to perfect fit. As the original angle range classes from the Rainflow Counting was rearranged based on damage, many of the angle ranges are very close in magnitude as can be seen in Table 7.1. The results are thus sensitive to small changes, and a slightly different linear relationship could have yielded significantly different results.

The angle was chosen as the master over the tension. Initially, the plan was to determine the maximum and minimum tension for each angle range class from the sea states that contributed to the angle range class. However, this proved to be difficult due to the nature of the Rainflow Counting algorithm in Python. Instead, a simple but conservative approach was adopted. It was assumed that the maximum tension occurred at the maximum angle, minimum tension occurred at the minimum angle, and linear interpolation was used to find the corresponding tension to each angle.

Maximum tension was used in Equation 3.26 when the analytical model calculated stress range on wire level, to grant a conservative procedure. Additionally, a sensitivity study was conducted to investigate the effect on fatigue life if mean or minimum tension would have been used (see Section 7.5.1).

The cable was covered with an outer sheath, and thus cannot be inspected for crack initiation

once in service. Consequently, High Safety Class was chosen for the design safety factor. Investigation of fatigue in the steel armouring layers were not included in the study.

8.4 Results and Discussion of Results

In this section, the estimated fatigue life of the power cable is presented. The section also contains the results from the sensitivity studies and the study of the friction mechanisms and their influence on fatigue life. The results displayed in the tables of this section are mean stress corrected according to Söderberg correction, and calculated with DFF=10.0.

8.4.1 Fatigue Life of Dynamic Power Cable

The fatigue life was calculated at two points on the dynamic power cable; maximum curvature range and maximum tension range. The results are displayed in Tables 8.1 to 8.4.

Fatigue Life at Point With Maximum Curvature Range

Case nr	Cycles (n_i) pr year	$\Delta\sigma$ [MPa]	Cycles to failure (N_i)	Damage (d_i) pr year
1	6930399.80	46.26	4.47E+11	4.70E-05
2	571967.90	50.68	6.83E+10	8.37E-06
3	237278.52	52.59	5.00E+10	4.74E-06
4	219492.01	54.51	3.70E+10	5.94E-06
5	198970.39	56.40	2.77E+10	7.17E-06
6	154052.12	58.33	2.09E+10	7.37E-06
7	130555.01	60.22	1.60E+10	8.18E-06
8	93955.72	62.08	1.24E+10	7.59E-06
9	68946.29	63.95	9.63E+09	7.16E-06
10	46839.21	65.83	7.54E+09	6.21E-06
11	54651.77	69.43	4.82E+09	1.13E-05
12	24288.68	72.76	3.25E+09	7.48E-06
13	16385.80	80.46	1.39E+09	1.18E-05
14	3355.41	118.14	5.48E+07	6.13E-05
15	139.30	134.55	1.83E+07	7.61E-06
Total damage pr year			2.09E-04	
Fatigue life before mean stress correction			640.28 years	
Fatigue life			477.95 years	

Table 8.1: Fatigue life calculations for innermost layer at maximum curvature range

Case nr	Cycles (n_i) pr year	$\Delta\sigma$ [MPa]	Cycles to failure (N_i)	Damage (d_i) pr year
1	6930399.80	37.01	9.66E+11	7.17E-06
2	571967.90	41.38	3.77E+11	1.52E-06
3	237278.52	43.26	2.59E+11	9.15E-07
4	219492.01	45.15	1.81E+11	1.21E-06
5	198970.39	47.02	1.29E+11	1.55E-06
6	154052.12	48.92	9.20E+10	1.68E-06
7	130555.01	50.80	6.70E+10	1.95E-06
8	93955.72	52.62	4.98E+10	1.89E-06
9	68946.29	54.48	3.71E+10	1.86E-06
10	46839.21	56.34	2.80E+10	1.67E-06
11	24288.68	59.91	1.67E+10	3.27E-06
12	54651.77	63.19	1.07E+10	2.28E-06
13	16385.80	70.75	4.11E+09	3.98E-06
14	3355.41	107.92	1.17E+08	2.86E-05
15	139.30	124.24	3.58E+07	3.89E-06
	Total damage pr year		6.34E-05	
	Fatigue life before mean stress correction		1657.03 years	
	Fatigue life		1576.68 years	

Table 8.2: Fatigue life calculations for outer layer at maximum curvature range

Fatigue Life at Point with Maximum Tension Range

Case nr	Cycles (n_i) pr year	$\Delta\sigma$ [MPa]	Cycles to failure (N_i)	Damage (d_i) pr year
1	6930399.80	54.92	3.48E+10	1.99E-04
2	571967.90	57.83	2.25E+10	2.54E-05
3	237278.52	59.06	1.88E+10	1.26E-05
4	219492.01	60.30	1.58E+10	1.39E-05
5	198970.39	61.52	1.34E+10	1.49E-05
6	154052.12	62.74	1.13E+10	1.36E-05
7	130555.01	63.96	9.62E+09	1.36E-05
8	93955.72	65.15	8.24E+09	1.14E-05
9	68946.29	66.34	7.07E+09	9.75E-06
10	46839.21	67.55	6.07E+09	7.72E-06
11	54651.77	69.84	4.59E+09	1.19E-05
12	24288.68	71.91	3.58E+09	6.78E-06
13	16385.80	76.67	2.09E+09	7.85E-06
14	3355.41	104.93	1.49E+08	2.26E-05
15	139.30	118.30	5.41E+07	2.57E-06
	Total damage pr year		3.74E-04	
	Fatigue life before mean stress correction		462.31 years	
	Fatigue life		267.37 years	

Table 8.3: Fatigue life calculations for innermost layer at location with maximum tension range

Case nr	Cycles (n_i) pr year	$\Delta\sigma$ [MPa]	Cycles to failure (N_i)	Damage (d_i) pr year
1	6930399.78	44.14	2.19E+11	3.17E-05
2	571967.90	47.00	1.29E+11	4.44E-06
3	237278.52	48.19	1.04E+11	2.27E-06
4	219492.01	49.39	8.49E+10	2.59E-06
5	198970.39	50.57	6.96E+10	2.86E-06
6	154052.13	51.77	5.72E+10	2.70E-06
7	130555.01	52.95	4.73+10	2.77E-06
8	93955.72	54.10	3.94E+10	2.39E-06
9	68946.29	55.26	3.30E+10	2.09E-06
10	46839.21	56.44	2.76E+10	1.70E-06
11	54651.77	58.65	2.00E+10	2.74E-06
12	24288.68	60.62	1.51E+10	1.60E-06
13	16385.80	65.13	8.25E+09	1.99E-06
14	3355.41	92.59	4.26E+08	7.87E-06
15	139.30	105.83	1.38E+08	1.01E-06
Total damage pr year			7.07E-05	
Fatigue life before mean stress correction			2478.20 years	
Fatigue life			1415.18 years	

Table 8.4: Fatigue life calculations for the outer layer at the location with maximum tension

The fatigue life calculations displayed in Tables 8.1 to 8.4 show that fatigue damage is more severe at the point with maximum tension range, as this point exhibits the shortest fatigue life. The fatigue life of the dynamic power cable was thus estimated to be 267.37 years. The inner layer prove to be the critical layer for both points of the conductor, indicating that local effects govern fatigue life. The mean stress corrections was performed according to the Söderberg Assumption. The exponent in the SN-Curve was high at m=8.424, making the results sensitive to correction.

8.4.2 Results from Sensitivity Studies and Study of Friction Mechanisms

In this section, the results from the sensitivity study and the studies of the contact mechanisms are presented.

Study of sensitivity by using Mean and Minimum Tension in Equation 3.26

When using minimum, mean and maximum tension for T in Equation 3.26, the fatigue life increased as shown in Table 8.5

Tension level	Fatigue life [yrs]	Fatigue life before mean stress correction [yrs]
Maximum tension	267.37	640.28
Mean tension	412.32	980.66
Minimum tension	837.24	2228.80

Table 8.5: Fatigue life with maximum, mean and minimum tension used in Equation 3.26

Table 8.5 show the increase in fatigue life, when applying the less conservative approach for tension in Equation 3.26 in the analytical model. Compared to the original approach, using maximum

tension, the fatigue life roughly doubles and quadruples with mean tension and minimum tension respectively. The importance of using maximum tension in the analytical model is hence not negligible.

8.4.3 Study of Sensitivity to Choice of SN-Curve

The results from the calculation of fatigue life using the SN-Curves presented in Karlsen (2010), are displayed in Table 8.6.

SN-Curve used	Fatigue life [years]
SN-Curve cable 1	1065.88
SN-Curve cable 2	2.24

Table 8.6: Fatigue life calculated by using SN-Curves from Karlsen (2010)

The results from Table 8.6 show that the fatigue life increased by a factor of almost 4 and decreased by a factor of over 100 when using the two SN-Curves from Karlsen (2010). The results show that the fatigue life calculation is very sensitive to the choice of SN-Curve.

Study of effect of contact between conductors

The results from the study of the effect of contact between the conductors are shown in Table 8.7 and Table 8.8.

Case nr	Cycles (n_i) pr year	$\Delta\sigma$ [MPa]	Cycles to failure (N_i)	Damage (d_i) pr year
1	6930399.80	43.87	2.31E+11	3.00E-05
2	571967.90	46.24	1.48E+11	3.87E-06
3	237278.52	47.23	1.23E+11	1.92E-06
4	219492.01	48.22	1.04E+11	2.11E-06
5	198970.39	49.20	8.77E+10	2.27E-06
6	154052.12	50.18	7.42E+11	2.08E-06
7	130555.01	51.18	6.29E+10	2.07E-06
8	93955.72	52.16	5.36E+10	1.75E-06
9	68946.29	53.15	4.58E+10	1.51E-06
10	46839.21	54.16	3.90E+10	1.20E-06
11	54651.77	56.13	2.89E+10	1.89E-06
12	24288.68	58.03	2.19E+10	1.11E-06
13	16385.80	62.71	1.14E+10	1.44E-06
14	3355.41	95.57	3.27E+08	1.03E-05
15	139.30	113.37	7.75E+07	1.80E-06
	Total damage pr year		6.54E-05	
	Fatigue life before mean stress correction		4011.16 years	
	Fatigue life		1530.15 years	

Table 8.7: Fatigue life calculations for innermost layer without effect of contact between conductors

Case nr	Cycles (n_i) pr year	$\Delta\sigma$ [MPa]	Cycles to failure (N_i)	Damage (d_i) pr year
1	6930399.78	32.30	3.04E+12	2.28E-06
2	571967.90	34.61	1.70E+12	3.37E-07
3	237278.52	35.56	1.35E+12	1.75E-07
4	219492.01	36.50	1.08E+12	2.02E-07
5	198970.39	37.44	8.76E+11	2.27E-07
6	154052.13	38.39	7.09E+11	2.17E-07
7	130555.01	39.35	5.76E+11	2.27E-07
8	93955.72	40.29	4.72E+11	1.99E-07
9	68946.29	41.26	3.87E+11	1.78E-07
10	46839.21	42.23	3.17E+11	1.48E-07
11	54651.77	44.13	2.19E+11	2.49E-07
12	24288.68	45.95	1.56E+11	1.56E-07
13	16385.80	50.43	7.12E+10	2.30E-07
14	3355.41	82.86	1.09E+09	3.09E-06
15	139.30	100.71	2.10E+08	6.63E-07
Total damage pr year			8.58E-06	
Fatigue life before mean stress correction			25219.47 years	
Fatigue life			11660.53 years	

Table 8.8: Fatigue life calculations for outer layer without effect of contact between conductors

Case nr.	ΔT_{max} $[N/m^2]$	ΔT_f $[N/m^2]$	$^{\Delta T_f}/_{\Delta T}$
1	2442.63	1142.47	0.46
2	2589.11	1210.25	0.47
3	2645.16	1239.32	0.47
4	2701.09	1268.36	0.47
5	2757.21	1297.21	0.47
6	2812.61	1326.23	0.47
7	2867.66	1353.73	0.47
8	2921.06	1379.66	0.47
9	2972.15	1404.10	0.47
10	3025.85	1429.00	0.47
11	3121.18	1469.23	0.47
12	3200.23	1492.39	0.47
13	3353.31	1507.64	0.45
14	3835.45	1101.39	0.29
15	3628.41	627.45	0.17

Table 8.9: Comparison of total stress range and stress range from friction

Tables 8.7 and 8.8 show that the fatigue life, with the inner layer as design layer, was estimated to be 1530.15 years when the effect of contact between conductors was excluded. The fatigue life was roughly 5 times the fatigue life of the original calculation in Table 8.3. Table 8.9 shows that the contact between the conductors contributes to approximately half of the tension range for most cases. The deviations seen in cases 14 and 15 are assumed to originate from the bend stiffener's lack of ability to perform optimally for some cases, as discussed in Section 8.2.2.

8.4.4 Study of Effect of Contact Between Layers in Conductors

Table 8.10 and Table 8.11 show the results from the study of the contact between the layers in the conductor.

Case nr	Cycles (n_i) pr year	$\Delta\sigma$ [MPa]	Cycles to failure (N_i)	Damage (d_i) pr year
1	6930399.80	43.62	2.42E+11	2.87E-05
2	571967.90	46.58	1.39E+11	4.11E-06
3	237278.52	47.81	1.12E+11	2.12E-06
4	219492.01	49.03	9.03E+10	2.43E-06
5	198970.39	50.24	7.36E+10	2.70E-06
6	154052.12	51.45	6.01E+10	2.56E-06
7	130555.01	52.66	4.95E+10	2.64E-06
8	93955.72	53.83	4.11E+10	2.28E-06
9	68946.29	55.00	3.43E+10	2.01E-06
10	46839.21	56.18	2.87E+10	1.63E-06
11	54651.77	58.39	2.07E+10	2.64E-06
12	24288.68	60.35	1.57E+10	1.55E-06
13	16385.80	64.79	8.63E+09	1.90E-06
14	3355.41	92.75	2.20E+08	7.99E-06
15	139.30	107.03	1.26E+08	1.11E-06
Total damage pr year			6.63E-05	
Fatigue life before mean stress correction			4142.13 years	
Fatigue life			1507.39 years	

Table 8.10: Fatigue life calculations for innermost layer without effect of friction between layers in the conductor

Case nr	Cycles (n_i) pr year	$\Delta\sigma$ [MPa]	Cycles to failure (N_i)	Damage (d_i) pr year
1	6930399.78	45.29	1.76E+11	3.93E-05
2	571967.90	48.16	1.05E+11	5.44E-06
3	237278.52	49.35	8.56E+10	2.77E-06
4	219492.01	50.53	7.00E+10	3.13E-06
5	198970.39	51.70	5.78E+10	3.45E-06
6	154052.12	52.88	4.77E+10	3.23E-06
7	130555.01	54.05	3.97E+10	3.29E-06
8	93955.72	55.19	3.33E+10	2.82E-06
9	68946.29	56.32	2.81E+10	2.45E-06
10	46839.21	57.47	2.37E+10	1.98E-06
11	54651.77	59.61	1.74E+10	3.14E-06
12	24288.68	61.52	1.34E+10	1.82E-06
13	16385.80	65.82	7.55E+09	2.17E-06
14	3355.41	92.56	4.28E+08	7.85E-06
15	139.30	105.86	1.38E+08	1.01E-06
Total damage pr year			8.39E-05	
Fatigue life before mean stress correction			2478.20 years	
Fatigue life			1192.22 years	

Table 8.11: Fatigue life calculations for outer layer without the effect of friction between layers in the conductor

Table 8.10 and 8.11 show the calculations of the fatigue life of the cable when the effect of the friction between the layers in the conductor was excluded. The fatigue life was calculated to be 1507.39 years with the inner layer as the design layer, more than five times the fatigue life in the original calculation. The fatigue damage was almost identical in the two layers before the mean stress correction was performed.

Chapter 9

Conclusion and Further Work

9.1 Conclusion

This study was carried out to determine the fatigue life of a dynamic power cable applied in offshore wind farms, as well as obtaining insights into the contact mechanisms of the cable cross-section. Dr. Techn. Olav Olsen's design OO-Star, at West of Barra Scotland, was chosen as a basis for a case study. SIMA RIFLEX was used to build a global model that included the whole dynamic part of the power cable. As the focus of the study was to examine local effects in the cross-section rather than complete a full fatigue analysis, several simplifications were done in terms of the possible displacements of the floating wind turbine.

The upper part of the power cable was modeled in a local model in Bflex, with the different layers and components of the cable cross-section, and also a bend stiffener. Contact between layers was modeled by contact elements, yielding a complex stress model situation.

The global analyses were performed by exposing the global model to 160 sea states from the scatter diagram, with one hour record length. The angle between the vessel and the cable and the tension in the upper element were converted into time series and counted by the Rainflow Counting algorithm. The cycle counts and angle range classes were rearranged into 15 cases with dynamic angles and corresponding tensions. Each dynamic angle and tension pair was applied to the local model for one full cycle. Then, the analytical model in Section 3.4.6 was applied to calculate the stress range on wire level, from the results obtained by the local analysis. By the use of an SN-Curve and the Miner Palmgren summation concept, the fatigue life was calculated at two separate points of the conductor by applying a safety factor 10 in the calculations. The results were mean stress corrected by the Söderberg correction. Studies were also performed to investigate the sensitivity to contact mechanisms of the cross-section.

The main findings in this study are summarized in Table 9.1:

Analysis	Fatigue life [years]	Fatigue life w/o Söderberg corr. [years]	Design layer
A	477.95	640.28	Inner
B	267.37	462.31	Inner
C	1530.16	4011.16	Inner
D	1507.39	4142.13	Inner

Table 9.1: Main findings summarized

where:

A means calculation at the location of maximum curvature range, all contacts included

B means calculation at the location of maximum tension range, all contacts included

C means calculation at the location of maximum tension range, the effect of contact between conductors is excluded

D means calculation at the location of maximum tension range, the effect of contact between layers in conductors is excluded

Furthermore:

- All failures occurred in the inner layer, suggesting that the fatigue life of the copper conductor is governed by local friction effect in the cross-section.
- The fatigue life of the dynamic power cable was calculated to be 267.37 years, with a safety factor of 10, at the point of the conductor having the highest tension range. The point on the conductor with maximum curvature range, on the other hand, exhibited more than 1.5 times the fatigue life in comparison.
- The fatigue life was very sensitive to choice of SN-Curve
- Excluding the effect of contact between conductors increased the fatigue life roughly by a factor of 5. It was also found that the effect of contact between the conductors contributed to almost half of the tension range.
- Excluding the effect of friction between layers also increased the fatigue life with roughly 5 times

These findings suggest that in general the local effects in the cable cross-section play an important role in the calculation of fatigue life. The two contact mechanisms investigated are of approximately the same importance in this case, after Söderberg corrections. These results may not be applicable to determine the exact effect of excluding the contact mechanisms, as only one case study was examined. Nevertheless, it can be concluded that contact between conductors and contact between layers in conductors both should be included in fatigue analyses.

9.2 Further Work

The topic of fatigue in dynamic power cables applied in offshore wind farms is not adequately studied yet, and thus, there are many possible approaches for further work. A number of possible future studies using the same numerical set up are apparent:

- Future trials need to be done to establish a statistical foundation to determine the true effect of excluding contact mechanisms in the cross-sections of dynamic power cables.
- A natural extension of this work is to perform the same modeling and analysis procedure as used in this project with other case scenarios. With the Lifes50+ project as a basis, several combinations of location and support structure designs could be analyzed, and fatigue lives could be estimated. The results could then be used to optimize designs of support structures in terms of power cable fatigue life.
- The global model can be expanded by introducing more complex weather conditions and fewer restrictions on displacement. The advancement of the global model would allow for a more accurate cycle count and fatigue analysis.
- It would be interesting to assess the effects of double armoring layers. This would increase the inertia of the cable, and thus reduce its motions.
- Fatigue in the steel armouring layers could also be investigated.
- Studies of optimization of cable configuration and cross-sections in terms of fatigue life could also be conducted.

Bibliography

Alani, M. & Raoof, M. (1997), 'Effect of mean axial load on axial fatigue life of spiral strands', *International Journal of Fatigue* **19**(1), 1–11.

Almar-Næss, A. (1985), 'Fatigue handbook : offshore steel structures'.

American Petroleum Institute (2014), 'Specification for unbounded flexible pipe'.

Bailey, H., Brookes, K. & Thompson, P. (2014), 'Assessing environmental impacts of offshore wind farms: Lessons learned and recommendations for the future', **10**, 8.

Beckman, R. L., Burnet, D. R. & Davenport, T. M. (2013), 'Submarine cables : the handbook of law and policy'.

Berge, S. (2016), *Fatigue and Fracture Design of Marine structures*, NTNU, Faculty of Engineering and Science.

Bolotinha, M. (n.d.), 'An introduction to submarine cables subsea power cables'. Accessed 05.10.2018.
URL: *https://www.electricaltechnology.org/2018/02/submarine-cables-subsea-power-cables.html*

Chien, C., Yap, E., Martindale, H. & Bucknall, R. (2004), Mechanical and electrical performance analysis of high power subsea transmission cable, *in* '39th International Universities Power Engineering Conference, UPEC 2004 - Conference Proceedings', Vol. 3, pp. 1258–1261.

Deigen, J. (2017), 'An illustrated guide to the growing size of wind turbines'. Accessed 03.10.2018.
URL: *https://www.greentechmedia.com/articles/read/an-illustrated-guide-to-the-growing-size-of-wind-turbinesgs.sE1pHLQ*

Det Norske Veritas (DNV) (2010), 'Riser fatigue, recommended practice dnv-rp-f204'.

Det Norske Veritas (DNV) (2014), 'Enviromental conditions and enviromental loads, recomended practice dnv-rp-c205'.

DNV GL (2016), 'Fatigue design of offshore steel structures, recomended practice dnvgl-rp-c203'.

Dr. Techn. Olav Olsen (n.d.), 'Prosjekt: Lifes50+'. Accessed 10.10.2018.
URL: *https://www.olavolsen.no/global/upload/4BPPQ/files/LIFES50%2B.pdf*

Equinor (2018), 'World's first floating wind farm has started production'. Accessed 03.10.2018.
URL: *https://www.equinor.com/en/news/worlds-first-floating-wind-farm-started-production.html*

European Wind Energy Association (EWEA) (2015), 'Wind energy scenarios for 2030'. Accessed 03.10.2018.
URL: *https://www.ewea.org/fileadmin/files/library/publications/reports/EWEA-Wind-energy-scenarios-2030.pdf*

Faltinsen, O. M. (1990), *Sea loads on ships and offshore structures*, Cambridge ocean technology series, Cambridge University Press, Cambridge.

Feld, G., Owen, D., Reuben, R. & Crockett, A. (1995), 'Mechanical behaviour of the metallic elements of submarine cables as a function of cable loading', *Engineering Structures* **17**(4), 240–253.

Gao, Z., Bingham, H., Ingram, D., Kolios, A., Karmakar, D., Utsunomiya, T., Capitovic, I., Colicchio, G., Rodrigues, J. M., Adam, F., Karr, D., Fang, C., Shin, H.-K., Slätte, J., Ji, C., Sheng, W., Liu, P. & Stoev, L. (2018), 'Issc 2018 committee v.4: Offshore renewable energy', pp. 193–277.

Geos, F. (2001), 'Wind and wave frequency distributions for sites around the british isles'.

Global Wind Energy Counsil (GWEC) (2018), 'Gwec global wind 2017 report'. Accessed 03.10.2018.
URL: *http://gwec.net/global-figures/global-offshore/*

Hau, E. (2013), *Wind Turbines : Fundamentals, Technologies, Application, Economics*, 3rd ed. edn.

Health Safety Executive (HSE) (2001), 'Enviromental conditions offshore technology report'.

Hills, D. A. (1994), *Mechanics of Fretting Fatique*, Vol. 30 of *Solid Mechanics and Its Applications*, Dordrecht.

Horizon 2020 (n.d.), 'What is horizon 2020?'. Accessed 10.10.2018.
URL: *https://ec.europa.eu/programmes/horizon2020/what-horizon-2020*

International Renewable Energy Association IRENA (2016), 'Floating foundations: A game changer for offshore wind power'.

Janiszewski, P. (n.d.), 'Implementation of astm e1049-85 rainflow cycle counting algorythm'. Accessed 01.05.2019.
URL: *https://pypi.org/project/rainflow/*

Kapsali & Kaldellis, M, J. (2012), *Offshore Wind Power Basics*.

Karlsen, S. (2010), 'Fatigue of copper conductors for dynamic subsea power cables', *29th International Conference on Ocean, Offshore and Arctic Engineering* **6**.
URL: *http://dx.doi.org/10.1115/OMAE2010-21017*

Langen, I. & Sigbjörnsson, R. (1979), *Dynamisk analyse av konstruksjoner*, [s.n.], S.l.

Lifes50+ (2015), 'Qualification of innovative floating substructures for 10mw wind turbines and water depths greater than 50m, deliverable 1.1 oceanographic and meteorological conditions for the design'. Accessed 12.10.2018.
URL: *https://lifes50plus.eu/wp-content/uploads/2015/12/GA*$_6$*40741*$_L$$IFES50 -_D$ *1.1.pdf*

Lifes50+ (2017), 'Qualification of innovative floating substructures for 10mw wind turbines and water depths greater than 50m, d1.6 upscaling procedures'. Accessed 10.10.2018.
URL: *https://lifes50plus.eu/wp-content/uploads/2015/11/Deliverable-D1.6-Upscaling-procedures.pdf*

Lifes50+ (2018), 'Qualification of innovative floating substructures for 10mw wind turbines and water depths greater than 50m, deliverable d4.2 public definition of the two lifes50+ 10mw floater concepts'. Accessed 10.10.2018.
URL: *https://lifes50plus.eu/wp-content/uploads/2018/04/GA*$_6$*40741*$_L$*IFES50*$_D$*4.2.pdf*

Lifes50+ (n.d.), 'Lifes50+'. Accessed 10.10.2018.
URL: *https://lifes50plus.eu/*

Lynn, P. A. (2011), *Onshore and Offshore Wind Energy*, John Wiley Sons Inc.

Make Consulting (2016), 'Norwegian oppurtunities in offshore wind'.

Mathew, S. & Philip, G. (2012), 2.05 - wind turbines: Evolution, basic principles, and classifications, *in* A. Sayigh, ed., 'Comprehensive Renewable Energy', Elsevier, Oxford, pp. 93 – 111.
URL: *http://www.sciencedirect.com/science/article/pii/B9780080878720002055*

Mathisen, K. M. (1990), *Large displacement analysis of flexible and rigid systems considering displacement-dependent loads and nonlinear constraints*, Vol. 1990:33 of *Doktor ingeniøravhandling (Trondheim : trykt utg.)*, Division of Structural Engineering, Norwegian Institute of Technology, Trondheim.

Moan, T. (2003), *TMR 4190 Finite Element Modelling and Analysis of Marine Structures*, NTNU, Department of Marine Technology.

Nasution, F. P., Sævik, S. & Berge, S. (2014), 'Experimental and finite element analysis of fatigue strength for 300 mm2 copper power conductor', *Marine Structures* **39**, 225–254.

Nasution, F. P., Sævik, S. & Gjøsteen, J. K. (2012), 'Finite element analysis of the fatigue strength of copper power conductors exposed to tension and bending loads', *International Journal of Fatigue* **59**, 114 – 128.
URL: *http://www.sciencedirect.com/science/article/pii/S0142112313002703*

Nasution, F. P., Sævik, S., Gjøsteen, J. K. & Berge, S. (2013), 'Experimental and finite element analysis of fatigue performance of copper power conductors', *International Journal of Fatigue* **47**, 244–258.

Ng, C. & Ran, L. (2016), *1 - Introduction to offshore wind energy*, Woodhead Publishing.
URL: *http://www.sciencedirect.com/science/article/pii/B9780081007792000015*

Patrick, D. R. (2000), *Understanding AC circuits*, Newnes, Boston.

Pettersen, B. (2007), *Kompendium: Marin Teknikk 3 - Hydrodynamikk*, Institutt for Marin teknikk, Trondheim.

Powell, E. I. R. (1995), *Three-phase a.c. circuits-5*.

Raoof, M. & Davies, T. J. (2008), 'Axial fatigue design of sheathed spiral strands in deep water applications', *International Journal of Fatigue* **30**(12), 2220–2238.

SINTEF Ocean (2017), *RIFLEX 4.10.1 Theory Manual*.

Sommerville, D. (2010), 'Offshore wind farms: Floating solutions for deep-water cables'. Accessed 06.10.2018.
URL: *https://www.powerengineeringint.com/articles/print/volume-18/issue-10/features/offshore-wind-farms-floating-solutions-for-deep-water-cables.html*

Srinil, N. (2016), *13 - Cabling to connect offshore wind turbines to onshore facilities*, Woodhead Publishing.
URL: *http://www.sciencedirect.com/science/article/pii/B9780081007792000131*

Sævik, S. (2013), 'bflex2010- theory manual'.

Sævik, S. (2017), 'bflex2010 theory manual'.

Sævik, S. & Ye, N. (2016), *Aspects of Design and Analysis of Offshore Pipelines and Flexibles*.

Taninoki, R., Abe, K., Sukegawa, T., Azuma, D. & Nishikawa, M. (2017), 'Dynamic cable system for floating offshore wind power generation', *SEI Technical Review* (84), 53–58.

Thies, P. R., Johanning, L. & Smith, G. H. (2012), 'Assessing mechanical loading regimes and fatigue life of marine power cables in marine energy applications', *Proceedings of the Institution of Mechanical Engineers, Part O: Journal of Risk and Reliability* **226**(1), 18–32.

Wagner, H.-J. (2013), *Introduction to Wind Energy Systems : Basics, Technology and Operation*, Green energy and technology, 2nd ed. edn.

Walt Musial, Donna Heimiller, P. B. G. S. & Draxl, C. (2016), '2016 offshore wind energy resource assessment for the united states'. Accessed 03.10.2018.
URL: *https://www.nrel.gov/docs/fy16osti/66599.pdf*

Wind Europe (2018), 'Offshore wind in europe - key trends and statistics 2017'. Accessed 03.10.2018.
URL: *https://windeurope.org/about-wind/statistics/offshore/european-offshore-wind-industry-key-trends-statistics-2017/presentation*

Worzyk, T. (2009), 'Submarine power cables : Design, installation, repair, environmental aspects'.

Yagihashi, K., Tateno, Y., Sakakibara, H. & Manabe, H. (2015), Dynamic cable installation for fukushima floating offshore wind farm demonstration project, *in* 'Proceeding Jicable 15–International Conference on Insulated Power Cables'.

Yang, S.-H., Ringsberg, J. W., Johnson, E. & Hu, Z. (2017), 'Biofouling on mooring lines and power cables used in wave energy converter systems—analysis of fatigue life and energy performance', *Applied Ocean Research* **65**, 166–177.

Appendix A

Results from Testing of Global Model

A.1 Static Configuration Without Current

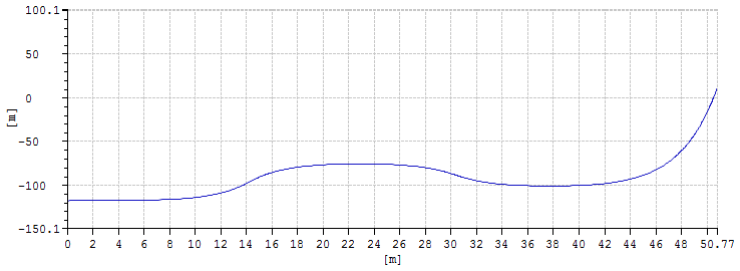

Figure A.1.1: Configuration for near position without current

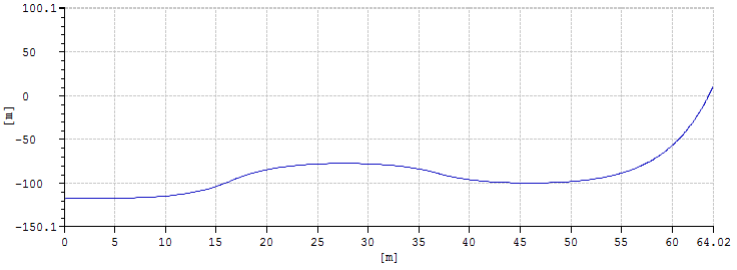

Figure A.1.2: Configuration for neutral position without current

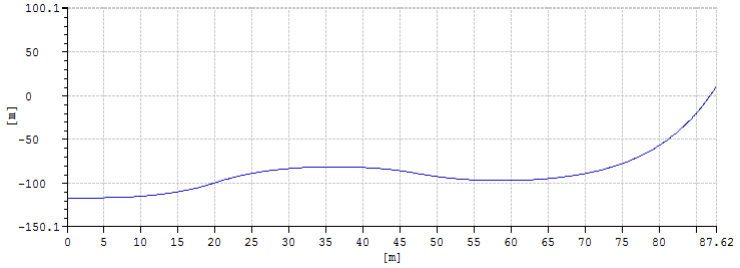

Figure A.1.3: Configuration for far position without current

A.2 Static Configuration With Current

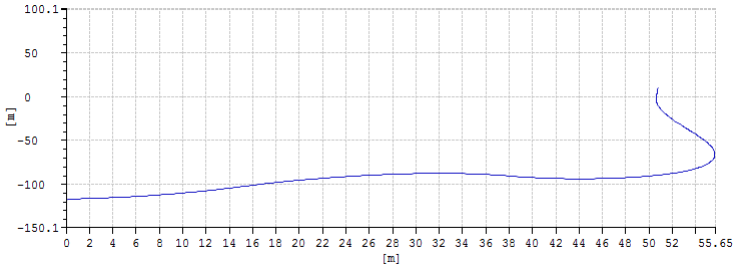

Figure A.2.1: Configuration for near position with current

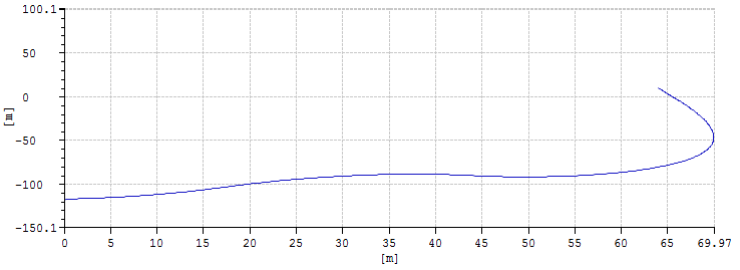

Figure A.2.2: Configuration for neutral position with current

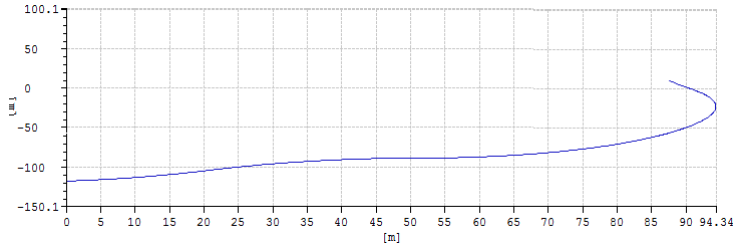

Figure A.2.3: Configuration for far position with current

A.3 Curvature

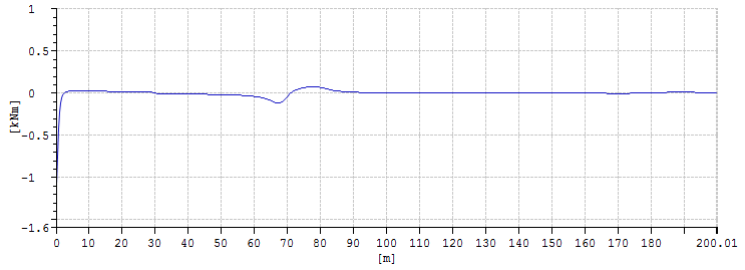

Figure A.3.1: Curvature envelope for near position

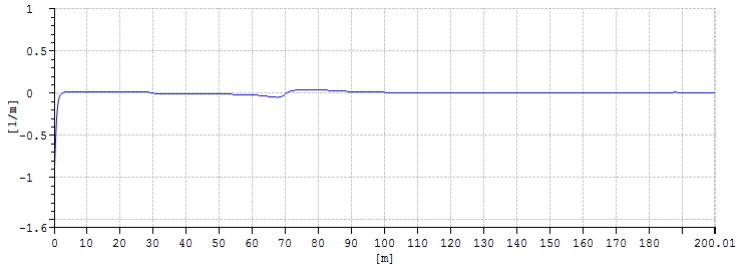

Figure A.3.2: Curvature envelope for neutral position

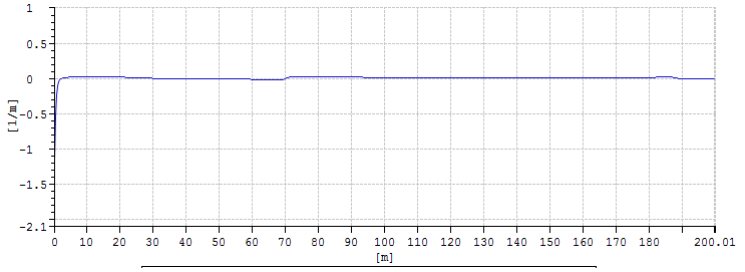

Figure A.3.3: Curvature envelope for far position

A.4 Maximum Tension

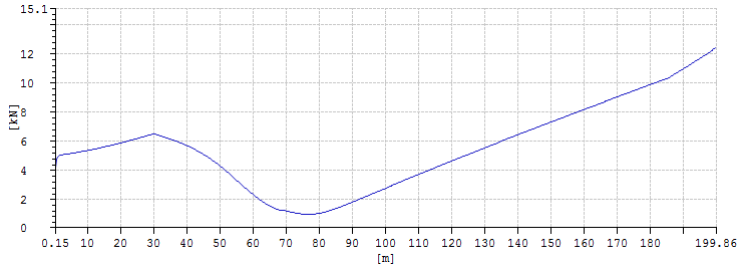

Figure A.4.1: The maximum tension over the length of the cable in near position

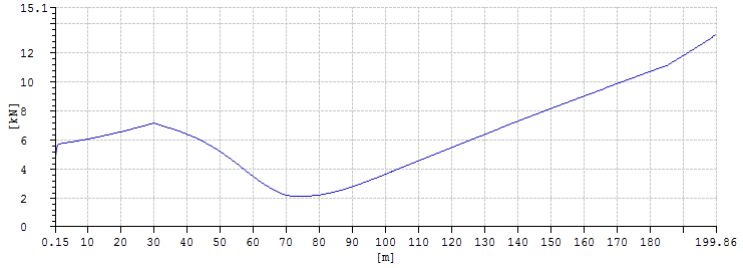

Figure A.4.2: The maximum tension over the length of the cable in neutral position

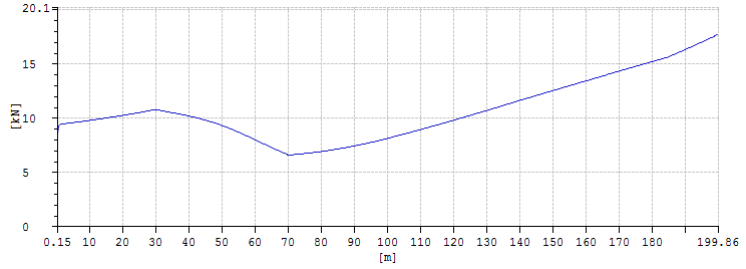

Figure A.4.3: The maximum tension over the length of the cable in far position

A.5 Minimum Tension

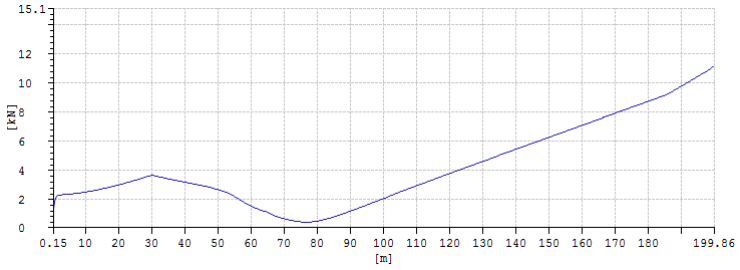

Figure A.5.1: The minimum tension over the length of the cable in near position

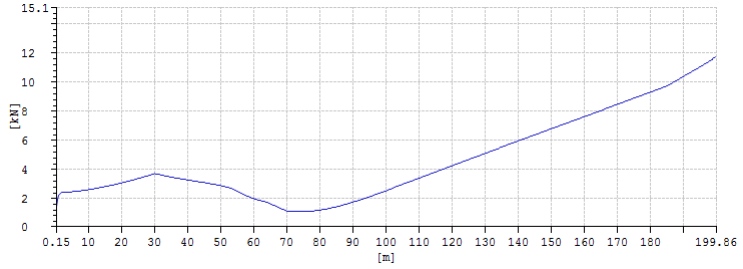

Figure A.5.2: The minimum tension over the length of the cable in neutral position

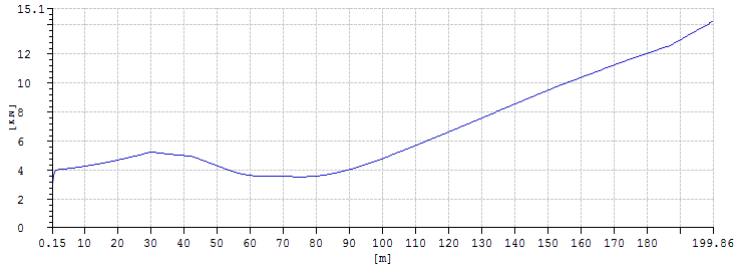

Figure A.5.3: The minimum tension over the length of the cable in far position

Appendix B

Results from Testing of Local Model

B.1 Cable

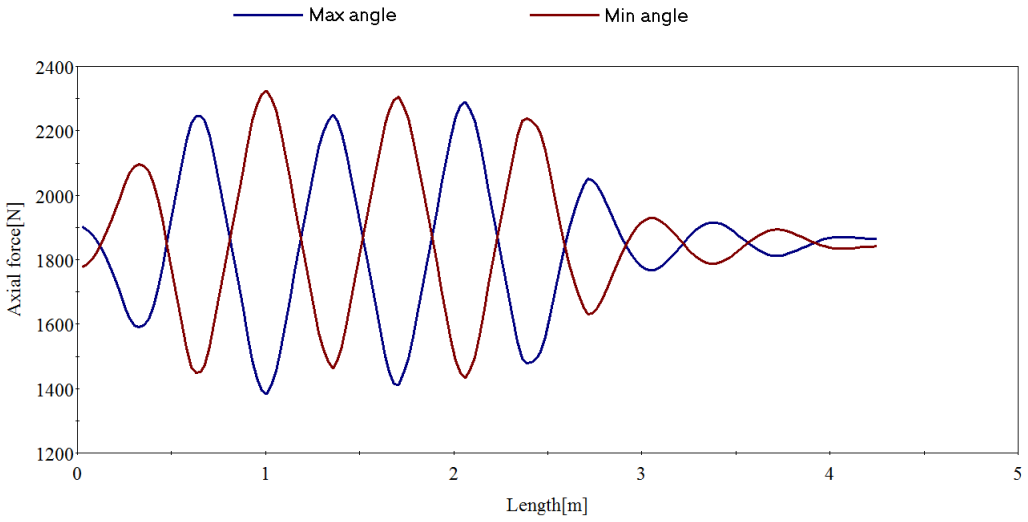

Figure B.1.1: Axial force in conductors over length of cable [N]

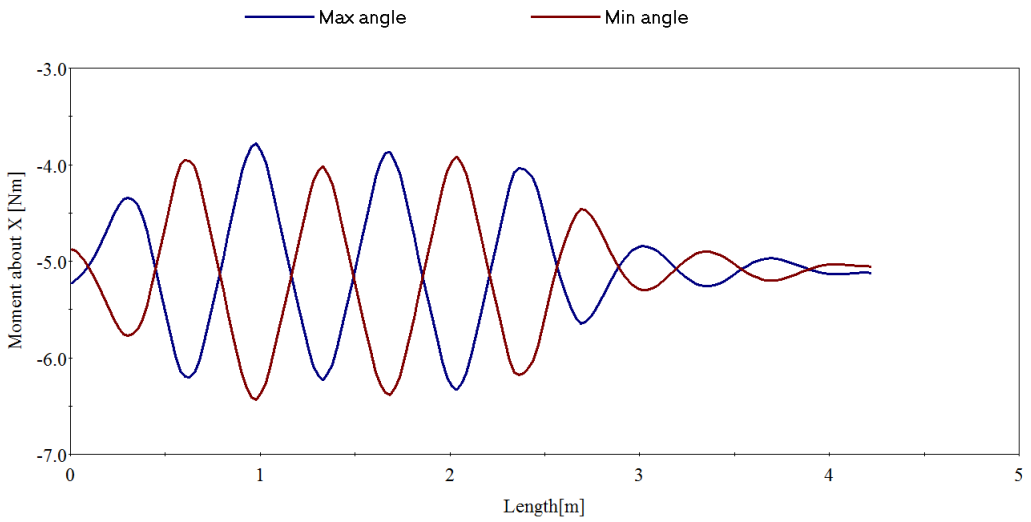

Figure B.1.2: Moment about X-Axis in conductors over length of cable [Nm]

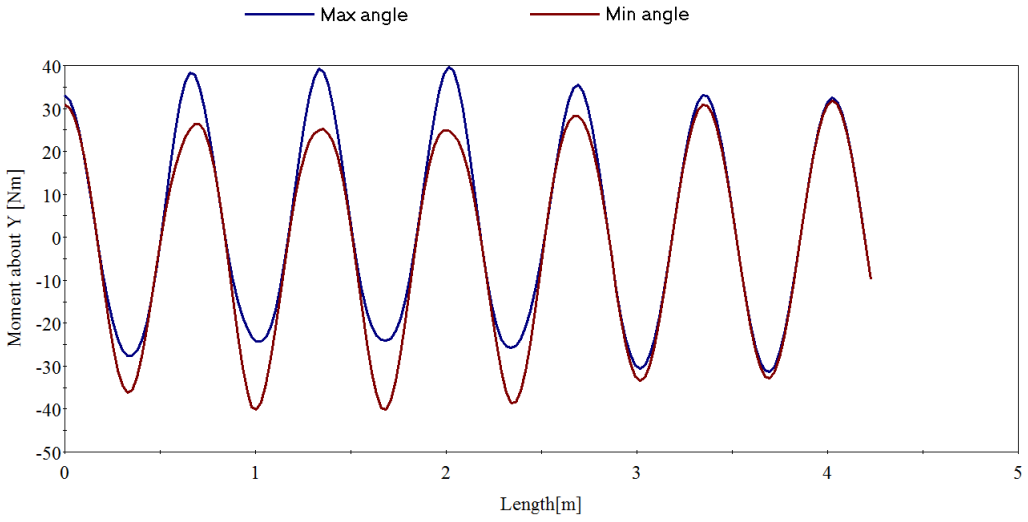

Figure B.1.3: Moment about Y-Axis in conductors over length of cable [Nm]

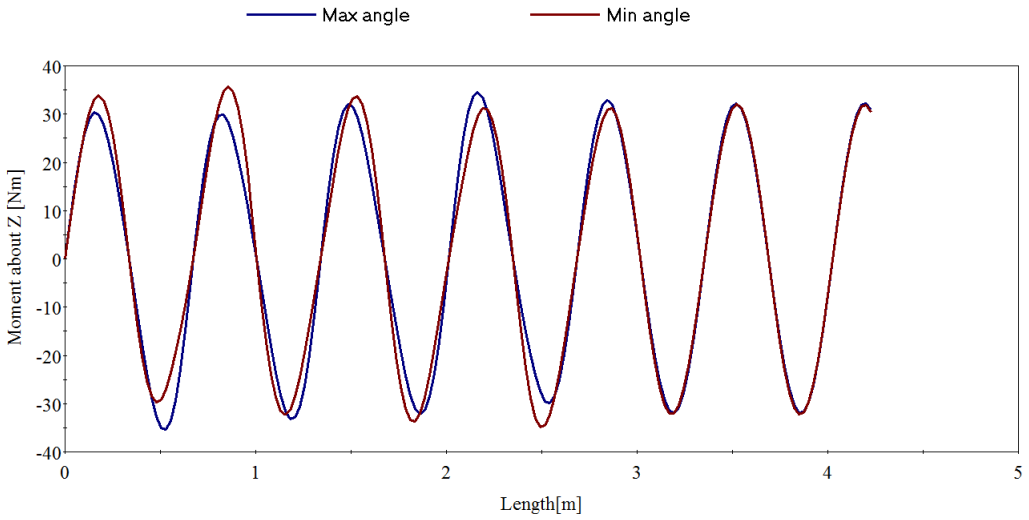

Figure B.1.4: Moment about z-axis in conductors over length of cable [Nm]

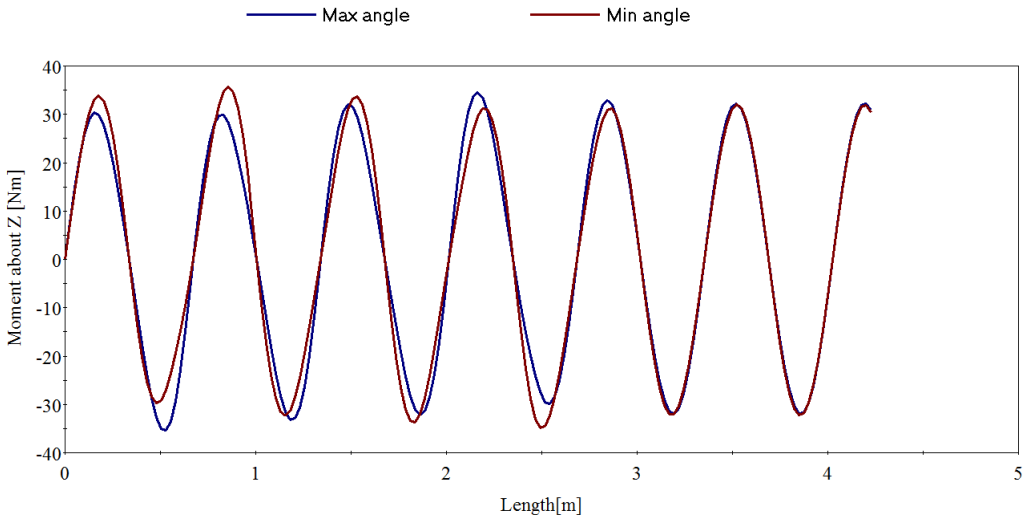

Figure B.1.5: Axial force in conductors over length of cable [Nm]

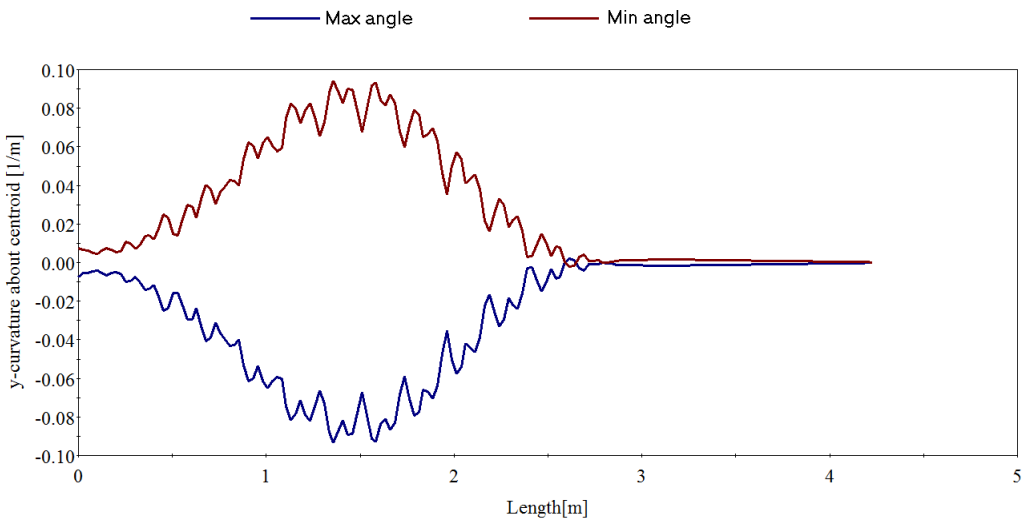

Figure B.1.6: Curvature in the outer sheath over the length of cable [1/m]

B.2 Bend Stiffener

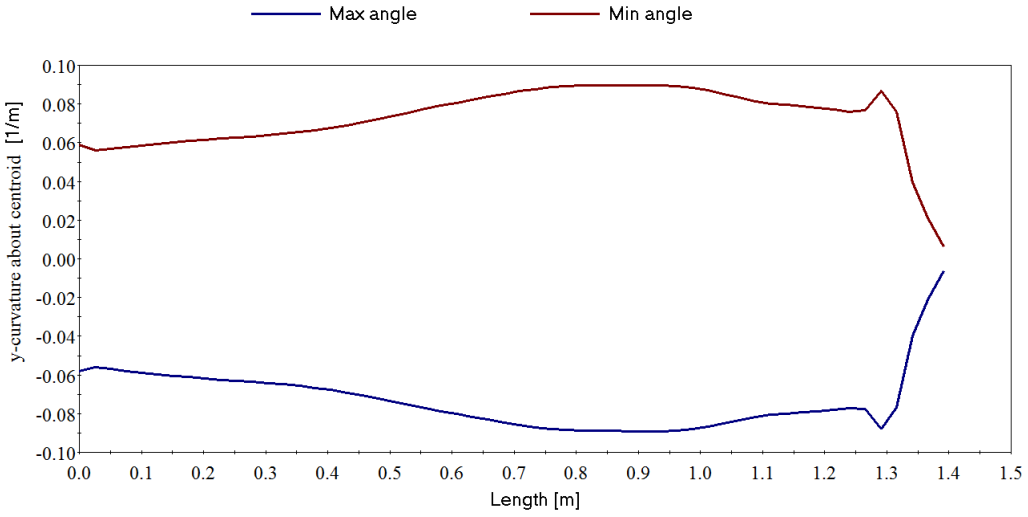

Figure B.2.1: Curvature in bend stiffener

Appendix C

Results

C.1 Results from the Local Analysis

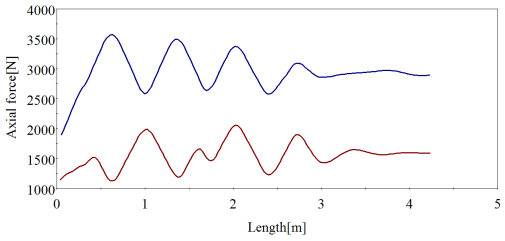

(a) Tension in conductor

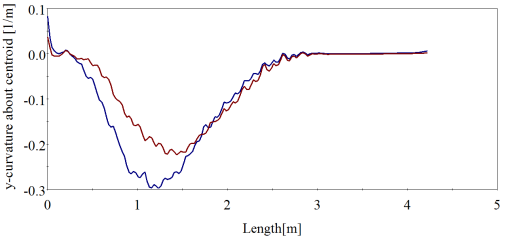

(b) Curvature in conductor

Figure C.1.1: Results from Load case 1. The blue plot is at the maximum angle and the red plot is at the minimum angle

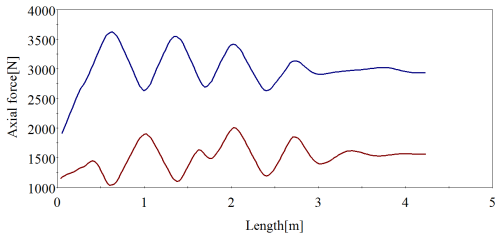

(a) Tension in conductor

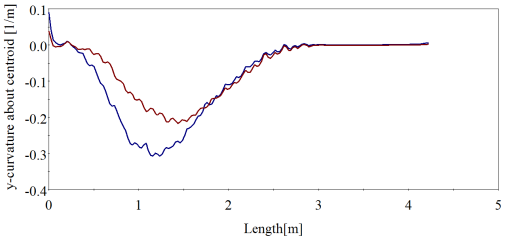

(b) Curvature in conductor

Figure C.1.2: Results from Load case 2. The blue plot is at the maximum angle and the red plot is at the the minimum angle

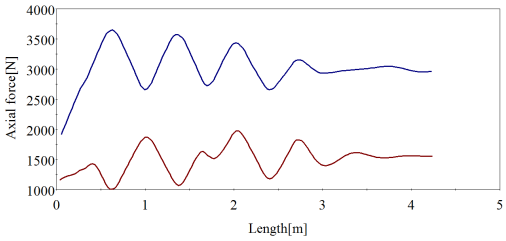

(a) Tension in conductor

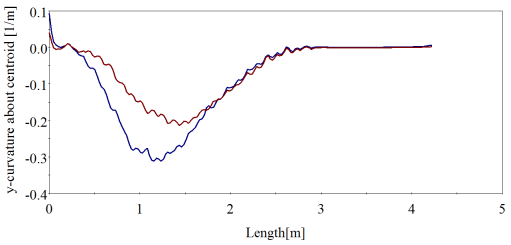

(b) Curvature in conductor

Figure C.1.3: Results from Load case 3. The blue plot is at the maximum angle and the red plot is at the the minimum angle

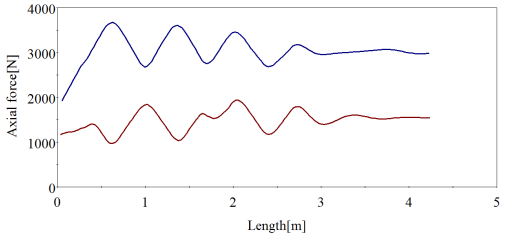

(a) Tension in conductor

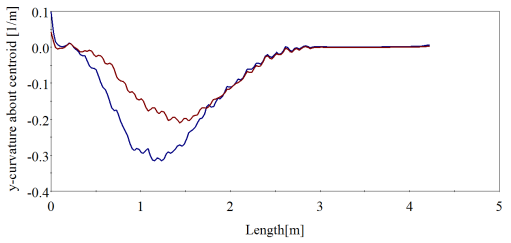

(b) Curvature in conductor

Figure C.1.4: Results from Load case 4. The blue plot is at the maximum angle and the red plot is at the the minimum angle

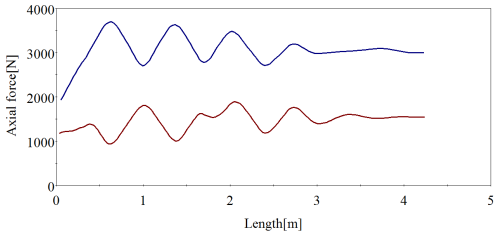

(a) Tension in conductor

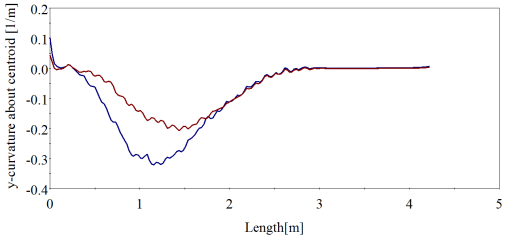

(b) Curvature in conductor

Figure C.1.5: Results from Load case 5. The blue plot is at the maximum angle and the red plot is at the the minimum angle

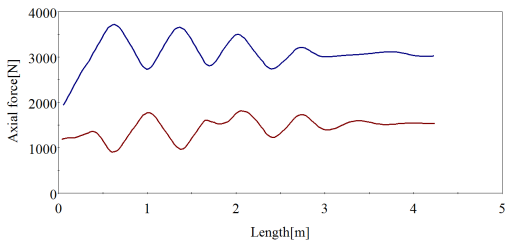

(a) Tension in conductor

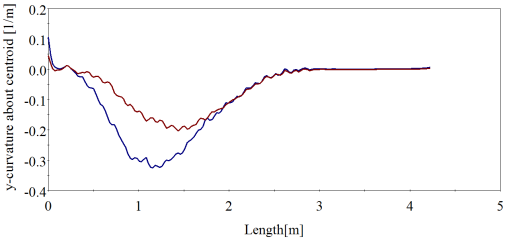

(b) Curvature in conductor

Figure C.1.6: Results from Load case 6. The blue plot is at the maximum angle and the red plot is at the the minimum angle

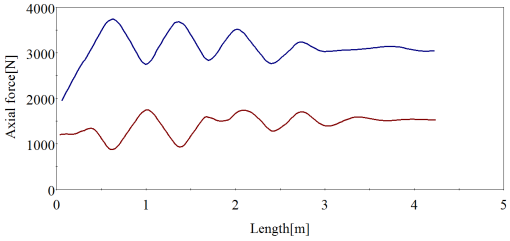

(a) Tension in conductor

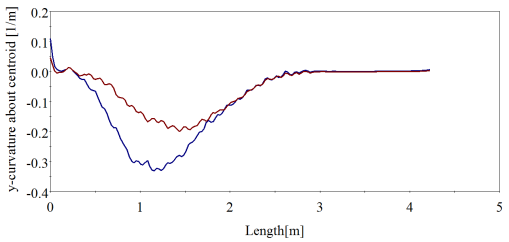

(b) Curvature in conductor

Figure C.1.7: Results from Load case 7. The blue plot is at the maximum angle and the red plot is at the the minimum angle

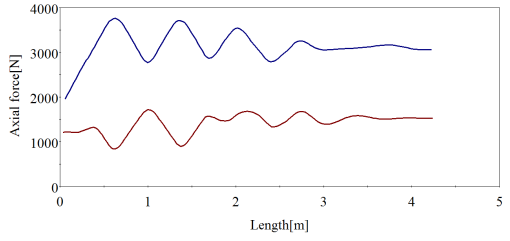

(a) Tension in conductor

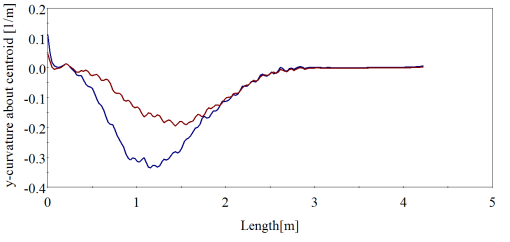

(b) Curvature in conductor

Figure C.1.8: Results from Load case 8. The blue plot is at the maximum angle and the red plot is at the the minimum angle

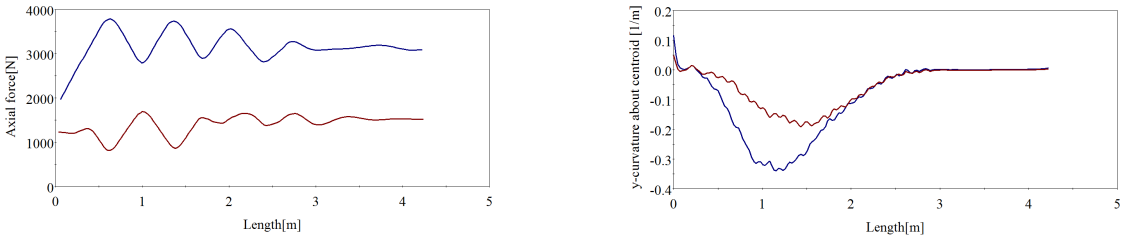

(a) Tension in conductor (b) Curvature in conductor

Figure C.1.9: Results from Load case 9. The blue plot is at the maximum angle and the red plot is at the the minimum angle

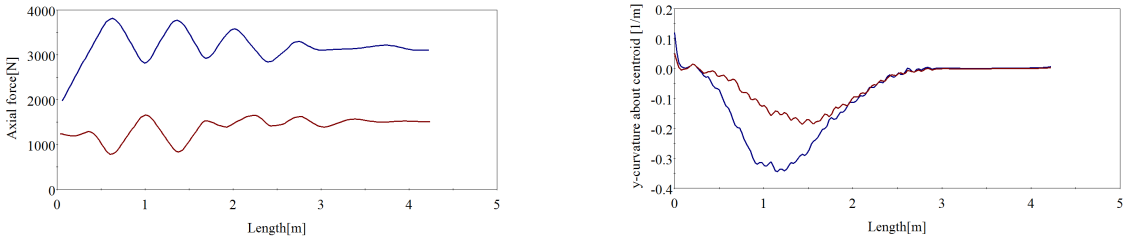

(a) Tension in conductor (b) Curvature in conductor

Figure C.1.10: Results from Load case 10. The blue plot is at the maximum angle and the red plot is at the the minimum angle

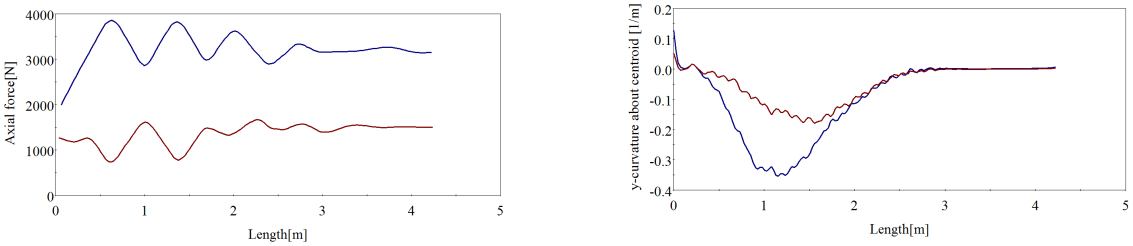

(a) Tension in conductor (b) Curvature in conductor

Figure C.1.11: Results from Load case 11. The blue plot is at the maximum angle and the red plot is at the the minimum angle

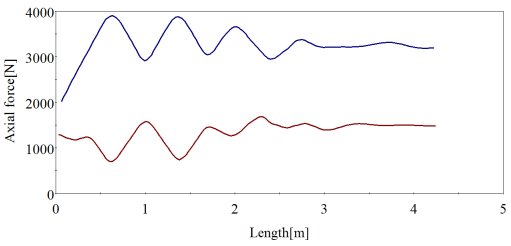

(a) Tension in conductor

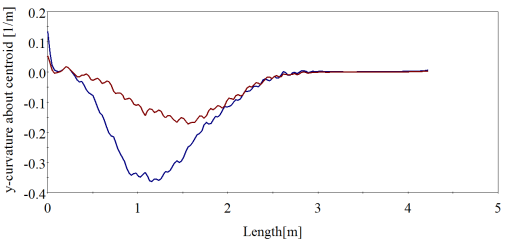

(b) Curvature in conductor

Figure C.1.12: Results from Load case 12. The blue plot is at the maximum angle and the red plot is at the the minimum angle

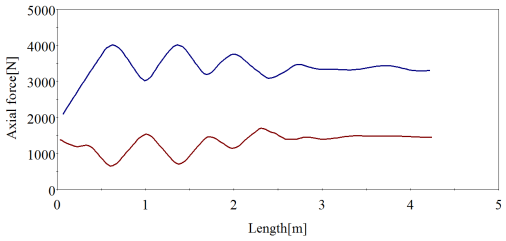

(a) Tension in conductor

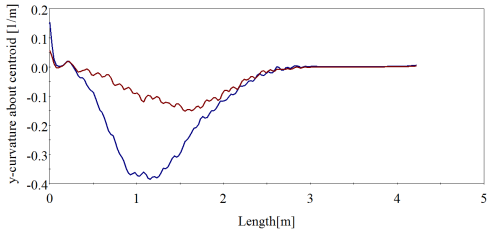

(b) Curvature in conductor

Figure C.1.13: Results from Load case 13. The blue plot is at the maximum angle and the red plot is at the the minimum angle

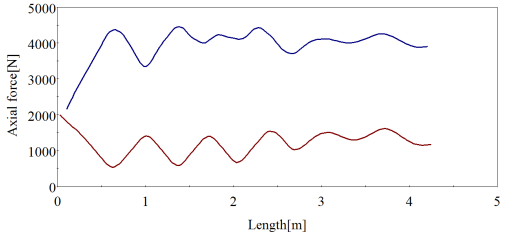

(a) Tension in conductor

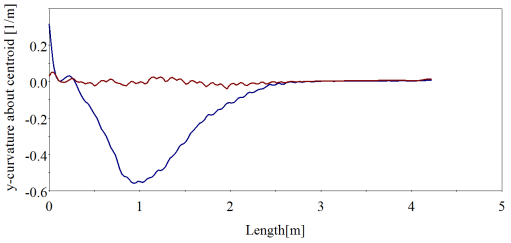

(b) Curvature in conductor

Figure C.1.14: Results from Load case 14. The blue plot is at the maximum angle and the red plot is at the the minimum angle

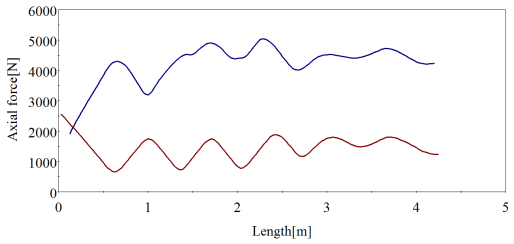

(a) Tension in conductor

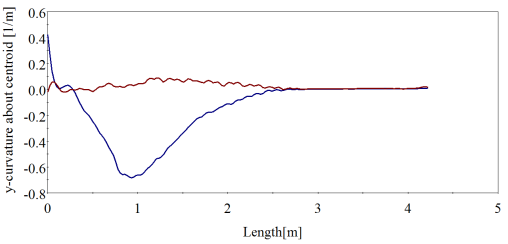

(b) Curvature in conductor

Figure C.1.15: Results from Load case 15. The blue plot is at the maximum angle and the red plot is at the the minimum angle

Karoline Bakken

Fatigue of Dynamic Power Cables Applied in Offshore Wind Farms

NTNU
Norwegian University of
Science and Technology